THE MECHANICAL ALLOYING OF SUB-STOICHIOMETRIC TITANIUM CARBONITRIDE-TUNGSTEN-ALUMINIUM BY HIGH ENERGY BALL MILLING

Maweja Kasonde

A Thesis submitted to the Faculty of Engineering and the Built Environment, University of the Witwatersrand, in fulfilment of the requirements for the degree of Doctor of Philosophy.

Johannesburg 2011

DECLARATION

I, Maweja Kasonde declare that this thesis is my own work. It is being submitted for the degree Doctor of Philosophy at the University of the Witwatersrand, Johannesburg. It has not been submitted before for any degree or examination at any other university.

Maweja Kasonde

This day of , 2011

Dedicates

To Aimée, Gentille, Artig and Candide

ACKNOWLEDGEMENTS

Work! Source of happiness and key to ascent!

Friendship and modesty become true and are magnified when supported by Work.

Beyond the words of this thesis, lie our greetings to all who strive for the sustainable development and well being of the humanity.

Our great thanks go to Professor Lesley A. Cornish for her mentoring and constructive remarks.

Thanks also extend to Doctor Nedret Can who explained the need for the potential impact of dissolving a refractory metal in titanium carbonitrides.

Amount of work and analyses results presented in this work were generated with the help of Josias Thagisa and Doctor Johan Westraadt.

THE MECHANICAL ALLOYING OF SUB-STOICHIOMETRIC TITANIUM CARBONITRIDE – TUNGSTEN – ALUMINIUM BY HIGH ENERGY BALL MILLING

Maweja Kasonde

Supervisor: Professor Lesley A. Cornish

Co-supervisor: Doctor Nedret Can

ABSTRACT

The transformations occurring in the sub-stoichiometric Ti(C,N) – W - Al system processed by high energy ball mill were investigated. The milling parameters included the milling time and the temperature comprising milling at subzero temperature and above 25˚C. Two sub-stoichiometric Ti(C,N) stocks were selected, the $Ti(C_{0.5}N_{0.05})$ containing more interstitial elements than the $Ti(C_{0.5}N_{0.5})_{0.6}$.The transformation stages and mechanisms of alloying are discussed with respect to the changes in crystal structures of the powder constituents. The milling atmosphere had an effect on the lattice strain of milled products, and hence on the kinetics of solid state dissolution between the powder constituents, but it did not affect the fracturing process.

The release of the stored crystallite lattice strain energy was the major determinant in mechanical alloying, with particle size reduction playing a necessary, but less significant role. The strain energy and the fine particle size contributed to the increased chemical

reactivity with oxygen of the powders milled for shorter times. The affinity of the powders with oxygen decreased after W dissolution in Ti(C,N), and the subsequent decrease in lattice strains.

The annealing behaviour of $Ti(C_{0.5}N_{0.05})$ - 40wt% W and $Ti(C_{0.5}N_{0.5})_{0.6}$ - 40wt% W mechanically alloyed powders were investigated using XRD, TEM, SEM and DTA techniques. It was observed that the reaction start and finish temperatures between constituents were lower in the system that had higher residual lattice strains after milling. The compositions of the intermetallic compounds and the solid solutions formed were dependent on the milling conditions and the annealing temperature. Thermal alloying was observed during annealing of $Ti(C_{0.5}N_{0.05})$ - 40wt% W mechanically alloyed products, whereas de-mixing of W-rich phases from the metastable solid solution occurred during annealing of the $Ti(C_{0.5}N_{0.5})_{0.6}$ - 40wt% W milled powders.

The effects of Al addition and milling at subzero temperatures on the transformation of $Ti(C_{0.5}N_{0.05})$-W powder mixtures were investigated. Addition of Al powder improved the kinetics of solid solution between powder constituents. The effect of Al was ascribed to the increase of lattice strain during short milling time followed of relaxation at longer time, and to the fast diffusion of atoms. Also, it was noticed that the high viscosity of the process control agent could inhibit the alloying process.
Multiple three-component compounds could be formed. Aluminium preferably reacted with tungsten. The W(Al,C) and W(Al,Ti) formed were stable, thus solubility of W in $Ti(C_{0.5}N_{0.05})$ in the presence of Al was limited.

The evolution of the morphologies of Ti(C,N)-W mixtures show that fracturing of hard particles dominated in the early stage of milling in the absence of Al, whereas with Al, plastic deformation of particles and cold welding of Ti(C,N) and W particles by the softer Al prevailed at the same time.

Longer milling time improved the homogeneity and the formation of nanostructured binder pools in the sintered products. Lower oxygen contents in sintered PcBN were achieved by mechanically alloying Ti(C,N), W and Al in the high energy ball milling stage. Low level of Co in the infiltration layer was also achieved when sintering PcBN with this type of binder. A link was established between the addition of Al at the attrition milling stage and high oxygen content in the sintered PcBN, thus should be avoided.

The pressure and temperature applied during sintering or annealing had a strong effect on the compositions and the crystal structures of the phases formed in the mechanically alloyed binder. The lattice strains of the binder and the PcBN were higher in the sintered materials prepared with the $Ti(C_{0.5}N_{0.5})_{0.6}$-W binder than in those made using the $Ti(C_{0.5}N_{0.05})$-W alloys.

KEYWORDS

Mechanical alloying; ball milling; titanium; tungsten; aluminium, lattice strain; atmosphere; temperature

TABLE OF CONTENTS

CHAPTER 1. GENERAL INTRODUCTION

Mechanical alloying is recognized as an efficient technique for the development of nano-structured, quasi-crystalline and non-equilibrium materials [1-6]. This technique allows the formation of metastable solid solutions by interdiffusion between metals and/or ceramics at relatively low temperature compared to their respective melting points. Metal systems that have positive Gibbs' free energy of mixing and non-favourable Hume-Rothery difference between the atoms radii have been alloyed mechanically [1-6]. Mechanical alloying was proven to be efficient in alloying metals that could not be alloyed by conventional casting because of the large differences in melting points despite their satisfying alloying conditions such as atom radii, identical crystalline structures and electronegativity. For example, alloying of Ti and Mg was achieved by high energy ball milling with controllable crystal structure [7, 8]. It is worthwhile noticing that the desired crystal structure, thus the performance of the alloy, processed by high energy ball milling can be achieved by means of careful adjustments to the processing parameters, such as the milling time, atmosphere, process control agent (PCA), status of the starting powder constituents – elemental powders or pre-alloyed powders, ball-to-powder mass ratio and temperature. The process is versatile and easily scalable to pilot and industrial scales.

The present study aimed to investigate the mechanisms of transformations and reactions occurring between two sub-stoichiometric titanium carbonitride species ($Ti(C_{0.5}N_{0.05})$ and $Ti(C_{0.5}N_{0.5})_{0.6}$, the elemental tungsten and aluminium powders processed in a planetary high energy ball mill.

The solubility between Al, Ti and W are introduced using the assessed equilibrium phase diagrams published by ASM International, Ed Massalski T.B. [9]. Different versions of these diagrams are available in the literature. The Ti-W binary equilibrium phase diagram showed the existence of a monotectoid composition at about 90at.% Ti - 10at.% W. The monotectoid temperature is estimated at about 740 ± 20˚C. The solubility of W in Ti below the eutectoid temperature is less than 1wt%. The system readily decomposes into a mixture of HCP titanium and a BCC phase rich in tungsten below the monotectoid temperature as shown in Figure 1.1a. The solubility of W in Al remains lower than 20 at.% at temperatures below 1523˚C as shown in Figure 1.1b, whereas Ti and Al can form a variety of binary compounds. The phase diagram in Figure 1.1c indicates that the binary titanium aluminides are located in the titanium rich end of the equilibrium phase diagram. It is believed that the small solubility between Ti, W and Al at low temperature and the formation of the binary compounds between Ti and Al and between Al and W may be the cause of formation of heterogeneous binder phases in sintered polycrystalline cubic born nitrides.

The ternary Al - Ti - W equilibrium phase diagram also predicts limited miscibility of the three elements at 1300˚C. Development of alloys based on these three elements by the casting route would present many technological challenges due to the differences in melting temperatures between them: W (3422˚C), Al (660˚C) and Ti (1670˚C). Thus, mechanical alloying was considered an appropriate technique for alloying constituents of systems predominantly composed of these three elements.

Figure 1.1a. Ti - W, Reevaluation of the Ti-W System and Prediction of the Ti-W-N Phase Diagram, by Jonsson S., in [9].

Figure 1.1b. Al-W (Aluminum-Tungsten) binary phase diagram, by Okamoto H., in [9]

Figure 1.1c. Al-Ti Phase Diagram, by Schuster J.C. and Palm M., in [9].

The mechanically alloyed powders are intended to replace the Ti(C/N)-Al based binders currently used in high pressure high temperature (HPHT) sintering of polycrystalline cubic boron nitride (PcBN). Conventional methods of alloying include the attrition milling admixing of Ti(C/N), Al and boron nitride powders in the correct ratio, and the alloying often occurs in-situ during the PcBN sintering process [10]. Although convenient, the method leads to variations in the alloying compositions within the matrix, and often results in inadequate homogeneity in the overall microstructure. Also, it is limited to simple binder systems. Thus, there is a great need for a simple and controllable method of alloying. Such methods should be able to alloy complex systems containing multiple elements, which may contain oxides, nitrides and carbides. Mechanical alloying is seen as a potential candidate.

Typical starting materials in PcBN sintering consist of high purity (99.5 wt%) fine grained cBN and Al binder particles (~3 μm, purity >98 wt%) [10]. The starting mixtures are degassed in vacuum of 3.4 x 10^{-3} Pa and temperature of 500˚C for one hour before HPHT sintering. The introduction of the high melting temperature element, W, in the binder system is expected to increase the high temperature properties of the binder and the bulk properties of the sintered PcBN. One shortcoming of the current Ti(C,N)-Al based binders is due to the formation of the Ti-aluminides and Ti-borides binary compounds during the sintering of PcBN [10-24]. The binary compounds are believed to render the hard sintered materials brittle. Another drawback of the custom binders is the formation of heterogeneous binder phases in the PcBN [13, 14, 24]. The introduction of W into the system by high energy ball milling equally aims to form more homogeneous binders containing ternary compounds instead of the brittle binary phases.

Two alloying procedures that would minimise the formation of the Ti-aluminides were investigated in this study; e.g.

- Pre-alloying the sub-stoichiometric Ti(C,N) with elemental W before adding Al into the system
- Admixing the three constituents and process the mixture by high energy ball milling.

HPHT sintering of PcBN is commonly conducted at elevated temperatures between 1200 and 2000˚C [10, 13, 14, 24]. The binary equilibrium phase diagram in Figure 1.1a shows the existence of a BCC (βTi,W) solid solution in the indicated temperature range before

melting. This solid solution decomposes in cooling to 1250˚C. The corresponding composition is at about 35wt% Ti. The monotectoid composition at which the solid state solubility between Ti and W is achieved is about (60 - 80wt%)Ti - (40 - 20wt%)W [9]. It would be preferable, for the development of a low temperature single phase binder, to mechanically alloy Ti-W based system in this composition range to be used in sintering processes above the monotectoid temperature.

Two major groups of PcBN are produced for industrial applications [10]:

- Low cBN designed for moderately interrupted hard turning and finish hard milling. The material has approximately 45 - 65% cBN, a sub-micron cBN grain size and a $Ti(C_xN_y)$ or TiC binder. Having one of the finest structures of all commercial grades, it can also provide for sub – micrometer surface roughness.
- High cBN are made of mixtures of cBN, in contents higher than those on low cBN, with special binders. The binder phases contain AlWCoB for some of these products and Al-nitrides and borides for others. High cBN are used in turning and cutting of hard cast iron and hard and abrasive workpiece materials.

The fracture toughness of all these groups of PcBN is sensitive to the oxygen content of the product. The binder phase is believed to be the main vector of oxygen into the system. Therefore the fracture toughness of the PcBN would be improved by lowering the oxygen content in the binder. Therefore, it was expected that alloying of W, Al and the Ti(C,N) would decrease the affinity of the binder with oxygen, and hence would decrease the oxygen content of the milled powder.

The mechanisms of alloying and transformation in systems processed by high energy ball milling were investigated in argon and in a nitrogen atmosphere. The effect of milling time, milling atmosphere, powder composition on the kinetics of alloying and on the intermediate transformations were examined using X-ray diffraction, scanning electron microscopy, transmission electron microscopy, oxygen and nitrogen analysis and differential thermal analysis of the milled powders.

The efficacy of the mechanically alloyed powders used in binding of the PcBN sinters was investigated and compared to the traditional binders. Homogeneity of the binder phase, which determines the wear resistance of the sintered PcBN and the state of residual stresses upon HPHT synthesis, was analysed by SEM and TEM. The sintering mechanism was hence determined.

CHAPTER 2. LITERATURE REVIEW

2.1. Industrial background

Polycrystalline cubic boron nitride is the second hardest material next to the diamond and posses many excellent physical and chemical properties (thermal stability up to 1200˚C), high resistance to chemical attack, mechanical properties (high elastic modulus *E* value near diamond materials). Its performance exceeds diamond in many applications involving contact with ferrous alloys and high temperatures [10-24].

The tools made from cubic boron nitride (cBN) and ceramic or metal binders are widely used for cutting hardened steels, cast iron and others [10-24]. Finish hard turning has experienced significant growth due to the need for continuously improving productivity and decreasing the processing cost [19-22]. This trend towards greater efficiency resulted in a growing demand for wear-resistant tools and a two-digit growth rate of consumption of PcBN.

Aluminum, silicon and other rare earth compounds are usually used as the binders in PcBN [11, 12]. It would be ideal to eliminate the use of these pure elements because they usually become the less resistant microstructure constituents in PcBN applications. Titanium carbides and carbonitride-based binders are used to replace pure element binders [13, 14]. However, these ceramic binders are brittle because of the formation of titanium aluminides during sintering.

Cermets bonds are also used widely because of their properties of forming both metallic bonds (good toughness) and ceramic bonds (high hardness and good heat endurance) [11, 12].

Sintering temperature has a determinant effect of the microstructure and properties of PcBN [15]. Zhao and Wang prepared polycrystalline Si_3N_4-Al_2O_3-Y_2O_3-cBN by spark plasma sintering at different temperatures between 1250 and 1450˚C. The main phases were cBN, corundum (α-Al_2O_3) and Sialon ($Si_4Al_2O_2N_6$). The relative density, microhardness and fracture toughness of samples increased with the sintering temperature. The relative densities, microhardness and fracture toughness of PcBN samples prepared at 1450˚C were 98.6%, 48GPa and 11.5MPa $m^{1/2}$ respectively [15].

The effects of insertion by mechanical alloying of elemental W, Ni, and carbide such as WC, Mo_2C, NbC on the microstructure and properties of Ti(C,N) - (Co, Ni) cermets that present potential to be used as cutting tools in turning and milling were investigated [25-32]. The addition of Mo_2C [25] gave different microstructures and properties than WC, and addition of NbC could lower the sintering temperature of the Ti($C_{0.7}N_{0.3}$)-WC-Mo_2C-(Co,Ni) cermets [26-28]. The hardness decreased with increased WC content in the presence of Mo_2C, whereas increased hardness and transverse rupture strength were reported in the absence of Mo_2C [28].

Li *et al.* [28] also showed that the toughness of the Ti(C,N)-based partially-complete solid solution cermets (PSS) was improved greatly with the addition of (Ti,W)C complete

solid solution phase (CSS). The addition of CSS enabled the control of the microstructure and mechanical properties of the sintered products.

Formation of core-rim microstructures during sintering is attributed to kinetics reasons for diffusion of atoms of the solute into particles of solid solvent. Therefore, particles of the final products are heterogeneous, and concentration gradients of solute are noticed across the particle sections. The toughness of PSS improved in direct proportion to the variation in core fraction of the core-rim microstructure in the sintered cermets [30].

Ahn and Kang [31 – 33, 35] and Ahn *et al.* [34] reported that the relative dissolution rate of Ti(CN) with respect to those of carbide additives such as WC, NbC, TaC and HfC in liquid Ni binder could be estimated from the composition of the rim part of sintered particles. The effect of the binder composition on the fracture toughness, hardness, thermal shock resistance and transverse rupture strength of titanium carbide – based cermets was given [36-39].

Typical binder constituents used in PcBN sintering are given in Table 2.1. Cubic boron nitride is only thermodynamically stable at high pressure. Therefore, cBN powder can be synthesized only at high pressure and temperatures (p = 4 - 9GPa, T = 1200 - 2100˚C). After mixing cBN powder with a cobalt alloy or Ti-Al compound, such as TiC-TiN-Al_2O_3 as a binder, sintering has to be done under extreme conditions of pressure and temperature. Typical properties of PcBN are listed in Table 2.2, along with other polycrystalline hard phases.

Table 2.1. Constituents of the binders used in PcBN sintering [10]

	PcBN (1)	**PcBN (2)**	**PcBN (3)**
Binder composition (EDX)	Ti, Al, C, N; Co	Ti, Al, C, N; Ni	Ti, Al, N

Table 2.2. Properties of polycrystalline hard phases [10]

Properties	**PcBN**	**WC**	**α-β Sialon**
Density (g/cm$^{3)}$	3.5	15.7	3.25
Grain size (μm)	2-5	0.15	2-3
$HV_{0.1}$	≤ 4000	3500	
HV_{10}		2900	1750
KIC (from crack length) (MPa $\sqrt{m}$)	6	7	5-7
Fracture strength (MPa)		≤ 1000	1000
Elastic modulus (GPa)	680	700	320
Thermal conductivity (W/(mK)	1300	100	5-15

Lahiri and Bhargava [40] showed that mechanical alloying changed the sintering process of Cu-Cr compacts from liquid phase sintering to solid-state sintering, thus making the process more energy efficient. Studies of the grain growth behavior of WC-Co systems showed that grain growth occurs during the early stages of sintering of nanostructured cemented materials [41-45]. Schubert pointed out that grain growth started during heating

up to the temperature, which was attributed to the high degree of metastability of the powder [45].

Benko *et al.* [46] investigated the effect of the binder composition on the chemical equilibria, microstructure and properties of PcBN. They confirmed the formation of TiB_2 in the cBN/TiN sintered composite, and TiB_2 and $TiC_{0.8}N_{0.2}$ in the cBN/TiC sintered composite [46], as predicted by thermodynamic calculations using the VCS (Villars, Cruise, Smith) algorithm [47]. Both TiB_2 and $TiC_{0.8}N_{0.2}$ compounds were found to be present just after heat treatment. Their location in layers or zones respectively to boron nitride grains was identified in a sequence: BN/TiB_2/TiN in BN/TiN composites; and in a sequence BN/TiB_2/$TiC_{0.8}N_{0.2}$/TiC in BN/TiC composites.

Casanova *et al.* [48] studied the kinetics of plastic deformation during sintering of PcBN compacts, with and without Al binder, sintered at 8GPa and 1850˚C using different processing times. They showed that the kinetics of plastic deformation for cBN was similar to the kinetics for diamond compacts. An intensive plastic deformation of cBN grains was observed at the short heating times (15s). The plastic deformation was smaller in compacts sintered with Al binder because it decreased the stress concentration at the cBN grain boundaries. The defect annealing process in cBN compacts dominated at longer heating times (t>15 s), which was attributed to the presence of the binder which generated additional stress by the reaction of Al with cBN. The binder could also reduce the stress relief and the recrystallization rate of cBN grains by hindering the movement of dislocations.

PcBN compacts were sintered from the cBN-Al and cBN-AlN systems in the temperature range of 1300 - 1700˚C for 20 minutes under high pressure ~ 5.0GPa [49]. It was found that the sintering mechanisms were quite different in the two systems. In the cBN-Al system, AlN and AlB_2 were observed due to the chemical reactions of cBN and Al, which led to a homogeneous microstructure in the sinters. Conversely, the AlN grains aggregated heavily in the cBN-AlN sintered samples. Cutting tests showed that PcBN compacts which had a homogeneous microstructure had a longer tool life. Kato *et al.* [50] suggested that the tool life of a binder-less PcBN tool at a cutting speed of 33.3 m/s was improved remarkably compared with the usual PcBN (BW80) tool. Many thermal cracks extending perpendicular from the cutting edge were observed in the usual PcBN tool after short cutting distance, and the width of thermal strain cracks enlarged, resulting in damage to the flank wear face.

Alternative composites to PcBN such as pseudo eutectic titanium diboride-boron carbide composites prepared by mechanical alloying of elemental powders and sintering by spark plasma sintering (SPS) were investigated [51]. Low pressure sintering of PcBN with a cBN content around 50vol.% would offer an opportunity to reduce tool costs and to promote the use of PcBN in hard machining. The deposition of cBN, which is being investigated worldwide, offers an interesting opportunity to create complex cBN tools. New alloys with finer grain size of cBN are also being developed. As with hard cermets, coatings and adopted cutting edge treatments will contribute to a further improvement of the performance of PcBN tools [52-56].

It was generally claimed in the past that cBN-rich films thicker than 200 nm peeled off quickly after deposition [57-59]. The bad adhesion was attributed to the presence of compressive stress in the cBN-containing films. A reason for the bad adhesion is the formation of a sp^2-bonded boron nitride layer located between the cBN-rich top layer and the substrate [60, 61]. The quality of cBN films grown by plasma enhanced chemical vapor deposition (PECVD) was significantly higher than those prepared by physical vapor deposition (PVD), which is due to the lower kinetic energies of particles used in PECVD [62-64]. Other diverse methods were suggested to improve the efficiency of cBN-based applications by coating using TiCN or AlTiN binders [65], doping of thin films with anions [66, 67].

2.2. Theoretical and experimental background

It has been shown that the physical properties (e.g. micro-hardness, electrical and heat conductivity) and the mechanical properties (e.g. shear modulus, wear resistance, toughness) of PcBN and Ti(C,N)-based cermets are influenced by the binder metal phases, and can be improved by optimizing the microstructure and composition [68-71]. These studies showed that the best way to improve the properties of PcBN is to reduce the grain size of the hard phase and to increase the homogeneity of the structural elements. Both features depend on the method of preparation. Mechanical alloying is a versatile method of production that allows production of homogenised and nano – structured materials [6, 71-88].

Several methods of producing dense, sintered, translucent cBN bodies without additional sintering agents have been reported [89-92]. These methods involved either the direct conversion of deoxidized hexagonal BN (hBN) to cBN at 7.7GPa and between 2000 and 2500˚C, or direct sintering of cBN powder at 7.7GPa above 2000˚C. Control of the grain size appeared to be easier when cBN powder was used as the starting material [90]. Although the HPHT technology is well developed, there still exists some shortcomings, e.g. the sizes of samples are small, the equipment is hard to maintain, and the costs are high. To resolve these problems, many researchers have developed some novel preparation methods. Zhao and Wang [15, 93] used the spark plasma sintering (SPS) to prepare PcBN at temperatures ranging between 1250˚C and 1450˚C and a heating rate of 300˚C/min. A novel pressureless sintering method to prepare PcBN compact was investigated by Ren *et al.* [94]. Their work showed that feldspar was an excellent fusing agent, which reduced the sintering temperature to between 900˚C and 1200˚C, and also improved the density of the compacts. However, the sintering time was longer than in HPHT, up to 4h.

Aluminium is frequently used to assist sintering of cBN, and AlN can be formed through the reaction with cBN [93], which acts as a binder among grains. Unfortunately, the other products such as AlB_2 and AlB_{12} were reported to degrade the mechanical strength of the composite [95, 96]. The cBN could also be sintered with AlN as an additive to avoid the appearance of AlB_2 and AlB_{12} [47-97]. Liquid phase sintering enhanced the reactions in the cBN-Al system, which led to the formation of AlN and AlB_2. Conversely, in the cBN-AlN system, AlN grains agglomerated heavily below 1500˚C and Al_2O_3 appeared, and

the agglomeration disappeared gradually as the sintering temperature increased. The corresponding microstructure and the phases formed are shown in Figure 2.1 [48]. These results suggested that the cBN-Al system was more favourable to obtain well-sintered cBN compacts, compared with the cBN-AlN system, as shown in Figure 2.2 [48].

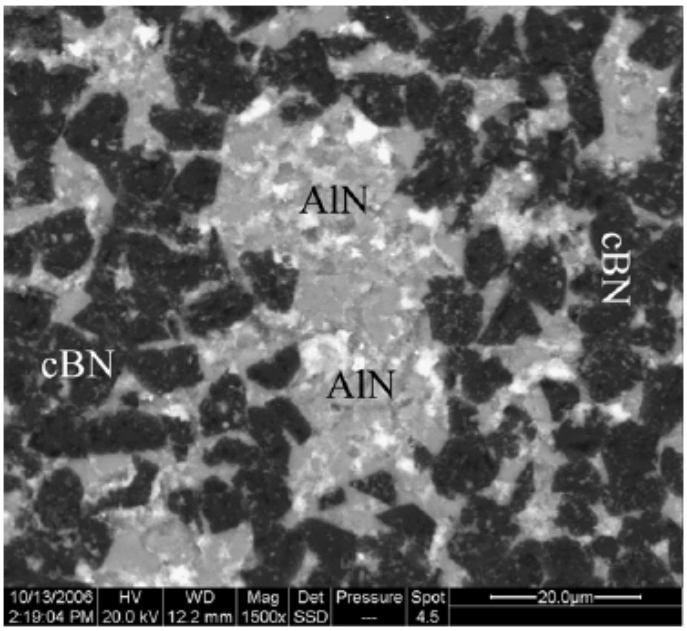

Figure 2.1. BSE – SEM micrograh showing the interfaces between AlN-rich and cBN-rich zones sintered at 1400˚C [48]

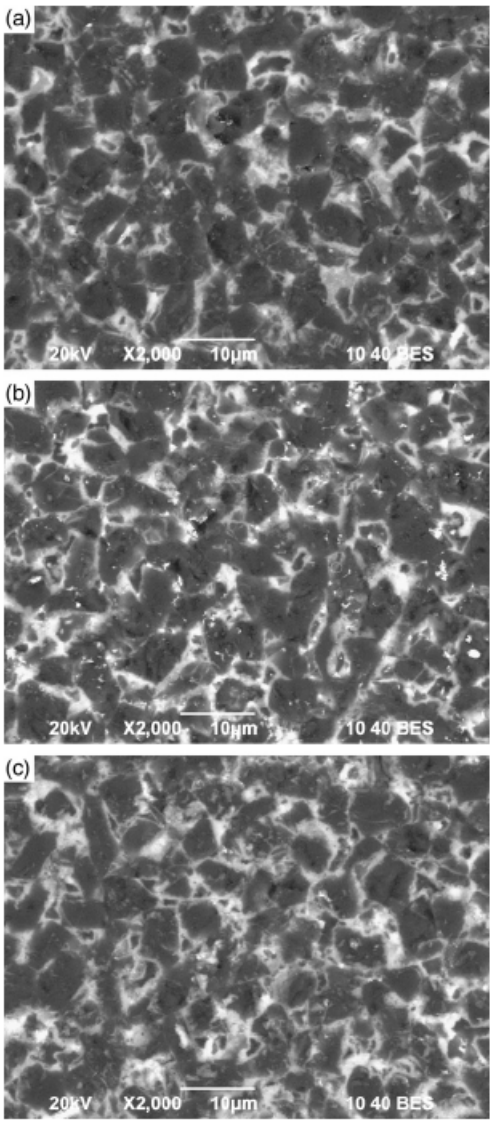

Figure 2.2. BSE – SEM micrographs of PcBN from cBN – 15wt% Al sintered at (a) 1300˚C, (b) at 1400˚C and (c) at 1500˚C under 5.0GPa for 20 minutes [48].

The addition of nano-diamond was shown to increase the density and strength of PcBN, and reduced the 'bridging effect', J_b, which represents the energy required for crack propagation by grain pull out and rupture [98].

2.3. Mechanical alloying and mechanochemical synthesis

Mechanical alloying (MA) was initially developed in the 1970s at the International Nickel Co. (INCO) as a technique for dispersing nanosized oxide inclusions into Ni-based alloys [6]. The mechanical alloying induced amorphization was demonstrated in subsequently using high energy ball milling [1-5, 72-77]. Mechanical alloying is a unique process in that a solid state reaction takes place between the fresh powder surfaces of the reactant materials at relatively low temperature.

Amongst the different options for preparation, the MA method has been considered the most powerful tool for nano-structured materials, because of its simplicity, relatively inexpensive equipment, and the possibility of producing large quantities that can be scaled up to several tons [6]. Traditionally, the raw materials used in mechanical alloying must include at least one fairly ductile metal to act as a host to hold together the other ingredients. The milling intensity that determines the average temperature rise during ball impacts and the energy storage in the powder particles determine the crystalline state of the milled products [3, 5, 7, 8, 72].

Detailed analyses of amorphization by MA in the Ni – Ti [73] and Fe – Zr [74] systems showed that amorphization was not caused by rapid quenching of molten surface regions owing to the high energy input during ball milling, but rather by a mechanical metastable thermodynamic equilibrium process. The amorphization by mechanical alloying was attributed to mechanical mixing and to a solid state interdiffusion reaction taking place at clean boundaries between polycrystalline Ni and Ti. Therefore, a close relation to

amorphization by solid state reaction could exist. This corresponds to a thermodynamic description in which a large negative enthalpy of mixing favors the amorphous phase compared with the crystalline composite of the elements [73, 74].

Mechanical alloying allows the broadening of compositional ranges of phases, making the preparation of quasi-crystals technologically easier [76, 76]. Moreover, all reactions proceed in the solid state, which helps to overcome the complex behaviour of solidification during conventional casting or condensation from vapors. Mechanical alloying was also shown to be beneficial as an interim manufacturing step to prepare three-phase alloys with a continuous matrix containing uniformly distributed intermetallic particles. Supersaturated solid solutions can also be obtained [77].

During the mechanical alloying process, the powder particles are periodically trapped between colliding balls and are plastically deformed by the generation of a wide number of dislocations, as well as other lattice defects [1-6]. The ball collisions cause fracturing and cold welding of the elementary particles, forming clean interfaces at the atomic scale. Further milling leads to an increase of the interface number and the sizes of the elementary component areas decrease from millimeter to sub-micrometer lengths. Concurrently to this decrease of the elementary distribution, some nanocrystalline intermediate phases are produced inside or at the surface of the particles. The end product depends on the milling conditions. The general behavior of the powders particles during mechanical alloying is shown schematically in Figure 2.3 [99].

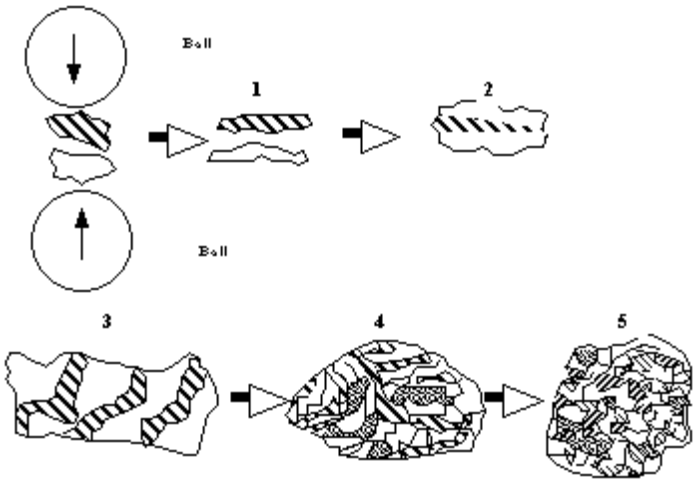

Figure 2.3. Schematic representation of the general behaviour of the powder particles during high energy ball milling [99]

Two types of machines used in high energy ball milling and mechanical alloying are illustrated in Figure 2.4. The grinding bowls of the planetary ball mill (Figure 2.4.a) move around own axis and in the opposite direction around the common axis of the sun wheel. Thus, the superposition of the centrifugal forces changes constantly (Coriolis' motion). The grinding balls describe a semi-circular movement, separate from the inside wall, and collide with the opposite surface at high impact energy. The impact and friction forces are the reasons for the high size reduction power of these equipments. High energy attritors with horizontal axis (Figure 2.4.b) have been developed by Zoz Maschinenbau GmbH for laboratory application, as for commercial use.

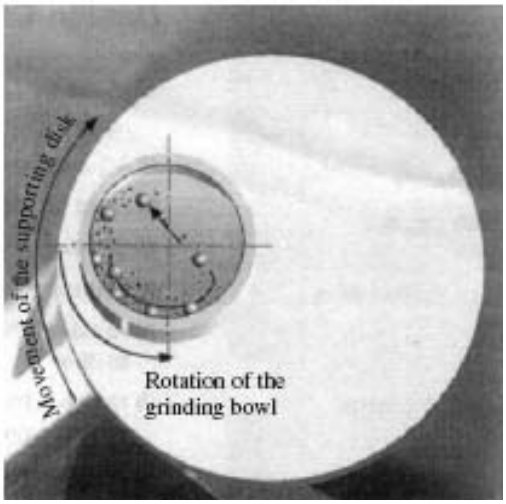

2.4.a

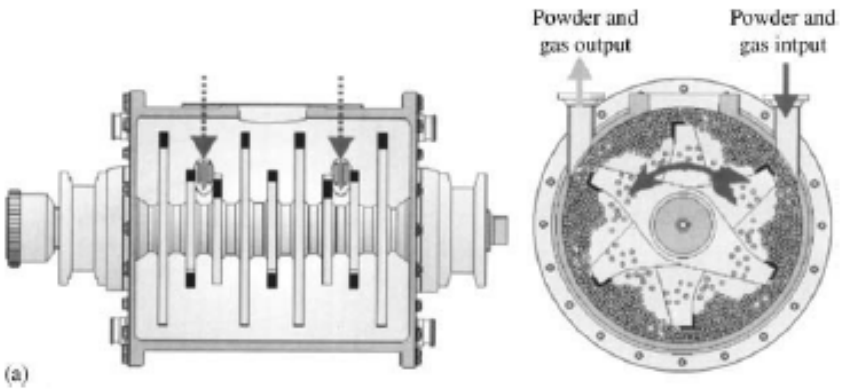

2.4.b

Figure 2.4. Schematic representations of high energy ball mills used for MA:

2.4.(a) planetary ball milling machine and 2.4.(b) roller ball milling machine [6].

There are several explanations of the mechanism of mechanical alloying. The “Thermal theory” reasons that the activation of chemical processes is provided by heat caused by friction and collision of particles with the grinding medium and with each other. The “Dislocation theory” reasons that the activation occurs at the expense of energy of exit dislocations on the particles which are being ground. In a third approach, the activation of chemical processes is connected with the “trip-out” of a resilient energy at the destruction of the solid and with the formation of short-lived active centers [1-6]. The presence of numerous effects, such as luminescence, emission of electrons and other charged particles, the appearance of electric charges on the surface and “evaporation” of crystal lattice components, led to the creation of the “deformation” model. The above models, without exception, complement each other [6, 79, 80, 85-88,100].

The mechanisms leading to phase transitions during high energy ball milling and mechanical alloying are still in discussion from a fundamental point of view [6]. Nevertheless, some points are discussed more, e.g. the available mechanical energy which is produced by the various milling machines. Mechanical milling energy has been compared to some other solid / liquid state processes leading to phase transitions under various conditions, as illustrated in Figure 2.5.

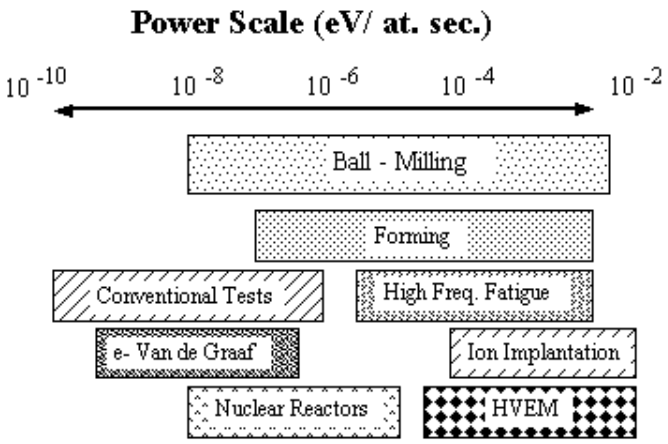

Figure 2.5. Comparison of the injected power expressed in eV / at.sec as a function of the various solid / liquid state processing leading to phase transitions under various conditions [79, 80, 100].

An equivalent time approach for scaling the mechanical alloying processes based on the dynamics of a single ball into a planetary ball mill was described by Ipus *et al.* [78]. The model led to a cubic dependence of the power transferred to the powder with the rotational speed of the main disc. This yield the definition of an equivalent time:

$$t_{eq} = t\left(\frac{\Omega}{\Omega_0}\right)^3 \qquad \text{Equation (2.1)}$$

where Ω_0 and Ω are two rotation speeds, t_{eq} and t are the corresponding milling times to achieve the same amount of energy transfer to the powder particles. Results of this model have been applied to powder particle size, contamination, microstructure and magnetic properties evolution of a 75Fe – 20Ge – 5Nb alloy obtained by ball milling from pure powders [78]. A study by Maweja and Phasha [7, 8] on the metastable 50Mg – 50Ti system instead concluded at a square dependence of the transferred power to the powder with the rotational speed.

The influence of milling parameters in manufacturing Fe-TiCN using high energy ball milling was investigated by Gordo *et al.* [79] and by Gómez *et al.* [80]. They observed that not only the oxygen content was important for the compositional characteristics of the powders obtained, but also the C/N ratio was important, as it had an influence on the microstructure and increased the micro-hardness of the sintered materials. They also observed that milling under argon yielded even finer and homogeneous microstructures than milling under N_2 - $9.9H_2$ - $0.1CH_4$ or in air. The milling atmosphere was seen to be the most influential factor in the composition of the powders, whereas the type of mill and the milling time affected the morphology and microstructure of the products.

Córdoba *et al.* [71] synthesed TiC_xN_{1-x} – (Co/Ni) powdered cermets by a one step mechanically induced self-sustaining reaction (MSR) process from mixtures of elemental powders, and subsequent sintering showed that the final morphology of the ceramic was dependent on the C/N ratio of TiC_xN_{1-x}. They also suggested that the presence of Ti in the binder reduced hard particle solubility in the melted binder and its subsequent grain growth.

Attempts to mechanically alloy all-ceramic components (instead of metal-metal or metal-ceramic systems) were done by Zhang and co-workers [81, 82]. They prepared $Ti(C_{0.3}N_{0.7})$ –WC – TaC and TiC – TiN solid solutions using a Fritsch P5 planetary ball mill. They reported that it was difficult to completely dissolve WC into Ti(C,N).

Increasing milling time and intensity extended the solubility and enhanced the phase transitions by ball milling [85, 86]. The lack of quasi-crystalline phase formation in some zirconium glassy alloys prepared by mechanical alloying with respect to melt-spun material was believed to indicate that the formation of icosahedra quasi-crystalline short-range order was strongly affected by the processing route used [87]. However, ball milling is an extremely complicated processing route in which several factors, such as impurity contamination, may play a role and cannot be considered merely as a deformation process. It was established that an oxygen at level as low as 0.3 wt% significantly increased both the glass transition and the crystallization temperatures of some Zr-based MA powders [87].

One serious problem in the processing of metallic materials by ball milling techniques is the potential contamination from the milling media or atmosphere. The small size of the powder particles and the consequent availability of large surface area, along with the continuous formation of new fresh surfaces during milling, contribute to the contamination of the powder [6, 87, 88].

2.4. Thermodynamic and kinetic considerations on mechanical alloying

Computational thermodynamics has evolved to a point where complex material thermodynamics problems can be solved with relative ease. Cases involving various degrees of non-equilibrium and therefore time-dependence have been reported [101-103].

Mechanical alloying is a process that transfers high amounts of energy from the balls to the powder during the milling step [6, 104]. The stored energy results from intense plastic deformation of the powder particles, which creates a high crystallite defect density such as dislocations and grain boundaries, which increase the free energy of the system. Departure from equilibrium achieved for some processes are given in Table 2.3 [104].

Table 2.3. Departure from equilibrium achieved for various processes [104].

Processes	**Maximum departure from equilibrium [kJ/mol]**
Solid-state quench	16
Quench from liquid (rapid solidification)	24
Condensation from vapor	160
Ion implantation	30
Mechanical cold work	11
Mechanical alloying	30

The grain size decreases as the milling time increases. The dislocation density increases after short milling time, and after decreases. This was attributed to the fact when particle sizes reach a saturation value, continued milling would not produce more dislocations due to the difficulty of generating dislocations at small grain sizes, although existing dislocations will be rearranged and some will be annihilated. Therefore the dislocation density decreases [6].

The free energy increase due to the grain size decrease can be determined by means of Equation 2.2 [105], where γ is the grain boundary energy, $\frac{A}{V}$ the surface/volume ratio and V_m is the molar volume. A cubic or spherical form of grain size is assumed to estimate the *A/V* ratio.

$$\Delta G_b = \gamma\left(\frac{A}{V}\right)V_m \tag{2.2}$$

The free energy change due to variation of dislocation density can be calculated using Equation 2.3 [105], where ξ is the dislocation elastic energy per unit length of dislocation lines and ρ is the dislocation density. The smallest grain size, *L*, can be estimated, for one metal, using Equation (2.4) proposed by Nieh and Wadsworth [106], where *G* is the shear modulus, *b* the burger vector, *v* the Poisson's modulus and *H* is hardness.

$$\Delta G_d = \xi\rho V_m \tag{2.3}$$

$$L = \frac{3Gb}{\pi(1-\nu)H} \tag{2.4}$$

The above mentioned model was applied and showed that the energy resulting from the MA process increased the crystalline defect density. Thus, the stored energy was sufficient to increase the solubility between metal systems which had positive Gibbs free energy of mixing [107]. The authors suggested that surface energy had a larger influence compared with elastic strain energy due to the presence of dislocations on free energy and solid solubility.

The fundamental properties which are thought to be the most possible metallurgical factors in determining the MA process between metals are:

- the crystal structure at about 100 – 200˚C that is the typical temperature measured during MA [108]
- the atomic size
- the self-diffusion coefficients at the milling temperature
- and the melting point [109].

Chen *et al.* [110] suggested that the dominating factor was the melting temperature of the elements, and higher melting temperatures would give lower alloying rates. They also reported that elements with better malleability, such as Al, can be spread out faster, and in the latter stage, they can diffuse at a faster rate into other elements or solution phases.

It was shown that it is possible to obtain information about the kinetics of structural relaxation from thermograms similar to Figure 2.6. The main difficulty lies in the fact that, in contrast to crystallization, structural relaxation does not occur around a peak temperature [111, 112].

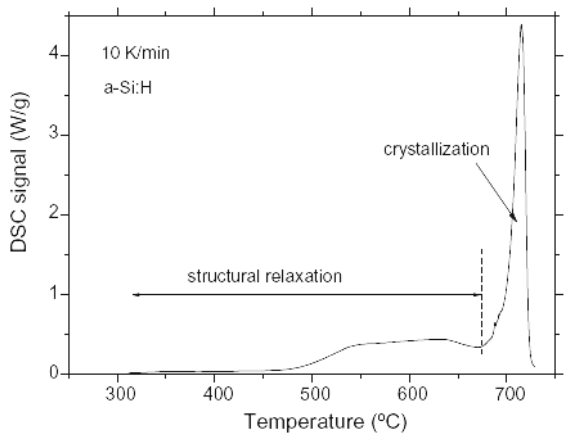

Figure 2.6. DSC thermogram of hydrogenated amorphous silicon showing the relaxation and crystallization signals [111].

2.5. Analysis techniques

The realization that a variety of useful properties and novel physical effects could emerge from the study of real, imperfectly ordered materials has grown in the last decades. The microstructure of such a material is characterized by the size, shape, crystal structure, volume fraction, and topological arrangement of the phases that it contains, and by defects such as point defects, dislocations, grain boundaries, and interphase boundaries incorporated in, or bounding, the phases. Owing to the great variety of possible phases and defects, their spatial arrangements, and not least to their mutual interactions, understanding the relationship between microstructure and properties remains one of the greatest challenges in materials science [113].

A method for the determination of the particle size distribution and dislocation density in nano-structured materials was developed and applied to various metals and ceramics in deformed conditions [114 – 120]. This model takes into account that the contrast caused by dislocations depends on the relative directions of line and Burgers vectors of the

dislocations and the diffraction vector. Anisotropic contrast can thus be summarized in contrast factor, *C*, which can be calculated numerically on the basis of the crystallography of the dislocations and the elastic constants of the crystal. An evaluation of the X-ray diffraction profiles by means of the Williamson-Hall and Warren-Averbach methods is summarized below.

Assuming that the strain broadening is caused by dislocations, the full widths at half maximum (FWHM) of the diffraction profiles can be given by the modified Williamson-Hall plot as [121]:

$$\Delta K = \gamma / D + \alpha\left(K\overline{C}^{1/2}\right) + O\left(K^2 C\right), \qquad (5)$$

where *D* is a size parameter characterizing the column lengths in the specimen, γ equals 0.9, α is a constant depending on the effective outer cut-off radius, the Burgers vector and the density of dislocations, *C* is the contrast factor of dislocations depending on the relative positions of the diffraction vector and the Burgers and line vectors of the dislocations and on the dislocation character and *O* stands for higher order terms in $K\overline{C}^{1/2}$. *K* is the length of the diffraction vector: $K = 2\sin\theta / \lambda$, where θ is the diffraction angle and λ is the wavelength of X-rays. $\Delta K = \cos\theta\left[\Delta(2\theta)\right]/\lambda$, where $\Delta(2\theta)$ is the FWHM of the diffraction peak. The size parameter corresponding to the FWHM, *D*, is obtained from the intercept at *K*=0 of a smooth curve according to Equation (5).

$\overline{C}$ factors can be determined using the modified Williamson-Hall plot without the knowledge of the arrangement of the existing dislocations.

The dislocation density is determined using the Warren-Averbach Equation (6) [123].

$$\ln A(L) \cong \ln A^S(L) - \rho B L^2 \ln\frac{Re}{L}\left(K^2 C\right) + O\left(K^4 \overline{C}^2\right) \qquad (6)$$

where *A(L)* is the absolute value of the Fourier coefficients of the diffraction profiles, A^S is the size Fourier coefficient as defined by Warren [124], ρ is the dislocation density, $B = \pi b^2/2$ (b is the length of the Burgers vector), *Re* is the effective outer cut-off radius of dislocations and *O* stands for higher order terms. *L* is the Fourier length defined as [125, 126]

$$L = na_3, \qquad (7)$$

where $a_3 = \lambda/2(\sin\theta_2 - \sin\theta_1)$, *n* is an integer starting from zero and $(\theta_1 - \theta_2)$ is the angular range of the measured diffraction profile.

Numerically solving the equations gives for PcBN the bulk modulus *B* = 400 GPa, the shear modulus $\overline{G}$ = 405 GPa, the elastic modulus $\overline{E}$ = 909 GPa and the Poisson's ratio $\overline{\nu}$ = 0.121 [127-129].

The Young's modulus and shear modulus of the PcBN obtained without mixing with any binder attained their maximum values for sintering temperatures of 2200 and 2350˚C for starting cBN particle sizes of 2 – 4 or 8 – 12μm, respectively. At a sintering temperature of 2100˚C, the modulus values were significantly less, suggesting incomplete sintering. The optimum sintering conditions occurred at a slightly higher temperature for coarse cBN starting material [130].

Harris *et al.* [131] investigated the flow stress at high temperature for a range of PcBN cutting tools. The materials consisted of 90 wt% PcBN and three PcBN/TiC composite materials corresponding to 80, 50 and 45 wt% cBN brazed onto WC/Co substrates for support. The authors identified the onset of plastic deformation, or flow stress, in the temperature range 800 – 1200˚C for all materials tested. The flow stress and room temperature hardness decreased with increased TiC content. Transgranular fracture occurred in the PcBN aggregate, whereas intergranular fracture was characteristic in the cBN/TiC composite materials.

The microstructure of nano-structured materials can be effectively studied by X-ray diffraction line profile analysis. Crystallite size and strain effects acting concurrently cause the broadening of a profile. In plastically deformed metals and ceramics, the lattice distortions are mainly caused by dislocations, so the strain broadening can be expressed in terms of the dislocation structure [132-138]. The Multiple Whole Profile (MWP) fitting method is used, in which the measured profiles are fitted by theoretical functions calculated on the basis of the model of microstructure. This procedure yields both the crystallite size distribution and the characteristic parameters of the dislocation structure in nano-structured materials. The crystallites are assumed to have spherical shapes with log-normal size distributions [139].

The thermal stability of the microstructure is commonly examined by differential scanning calorimetry. It was shown that the maximum of the exothermic peak in the DSC

trace shifted to lower temperature values and the heat released during the annealing increased with increased strain in a heavily deformed copper specimen [118].

2.6. Modelling of mechanical alloying

Among the observed phenomena in MA are supersaturated solid solutions, metastable phase formation, and amorphous and nanostructured materials. An excellent summary of the available experimental information is contained in the review by Suryanarayana [6]. It is possible to obtain very large solubility, even in systems where no observable solubility has been found under equilibrium conditions. Much attention has been given to investigating the effect of variation in parameters such as milling speed, milling time, powder size, ball-to-powder weight ratio and milling temperature on the final phase constitution. In contrast, much less attention has been given to the quantitative determination of the energy imparted to the powder components during the ball milling process.

The stored energy can be very significant, and the magnitudes of the measured enthalpies, together with the frequently observed extended solubility imply that the mechanical energy imparted by the alloying process results in changes to the equilibrium Gibbs energies of the alloy components. These changes can be compared to thermodynamic calculations to simulate the extended solubility in a particular alloy system. In the case of MA, temperatures during the process are generally low and it is anticipated that, owing to restricted diffusion, the formation of less complex single-phase structures is favoured [6].

Battezzati [140] used the results of different workers to plot the energy release from ball milled copper as a function of annealing temperature. It was evident from his investigations that the energy imparted to powdered metals by the ball milling process must be taken into consideration in calculations of the phase equilibria resulting from the particular alloying process concerned. Spencer [141] calculated metastable phases and their ranges in various systems, e.g. Al – Mn, Cr – Co, Al – Ti and Fe – Ni. He assumed the following:

- The component Gibbs energies are modified by quantities corresponding to the energy imparted to the component powders by the mechanical alloying process,
- The observed phase is the homogeneous single close-packed phase with the lowest Gibbs energy for an overall alloy composition, and
- Solubility boundaries are given by the points of intersection of the Gibbs energy curves for the single phases.

For all calculations, Spencer used the well-established modeling and calculation methods presented by Wang [142]. Spencer concluded that more detailed experimental investigations incorporating both systematic measurement of the energy imparted to powder components during milling and metallographic of the phases precipitating were needed to achieve better thermodynamic modeling and interpretation of the phases formed.

The maximum entropy principle (MEP) introduced by Jaynes [143] has been successfully applied to many engineering problems arising in a wide variety of fields. The MEP allows one to determine the least biased probability distribution function when the

information available is limited by some constraints. The process which gives the maximum value of the informational entropy, $H[f(x)]$, may be described by:

$$H[f(x)] = -\oint_E f_U(x).\ln[f_U(x)]dx \Rightarrow \max \qquad (8)$$

where $f_U(x)$ is a function which approximates the unknown probability distribution *f(x)*. From the practical point of view, the progress of the grinding process may be described using the kinetic equation including the intensity of the process [144]. More applicable is the full statistical description of the particle size reduction (PSR) during the grinding process [145].

A conception of the total mass related energy input, E_M, for a grinding process with particles has been considered [146, 147]. This total energy input may be expressed as follows:

$$\int_0^{y_{\max}} \int_0^{y} T(x,y)C(x,y)f_s(y)dxdy = E_M \qquad (9)$$

where *C(x,y)* is the energy transition function written in the following form:

$$C(x,y) = c_k \ln\left(\frac{y}{x}\right) \qquad (10)$$

Equation 10 is the so-called law of breakage or Kick's hypothesis [145]. The constant factor, c_k, is dependent on the material properties and the shape of granular material elements.

Rakoczy [145] suggested that the particle size mean value, d_{avg}, and the standard deviation, σ, were dependent on the operational parameters, such as milling time and diameter of particles, and obeyed exponential laws such as:

$$d_{avg}(t,d,w) = p_1(d,w)\exp[p_2(d,w)t] \quad (11)$$

$$\sigma(t,d,w) = p_3(d,w)\exp[p_4(d,w)t] \quad (12)$$

The coefficients $p_1(d,w)$ through to $p_4(d,w)$ are given by the combination of three parameters depending on the milling time and speed (w), and the initial particle size d.

The following phenomena may take place, and are of interest, in the course of ball milling: size reduction (dry or wet; with or without additives); mechanochemical transformation (amorphization, surface activation; polymorphic transformation; chemical reaction etc.); mechanical alloying and wearing of the mill parts. An energetic approach to the kinetics of a batch ball milling was developed by Kheifets and Lin [148], which enables the comparison and the reproducibility of a milling process, particularly the mill scale-up.

The description of milling as a rate process is often based on a population balance linear integro-differential equation derived by Gaudin and Meloy [149]

$$\frac{\partial m(x,t)}{\partial t} = -S(x)m(x,t) + \int_x^\infty S(y)\frac{\partial B(y,x)}{\partial x}m(y,t)dy \quad (13)$$

where t is the current time, $m(x,t)$ is the density distribution function for which $m(x,t)\partial x$ is the mass fraction of particles in an infinitesimal size range x to $x+dx$; $S(x)$. The selection function, also called the rate function, is equal to the mass fraction of particles of size x selected for breakage per unit time. $B(y,x)$ is the mass of progeny particles of sizes less than x when a unit mass of particles of size y are broken.

Proceeding from Equation 13, Kapur and Fuerstenau suggested a general grinding time-size reduction relationship [150]:

$$\frac{d\mu_1(t)}{dt} = -C\mu_1^n \tag{14}$$

where C and n are constants, and μ_1 is the first moment of the particle size distribution (which is called 'mean size'):

$$\mu_1(t) = \int_0^\infty m(x,t)x dx \tag{15}$$

Taking into account $dE=Pdt$, where E is the net energy input to grinding mill and P is the net power draft, Kapur and Fuerstenau [150] derived the well-known master energy-size reduction relationship:

$$\frac{d\mu_1}{dE} = -\varepsilon.\mu_1^n \tag{16}$$

where they considered factor ε as constant. The authors showed that the most common descriptive measures of fineness such as mean, median, percentiles, specific surface area,

are interchangeable; so the expression shown in Equation 16 can be applied to all these values.

Kheifets and Lin [148] suggested taking into account the 'energetic efficiency', $\eta = \frac{U}{E}$, where U is the actual energy uptake in the substance during milling, and the milling intensity. They proposed a general form of this dependence as an Arrhenius equation;

$$\eta = \eta_0 \exp\left[-E_a/(I - I_0)\right] \tag{17}$$

where η_0 is the maximum energetic efficiency, E_a is the activation energy, I is the actual intensity of treatment, and I_0 is the critical (threshold) intensity. The maximum of η is about 0.25 to 0.30 due to inevitable heat evolution [151]. The dimensionless group proposed for modeling and scaling is the intensity number defined as:

$$In = \frac{I - I_0}{E_a} \tag{18}$$

where In is a measure of relation of the energetic potential of the ball media of a mill and the substance treated. The intensity of treatment in a mill with loose balls characterized by the angular frequency is given by:

$$I = \frac{P}{m_s . f}, \text{ J/kg} \tag{19}$$

where m_s is the mass of substance being treated, $f = \omega/2\pi$ is the frequency.

The survey on industrial and theoretical backgrounds of mechanical alloying by high energy ball milling and HPHT sintering of polycrystalline cubic boron nitride demonstrate the complexities and challenges inherent to these two processes. Much work has been done worldwide to develop understanding of the driving forces and kinetics of the two processes. However, the issue of advanced binder phases for PcBN composites with multiple phases was identified as a cause of low performance of the PcBN cutting tools. The present study investigated the mechanism of formation of ceramic-metals solid solutions by mechanical alloying and the benefit of using these materials in sintering of PcBN composites. The rationales for this investigation are presented in Chapter 3.

CHAPTER 3. MATERIALS AND EXPERIMENTS

3.1. Rationale and hypotheses – Alternative binder materials for cBN

1. Primary cBN binder materials found in commercial products are Co – W – B, AlN, TiN, TiC, TiCN, TiB_2, HfC and TaC [10]. Among these, TiN, TiC and TiCN based cBN composites are superior in their wear resistance in the turning SKD11 test and APT - milling test [10]. Pure cBN compacts are difficult to prepare, even using high pressure high temperature (HPHT) techniques [152]. To assist sintering cBN, aluminium is frequently used as an additive, and AlN can be formed through the reaction of Al and cBN. Other reaction products, such as AlB_2 and AlB_{12}, were reported to degrade the mechanical strength of the composite [40, 153]. The cBN compacts could also be sintered under HPHT with AlN as an additive to avoid the appearance of AlB_2 and AlB_{12}.

Thus, mechanical alloying by dissolution of W into the titanium carbonitride prior to, or simultaneously with, Al addition in the binding mixture may enhance the formation of ternary Ti-W- Al compounds and prevent the formation of the binary AlB_2 and AlB_{12} or similar titanium-borides.

2. It is accepted that strong ceramic-ceramic bonding is essential for high strength cBN composites due to the dominance of intergranular fracture [154]. Good bonding between cBN and the binder phase usually occurs when the hard phase has a small amount of solubility in the binder phase.

Therefore, Al or pre-reacted Al alloys are generally mixed with cBN particles to improve bonding between phases by reactive-liquid phase sintering. According to Sumitomo [155], if the Al content exceeds 20wt% in the binder material, hardness will be significantly reduced. Therefore, sub-stoichiometric Ti-containing phases are also added to further enhance chemical reaction with cBN and to form TiB_2 and TiN, both of which are harder than AlN [10, 155].

It is hence hypothesised in this work that the introduction of a refractory metal into the binder composition may overcome the drawback due to the low melting temperature of the necessary aluminium.

3. BN + TiC – TiN – TiB_2 were synthesized in situ by sintering a 70h – milled mixture of Ti and amorphous BN (aBN) powders of nanometre size at 5GPa and 1300˚C [156, 157]. The powders prepared by ball milling benefited by increasing solid-state reaction activity between Ti and aBN and decreasing synthesis temperature and time. Higher temperatures and longer times of sintering could increase the content of TiB_2 and TiN in the composites. The samples sintered at 5GPa and 1300˚C had their highest hardness, 8.8GPa, which is lower than reported [45, 158], when the composites were prepared at 1600 - 1800˚C.

It is believed that high sintering temperature can eliminate the pores in the composite during the solid-state diffusion reaction and improve the hardness.

4. One of the most important parameters affecting strength is the homogeneity of the composite matrix within micro volumes [159]. Based on the Griffiths' law of brittle fracture [160, 161, 162, 163], agglomerated cBN and/or binder phase particles behave like large particles which exhibit less resistance to crack initiation [164].

Therefore, fine particle size materials and uniform and well distributed hard particles are favoured to increase strength.

5. Agglomeration of particles is generally associated with milling and mixing of fine and ultra-fine particles [1-6].

Since mixing efficiency decreases with decreasing particle size, the tendency toward agglomeration may be prevented by addition of suitable dispersant agents (process control agents) into the milling slurry.

6. Homogeneous distribution of particles in a composite matrix can be achieved, even for sub-micron particles, by improving communition techniques.

High energy ball milling may be an appropriate means of achieving homogeneous distribution of phases in nanostructured materials

7. Since sintering of composites involves chemical interaction between the binder phase and hard phase particles, inhomogeneous distribution of phases may form an excess amount of localised brittle phases in the matrix.

High energy ball milling of the binder constituents can improve the homogeneity and the coefficients of diffusion between the phases in presence during the HPHT sintering of cubic boron nitride.

8. Particle size distribution may affect the mixing and homogenisation of powders. It also plays a role in the early milling stage where fracturing and cold welding processes are dominant. The effect of particle size would be more significant when large particles of a soft material powder are milled with fine particles of a hard material [4, 6]. Fracturing would be slow in this case, whereas particle size reduction is fast during high energy ball milling of ceramics and hard metals. However, mechanical alloying is driven by the lattice strain energy stored in crystals, which contribute to the driving force for transformations [4, 6, 8, 35].

Large starting powder particles will introduce less oxygen in the milling media than fine powders would. Therefore large powder particles of hard W were used to investigate the behaviour (fracturing versus cold welding) of hard particles in early milling stage, its effects on the kinetics of alloying and on the order of destruction of crystalline structures of mixture constituents, which determines the solute and the solvent.

3.2. Variables considered in experiments

3.2.1. Independent variables

Mechanical alloying of elemental powders is strongly dependent on the amount of energy input during the high energy ball milling process [2-5, 72]. Experimental and theoretical models have shown that the mixture composition, milling atmosphere, milling time and the nature of milling balls determined the properties of the milled powders [7, 8, 78-83]. The mixture composition determines the chemistry, morphology and structure of the final product. The transformation mechanism that defines the intermediate products formed, and the solid solution mechanism occurring during high energy ball milling of powders of crystalline metals or ceramics are equally dependent on the crystallography and physical properties of the substances present. The rates of interdiffusion and dissolution between the elements and/or compounds at room temperature are attributed to the nature of the substances under consideration.

Chemical reactions of atoms from the milling atmosphere with the activated powder particles would affect the nature of the intermediate as well as the final phases. Adsorption of atoms from the milling atmosphere onto the surface of the milled powder particles is another possible interaction with the evolving products [6, 71, 72].

Milling time is the most basic variable for monitoring the kinetics of occurring transformations and reactions during high energy ball milling. The energy efficiency, the yield and the scaling factors are commonly defined on a time base scale. The mechanical

energy input into the system increases with the milling time. The physical properties of the milled products evolve with the milling time.

The milling media, characterized by the constitution of the milling balls and milling pots, would have an effect on the mechanical total energy input of the system, and hence on the kinetics of the occurring transformations. The density, size and the number of the milling balls determine the kinetic energy and the pressure applied on the powder particles trapped in between the moving balls at a given rotation speed of the ball mill machine. Another effect of the nature of the milling media on the mechanical alloying process is through contamination. Some milling media materials would have a catalytic effect (activating or retarding) on the kinetics of the mechanical alloying process.

The experimental and theoretical models suggest that the rotation speed and the milling time are ultimately linked to the kinetics of transformations by the effect of the kinetic energy of the milling balls [2-5, 72, 7, 8, 78-83, 141-151].
Hence, after choosing to describe the kinetics of MA in the time domain, the conversion to the energy domain could be done using the existing models.

Preliminary experiments conducted in this work on the amount of PCA to be added to minimize the cold welding of the powder particles and their adhesion on the contact surfaces with the milling media showed that the optimum comprised between 3 and 6 wt% for milling time of up to 48h. Excessive amounts of PCA could lead to

contamination of the milled product, or to excessive oxygen sensitivity which leads to spontaneous combustion of the milled powders.

Milling started at room temperature (~25˚C). The temperature increased as the milling time increased to a maximum of about 150˚C to 160˚C. It was assumed that the heat effect on the solid state diffusion and transformations was identical in all the experiments because of the similarity of the maximum temperatures reached. Hence, temperature was also considered as a parameter during the investigations.

3.2.2. Dependent variables selected to monitor the process

The reactions and transformations during ball milling were monitored in the time domain by means of five dependent variables or functions. The particle size distribution of the milled products was characterized in order to determine the efficiency of the crushing process. The analysis of the particle size distribution is a key factor in optimizing the energy consumption involved in this process.
Energy consumption is the critical design factor of ball milling processes because it may constitute the major drawback in implementing such technique in industry.

Contamination of the milled products by oxygen from the milling atmosphere and from the process control agent, and by the constituents from the milling media were analysed as these may affect the microstructure and performance of the final products.
Contamination from the milling media can occur due to interdiffusion or to mechanical

erosion of the balls and pots. Chemical analysis of the products enabled the determination of the extent of these causes of contamination.

The evolution of the crystal structures, crystallite sizes and strains allowed the identification of the transformation steps during milling, and the corresponding driving forces. Thus, the mechanism of alloying and reactions could be described with respect to the changes in crystal structures of the powders. The relationships between the independent and dependent variables were examined through a range of experiments and analyses described in Section 3.3.

3.3. Experiments

3.3.1. High energy ball milling and alloying of the powder constituents

Mechanical alloying tests were undertaken on mixtures of the sub-stoichiometric $Ti(C_{0.5}.N_{0.05})$ or $Ti(C_{0.5}N_{0.5})_{0.6}$ with elemental W powder. The mixtures were processed by a Retsch planetary high energy ball mill PM400 *MA – type*.
Another type of mixture contained the Ti(C,N), W and Al powders. The difference in composition between these two types of mixtures was to determine the effect of Al on the mechanism of solid solution between the sub-stoichiometric Ti(C,N) and W, and on the phases formed during ball milling.

By adding Al to the starting powders, the effect on the homogeneity of the binder phase formed in HPHT sintering of PcBN was to investigated. The structural and composition

heterogeneities in the binder phase and the formation of the brittle binary aluminide phases are practical issues encountered in PcBN sintering using Al-containing binders, as described in Chapter 2.

The proportion of Ti(C,N) and W in the mixtures were selected to obtain Ti and W contents near the monotectoid composition as defined in the equilibrium phase diagram in Figure 1. Hence, powders of $Ti(C_{0.5}N_{0.05})$ or $Ti(C_{0.5}N_{0.5})_{0.6}$ were mixed manually with W, all at 99.5wt% purity, in proportion of 60wt% Ti(C,N) and 40wt% W. The second type of mixtures contained 55wt% Ti(C,N), 35wt% W and 10wt% Al. Aluminium stearate powder was also added as 3wt% proportion to the total mixture of powders, as a PCA. Milling media consisted of 1 kg of diameter 3mm 3Cr12 stainless steel. The ball-to-powder weight ratio was kept constant at 10:1 in all the experiments. Powders of Ti(C,N) were first milled for an hour to form external layers that prevent diffusion of steel constituents from the milling jar and balls to the powder particles.

Prior studies showed that kinetics of mechanical alloying was delayed and contamination was high when hard ball and milling pots such as WC or ZrC were used due to fracturing of the balls upon high energy impacts [4, 6]. Contamination by WC will introduce a non soluble phase in the binder phase, which will lead to high residual stresses after sintering as discussed in Chapter 2. Contaminant iron would be dissolved at sintering temperature (~1400˚C). The use of soft balls, such as 3Cr12 stainless steel, would therefore produce less detrimental effects on the composition of milled products.

The powders and balls were permanently stored and manipulated inside a glove box, under an argon or nitrogen atmosphere, inside which the oxygen was kept lower than 0.5vol.% under a total pressure of 1.3 bars. The pressure inside the glove box was set to be higher than ambient pressure, "positive pressure" to ensure that any leaks were outwards. The controlled atmosphere in the glove box also reduced the introduction of oxygen into the milling bowls where it would dissolve or adhere on the fresh surface of the finer powder particles generated during the high energy milling process. The powder mixtures were processed at a constant rotation speed of 400 min^{-1} for milling times of 12h, 24h, 48h and 72h.

The powder samples for SEM analysis were prepared by cold mounting in resin, grinding on successive grit papers and polishing with diamond pasts. Cross sections of the milled powder particles could hence be analysed.

The crystallite sizes (L) and lattice strains (e) of the milled constituents were analysed by X-ray diffraction in a Philips X'Pert powder diffractometer with an X' Celerator detector, and variable divergence and receiving slits with Ni filtered Co-Kα radiation. These parameters were calculated by means of the modified Williamson-Hall method presented in Section 2.5. The crystal structures were confirmed by electron diffraction analysis determined using a JEOL TEM 2100S. The compositions and distribution of the phases in the cross sections of the powder particles were analysed in backscattered electron mode under 12kV in an EDAX ESEM instrument equipped with an X-ray energy dispersive detector.

Oxygen and nitrogen contents in the milled powders were analysed in an ELTRA ON – 900 Oxygen / Nitrogen Determinator. The detectors utilize solid state sensors combined with infrared filters. Each of the cells could be installed with infrared absorption lengths ranging between 1mm and 320mm. The particle size distribution of the milled products was determined at various milling times using a Malvern Mastersizer 2000.

3.3.2. Transformation temperatures and annealing of the ball milled powders

The transformation temperatures of the milled powders were estimated by means of differential thermal analysis, DTA, in an argon atmosphere using a Mettler-Toledo TGA/SDTA851 heated up at a rate of 5˚C/min. The milled powders were subsequently annealed in an argon atmosphere for 2 hours near the transformation temperatures determined from the DTA curves. The phases formed in the annealed conditions were analysed by XRD. The crystal structures of the phases present in the annealed powders were also analysed the electron diffraction technique. Hence, the early stage mechanism of a pressureless sintering and the products formed in the binder systems in the absence of cBN were characterised.

3.3.3. High Pressure High Temperature PcBN sintering

Admixes containing 60% cBN and 40% of mechanical alloyed binders were prepared in an attrition mill in liquid hexane for 24h. The milling media consisted of WC balls. Attrition milling improved the dispersion and homogenization of the constituents. Aluminum powder was introduced in the attrition mill chamber, if it was not previously

added during the high energy ball milling stage. The slurries from the attrition milling were dried at 80˚C for 24h.

Sintering was conducted under a 5GPa pressure at 1500˚C for 30 minutes. The microstructure of the PcBN sinters was analyzed by means of SEM and TEM.

CHAPTER 4. RESULTS AND DISCUSSION - MECHANICAL ALLOYING

4.1. Ti($C_{0.5}N_{0.05}$) – W processed by high energy ball mill

The X-ray diffraction patterns of the products milled in a nitrogen atmosphere (Figure 4.1) showed that the initial mixture was composed of the crystalline Ti($C_{0.5}N_{0.05}$), phase (1), and W. The Ti($C_{0.5}N_{0.05}$) peaks shifted to higher 2θ angles after milling, which indicates a decrease of the d-spacings upon milling. The d-spacing for first order diffraction of X-ray could be calculated according to the Bragg's law as:

$$d = \frac{\lambda}{2.\sin\theta}.$$

Substituting λ by the wavelength for CoK_{α} = 0.178901nm and the third order diffraction angles yield the d-spacing value equal to 0.289701nm. The d-spacing after 24h processing is 0.282128nm. The variation of the d-spacing subsequent to the milling processing of Ti($C_{0.5}N_{0.05}$) represented 2.6% of the initial value.

The broadening of the peaks and their reduced intensities were attributed to the crystallite refinement, and the straining of crystallite lattices. The intensities of the characteristic X-ray diffraction peaks of tungsten decreased quickly on milling for 12h, and the peaks completely vanished after milling for 24h. The disappearance of the W peaks was attributed in the first instance to the amorphization of W and the solid state diffusion and dissolution of W atoms in the Ti($C_{0.5}N_{0.05}$) matrix.

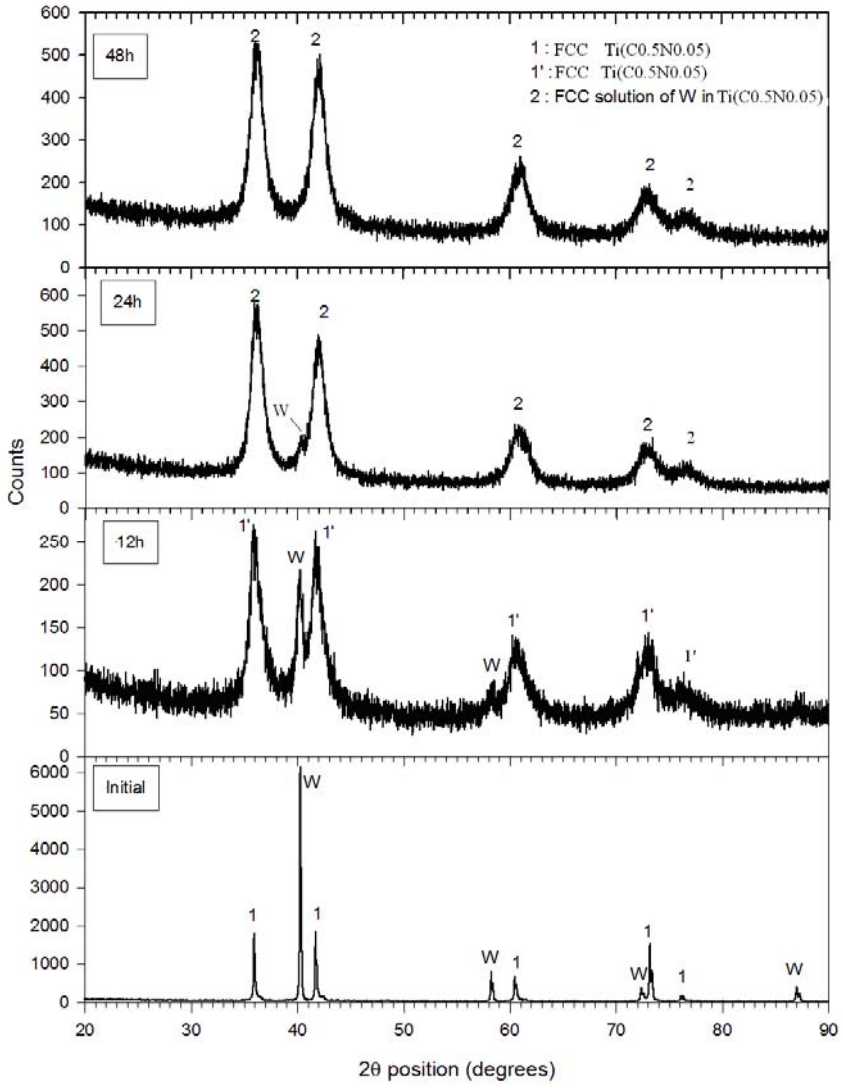

Figure 4.1. Effect of milling time on X-ray diffraction of the $Ti(C_{0.5}N_{0.05})$ – 40wt% W system processed in a high energy ball mill in a nitrogen atmosphere.

Similar trends were observed during the milling of the powder mixtures in an argon atmosphere. The evolution of the calculated crystallite sizes and the lattice strains of the $Ti(C_{0.5}N_{0.05})$ matrix milled in argon and nitrogen, and corrected using a silicon standard, are shown in Figure 4.2. The milling atmosphere affected the lattice strain, and hence the kinetics of the solid state dissolution between the powder constituents.

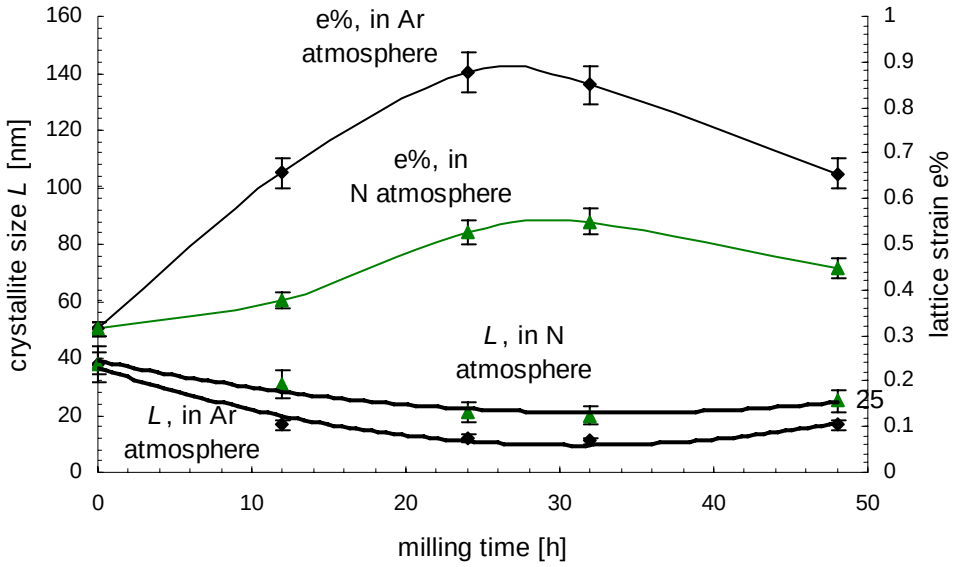

Figure 4.2: Evolution of crystallite sizes, *L*, and lattice strains, *e*, of $Ti(C_{0.5}N_{0.05})$ milled with W in argon or nitrogen atmospheres as a functions of milling time.

The lattice strains were higher after processing in argon, and the corresponding crystallite sizes were smaller than in nitrogen. This effect is explained by the dissolution of nitrogen in interstitial sites of the $Ti(C_{0.5}N_{0.05})$. Elemental nitrogen could be formed by the decomposition of the nitrogen molecules during milling, and the small radius, 0.075nm [201], allowed it to diffuse into interstitial sites of the sub-stoichiometric $Ti(C_{0.5}N_{0.05})$, which introduced tensile strains in the $Ti(C_{0.5}N_{0.05})$ lattices.

The tensile strains opposed the compressive strain induced by powders being trapped between impacting milling balls. Conversely, argon atoms have a larger diameter, 0.088nm [201], and could not fit so well into the interstitial positions in $Ti(C_{0.5}N_{0.05})$ lattice.

These crystallites would therefore not be subjected to volumetric tensile strain that could oppose the compressive strain induced in the milled materials. Thus, resultant lattice strains were higher in powders milled in argon atmosphere than in nitrogen.

The evolution of the nitrogen content shown in Figure 4.3, decreased after milling for 12h. However, an increase was observed at longer milling times when the powder mixtures were processed in nitrogen. Conversely, de-nitriding was observed in the powders processed in argon. Thus, the effect of the milling atmosphere on the lattice strain and on the crystallite size of the milled products was attributed to nitriding or de-nitriding when processed in nitrogen or argon atmospheres. The refinement of the crystallite sizes of the powders and the mechanism of storing/release of lattice strain energy during high energy ball milling could in return affect the kinetics of solid solution formation between the sub – stoichiometric Ti(C,N) and W.

A maximum lattice strain of 0.528% was attained after 24h milling in nitrogen, followed by a slight decrease after more milling. The crystallite size of the milled product increased from 21 to 25nm, due to the partial dissolution of W atoms in $Ti(C_{0.5}N_{0.05})$. The decrease in lattice strain after milling for more than 24h was attributed to the solid solution of W by substitution of Ti atoms in $Ti(C_{0.5}N_{0.05})$. Thus, the relief of the lattice strain of the matrix was partially attributed to the solid solution of W. The crystallite size of W milled in a nitrogen atmosphere decreased from 41nm to 21nm after 12h, and became smaller than that of $Ti(C_{0.5}N_{0.05})$.

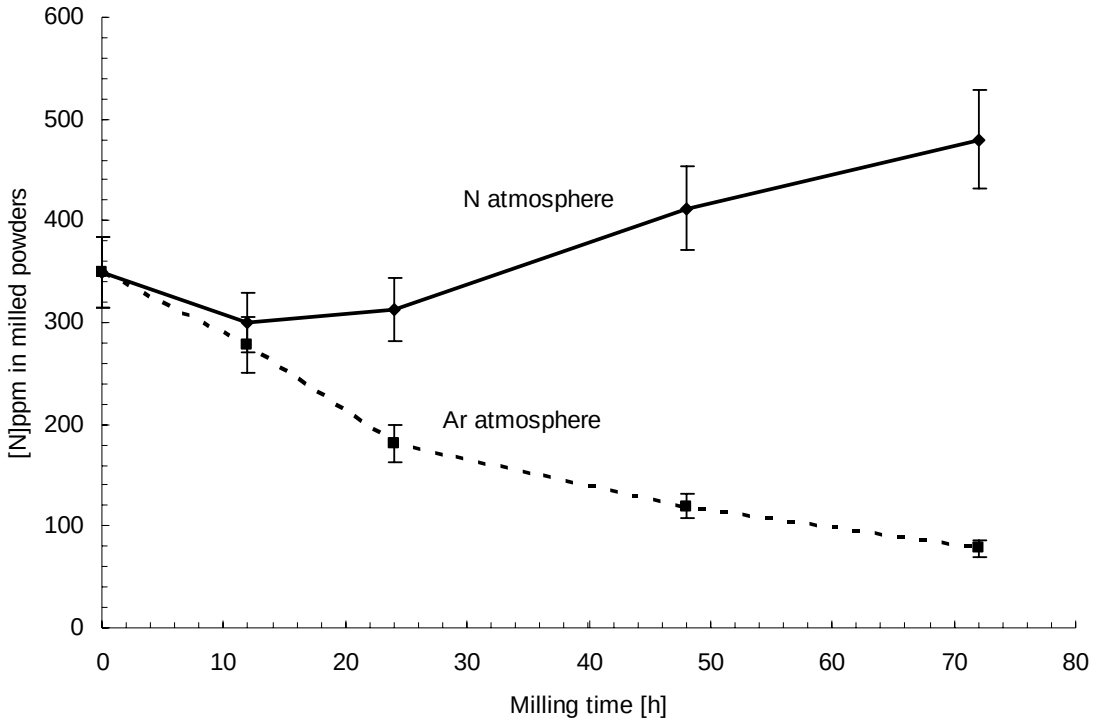

Figure 4.3. Nitrogen content of the $Ti(C_{0.5}N_{0.05})$-W powder mixtures processed by high energy ball milling in nitrogen and in argon atmospheres.

The calculated crystallite sizes and lattice strains in Figure 4.4 suggest that the crystallites of W became smaller than those of $Ti(C_{0.5}N_{0.05})$ at point (e,L) = (0.56%,17nm), after milling for 24h. Tungsten atoms were all dissolved in the strained $Ti(C_{0.5}N_{0.05})$ at that point. The high lattice strain energy induced the collapse of the W crystal structure, which led to the diffusion of W atoms into the solid $Ti(C_{0.5}N_{0.05})$ particles forming an FCC solid solution (2) on Figure 4.1 by substitution of Ti atoms. Figure 4.2 shows that the lattice strain induced in $Ti(C_{0.5}N_{0.05})$ crystals milled under an argon atmosphere was high, and its release contributed to the driving force for the dissolution of W atoms in the $Ti(C_{0.5}N_{0.05})$ matrix.

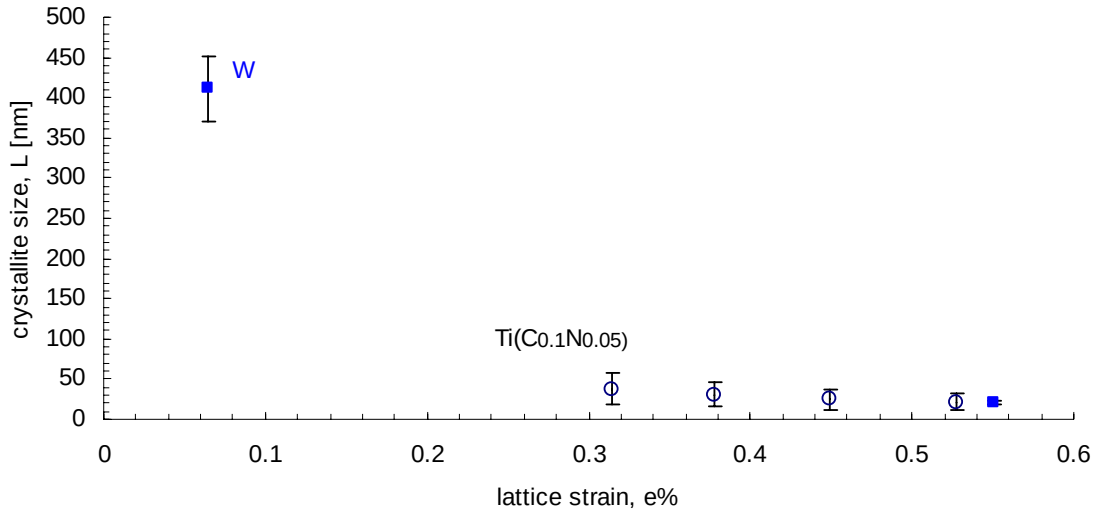

Figure 4.4. Variation of crystallite sizes, *L*, as function of lattice strain, *e*, of W and $Ti(C_{0.5}N_{0.05})$ upon milling in a nitrogen atmosphere.

The insertion of nitrogen atoms in the crystal lattice, and its antagonist effect on the compressive lattice strain energy storage could also explain similar observations on the variation of the crystallite sizes reported by Gordo *et al.* [79], and by Gómez *et al.* [80] in the manufacturing of Fe-50vol.% TiCN composite by ball milling under Ar and N_2-$9.9H_2$-$0.1CH_4$. These authors observed that milling under an argon atmosphere yielded finer and more homogeneous microstructures than in N_2-$9.9H_2$-$0.1CH_4$ or in air. The milling atmosphere was seen to be the most influential factor in the composition of the powders after milling [79, 80].

The particle size distribution of the mixtures of $Ti(C_{0.5}N_{0.05})$ and W powder mixtures milled in argon and in nitrogen atmospheres are presented on semi-logarithmic scales in Figure 4.5.

The starting $Ti(C_{0.5}N_{0.05})$ and W powder mixtures had bi-modal particle size distributions around 3.8 and 550μm, which corresponded to the distribution modes of the as-received W and the $Ti(C_{0.5}N_{0.05})$ powders. The particle size shifted to smaller values as milling proceeded, although the distribution remained bi-modal around the smaller values of 1.5 and 23μm. Thus, the size of larger particles of $Ti(C_{0.5}N_{0.05})$ powder was reduced by more than 20 times after 12h milling, whereas the particle size reduction ratio remained close to 2 for the finer W particles. Thus, *Stage 1* of the process was a fracturing of the larger $Ti(C_{0.5}N_{0.05})$ powder particles.

Phasha and Maweja [8] reported that it was difficult to mechanically alloy Ti and Mg elemental powders processed by the high energy ball milling route when the particle size of the softer magnesium powder was larger than that of the hard titanium powder by a critical ratio. The fine hard particles of Ti became trapped inside the large soft particles of magnesium powder during the initial stage of milling. This behavior resulted in a decreased transmission of mechanical energy to the powder particles. However, it was observed that a metastable solid solution was formed and extended solid solution was achieved when the particle sizes of Ti and Mg powders were fine and similar.

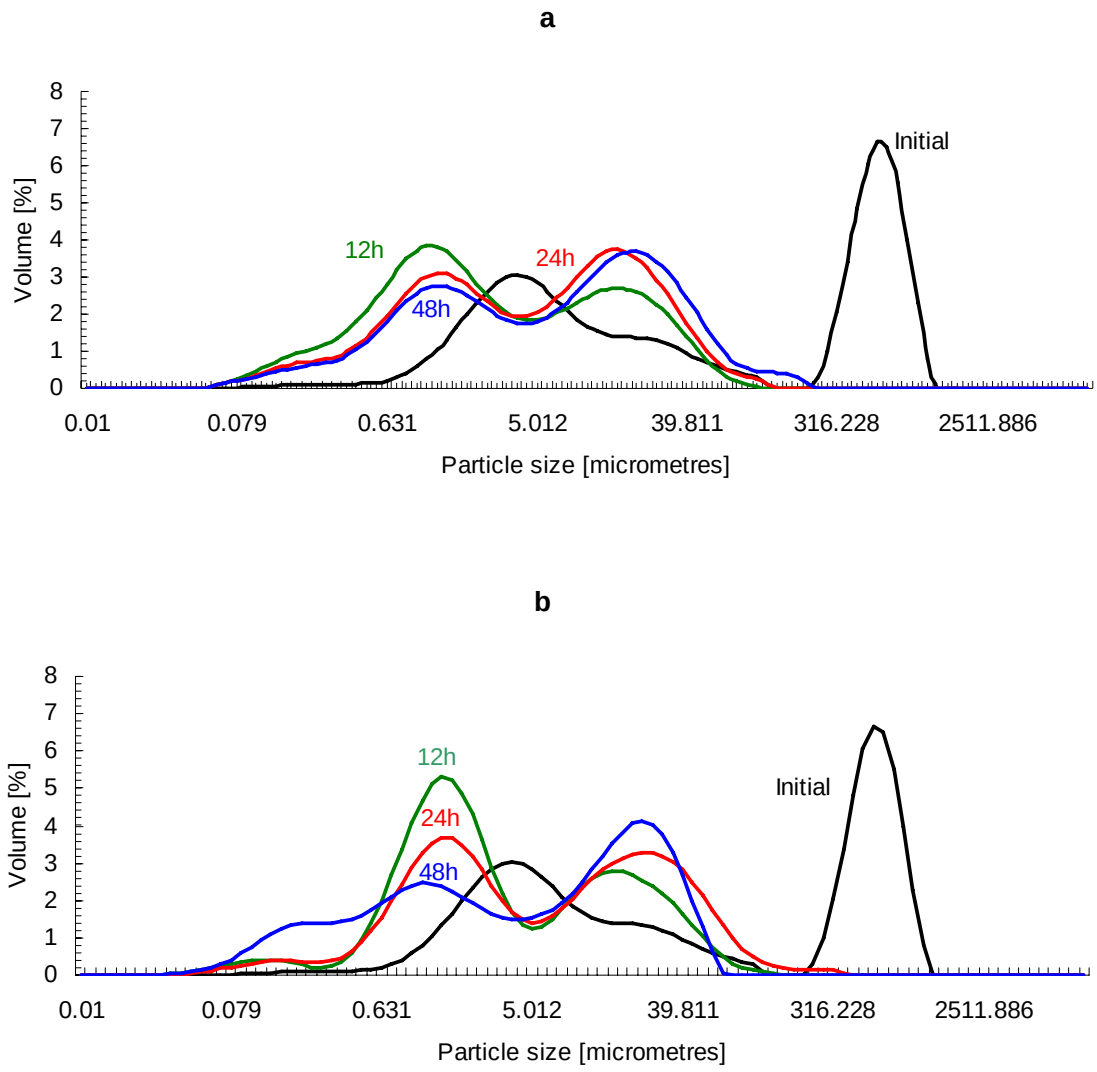

Figure 4.5. Particle size distribution of $Ti(C_{0.5}N_{0.05})$ and W powder mixtures processed by high energy ball mill (a) in an argon and (b) in nitrogen atmospheres.

It is shown by Figure 4.5 that the proportion of the fine particles around 1.5μm was higher in the products milled for 12h than in those milled for longer times. The systematic decrease in the proportion of these finer particles and the simultaneous increase in proportion of those particle sizes around 23μm suggest that fracturing of powder particles only dominated during the first 12h, whereas the cold welding and

agglomeration predominated as the milling time increased to 24h and longer. This suggested that the efficacy of the PCA decreased when the milling time exceeded 24h. To avoid significant decrease of the yield of the process, another 3% mass of process control agent was added to the powders after milling for 24h and before further processing. It is believed that an inert liquid instead of the solid aluminum stearate would be more efficient as PCA when ball milling is conducted for times longer than 24h.

The d_{10}, d_{50} and d_{90} characteristics that represent the sizes of 10, 50 and 90% of the total volume of particles in the powders were compared to elucidate the effect of the milling atmosphere on the particle size. The three characteristics are shown in Figure 4.6. It is observed that the d_{10}, d_{50} and d_{90} were similar and independent of the milling atmosphere. Thus, it reasoned that the milling atmosphere did not affect the particle sizes. This fact needs to be emphasized as the milling atmosphere rather had a significant effect on the crystallite sizes and on the crystallite lattice strains of the milled products, as observed previously and shown in Figure 4.2. The size reduction of the powder particles occurred by a mechanism of fracturing along favorable planes or surfaces and is dependent on the bulk and mechanical properties such as hardness, tensile and shear strengths [1-7]. The effects of the milling atmosphere on the process are of different types.
Viscosity and density decrease the transmission of the energy from the milling balls to the powder particles, whereas adsorption and reactivity can improve the fracturing mechanism by disintegrating the grain boundaries of the particles. The quasi-absence of the effect of the milling atmosphere on the particle size was therefore attributed to the low density and viscosity and the inertness of the argon and nitrogen atmospheres.

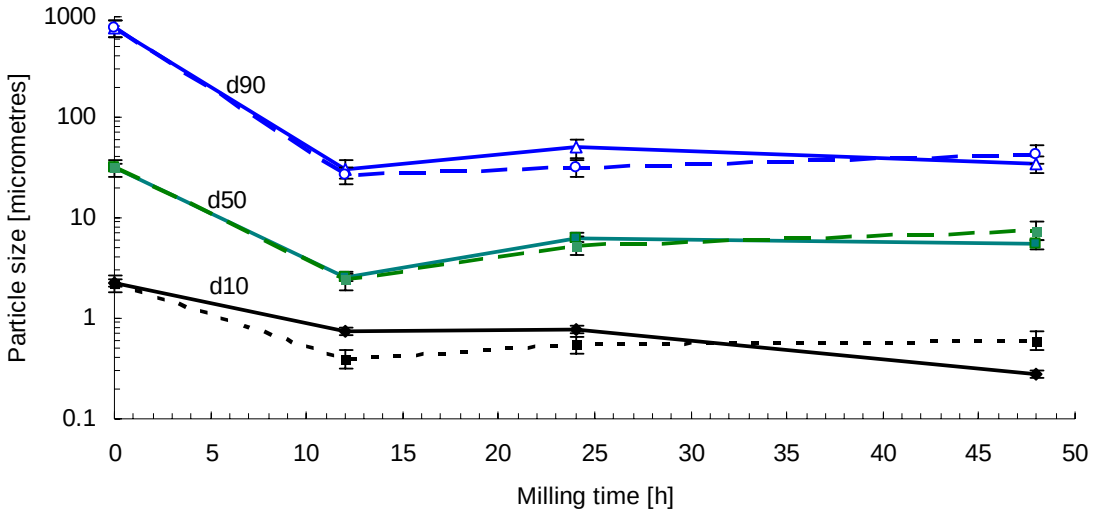

Figure 4.6. Particle size distributions of $Ti(C_{0.5}N_{0.05})$-W powder mixtures processed in argon (doted lines), and in nitrogen (solid lines).

The TEM micrographs in Figure 4.7 show the presence of sub-micron particles in the powders obtained after milling. The asymmetric large diffraction spots are indicative of the formation of elongated large crystals formed by agglomeration and deformation of many small randomly orientated crystals. The elongated spots in the electron diffraction patterns of the milled products also indicated an intermediate product with a deformed FCC crystal structure formed after milling for 12h (Figure 4.7).

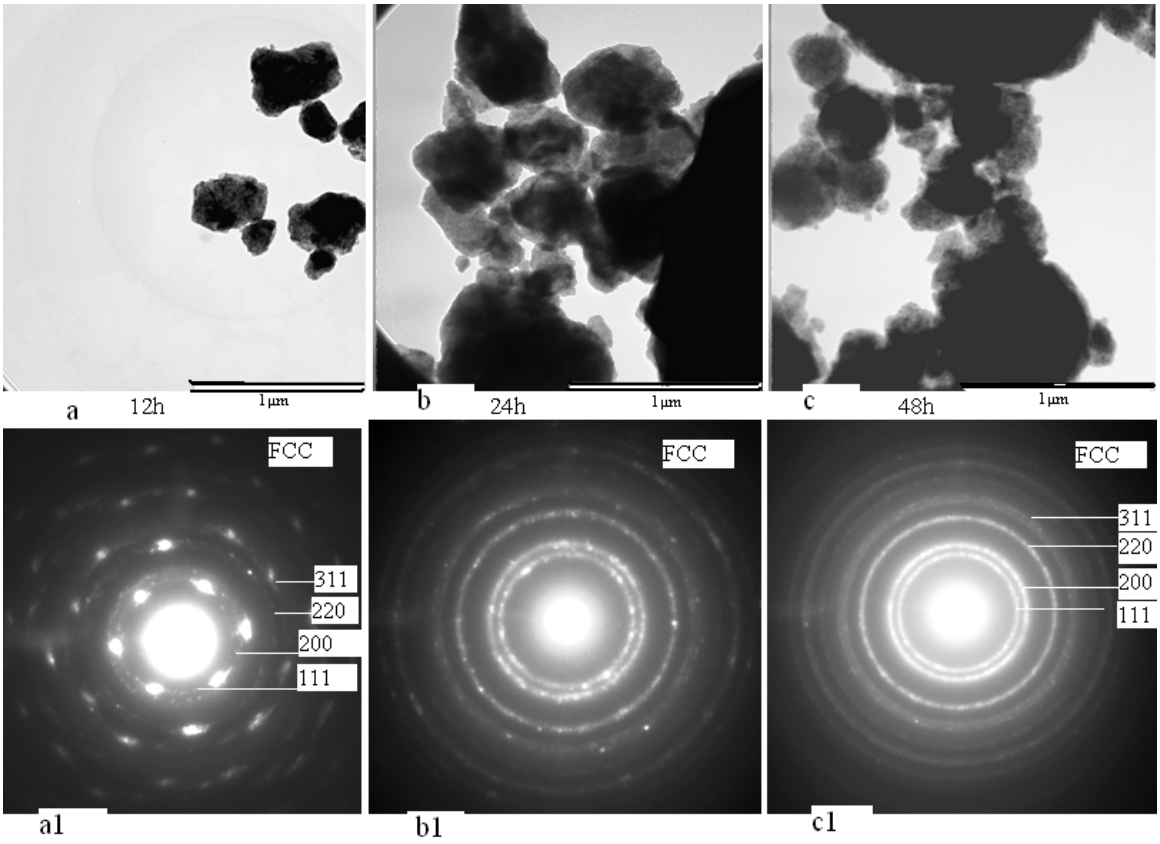

Figure 4.7. TEM micrographs of Ti($C_{0.5}N_{0.05}$) -W milled products formed after a) 12h, b) 24, c) 48h and the corresponding selected area electron diffraction patterns a1, b1 and c1.

The characteristic XRD peaks, in Figure 4.1, suggested that the intermediate phase (*1'*), formed after 12h, mainly resulted from the straining of the Ti($C_{0.5}N_{0.05}$) crystal lattice. Thus, both the TEM and XRD results show that *Stage 2* of the process consisted of deformation of the crystal lattice of the matrix constituent.

The crystal structure of Ti($C_{0.5}N_{0.05}$) was deformed, whereas W crystallites were destroyed. The elongated spots in the corresponding selected area diffraction patterns (SADP) indicate the existence of well defined atom planes which diffracted the electrons. The SADP of the products milled for 24h (Figure 4.7.b and 4.7.b1) were composed of rings containing some spots.

This indicated that the crystallites of the products became finer as the milling time increased to 24h, and W atoms were dissolved in the strained crystallites of Ti($C_{0.5}N_{0.05}$), resulting in finer randomly orientated crystallites.

The thickening and the decrease in intensity of the rings in the SADP of the powders milled for 48h (Figure 4.7.c2) is indicative of further refinement of the crystallites. Thus, *Stage 3* consisted of dissolution of W in the metastable FCC phase (1′) that led to the formation of the metastable FCC solid solution phase (2). The powder products obtained after milling for 48h or longer could also contain an amorphous substance in an FCC matrix.

In samples milled for shorter times, more grains with higher dislocation densities were observed (Figure 4.8) than for similar samples milled for longer times (e.g. 48h). This absence was observed once the tungsten had become dissolved in the Ti($C_{0.5}N_{0.05}$) lattice, and was deduced to be due to the release of the lattice strain energy, since the dislocations had mainly disappeared. Similar observation in Ti-rich particles milled for shorter times were reported before solid state dissolution of Mg during high energy ball milling of Mg-Ti alloys [7].

Backscattered SEM images of the cross sections of the particles showed that the powder mixtures were initially heterogeneous, as shown in Figure 4.9a. Finer powder particles of tungsten formed large agglomerates that were not destroyed during the manual mixing prior to ball milling.

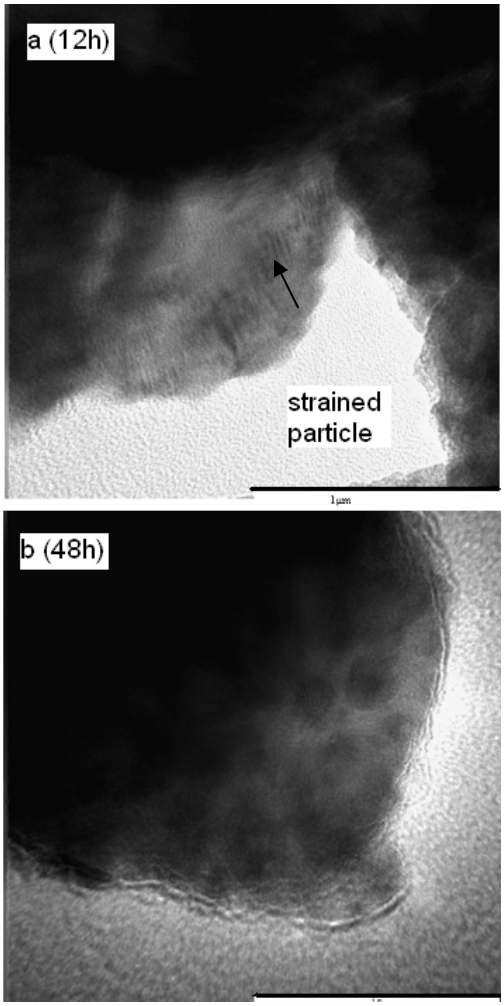

Figure 4.8. TEM micrograph showing (a) a strained particle of Ti($C_{0.5}N_{0.05}$) powder particle milled for 12h and (b) a particle of powder milled for 48h. Scale bar = 1 μm.

Powders milled for 12h contained mixed agglomerates of different shapes and sizes <1μm - 1000μm, illustrating the well known fracture - cold welding mechanism. Milling started to improve the mixing and the homogeneity of the powders (Figure 4.9.b) by destroying the agglomerates of tungsten particles, and the fine particles became dispersed in the softer Ti($C_{0.5}N_{0.05}$) particles. The softer of the powder particles present plays this role during high energy ball milling [1-8, 72, 73, 78].

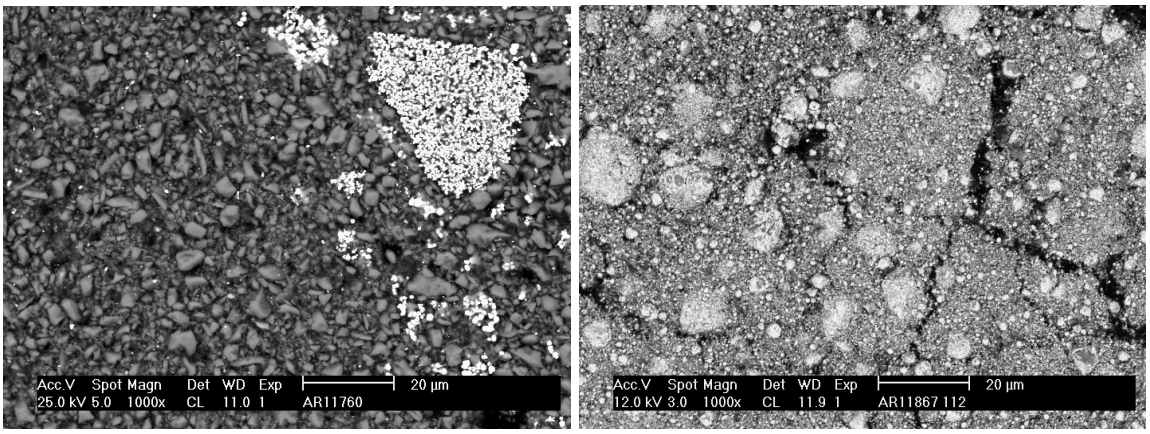

(a) (b)

Figure 4.9. Backscattered SEM images of: (a) the starting powder and (b) the powder milled for 12h in nitrogen atmosphere showing the improved homogeneity of the $Ti(C_{0.5}N_{0.05})$ - W mixture.

The fracturing - cold welding mechanism is deduced to enhance the solid state homogenisation and surface diffusion by forming new fresh surfaces with a high defect density on the powder particles, and by bringing them into contact under high pressure conditions generated between the impacting balls, as reported in other works [1-6].

Cross sections of the milled powder particles (Figure 4.10) show that mechanical alloying occurred via the diffusion of W atoms inside the $Ti(C_{0.5}N_{0.05})$ particles, and reveal a core-rim structure. This diffusion was completed after 24h milling for $Ti(C_{0.5}N_{0.05})$ particles that were smaller than 1µm. Conversely, $Ti(C_{0.5}N_{0.05})$ particles larger than 1µm still had a core-rim structure, with a rim being richer in tungsten.

The EDX and the electron probe microanalysis showed that the core of the large powder particles contained more or less 77±3wt% Ti with less than 22±2wt% W, whereas the rim contained 53±2wt% Ti with 42±2wt% W and about 5±2wt% Fe. However, these values are very speculative because of the large interaction volumes (possibly spreading to 3µm

across) compared with the fine particle sizes. That there was more W in the rim was confirmed by the lighter contrast in the BSE mode. Iron was also found in the rim cross section, with a small peak at ~6.5 keV in the EDX spectrum.

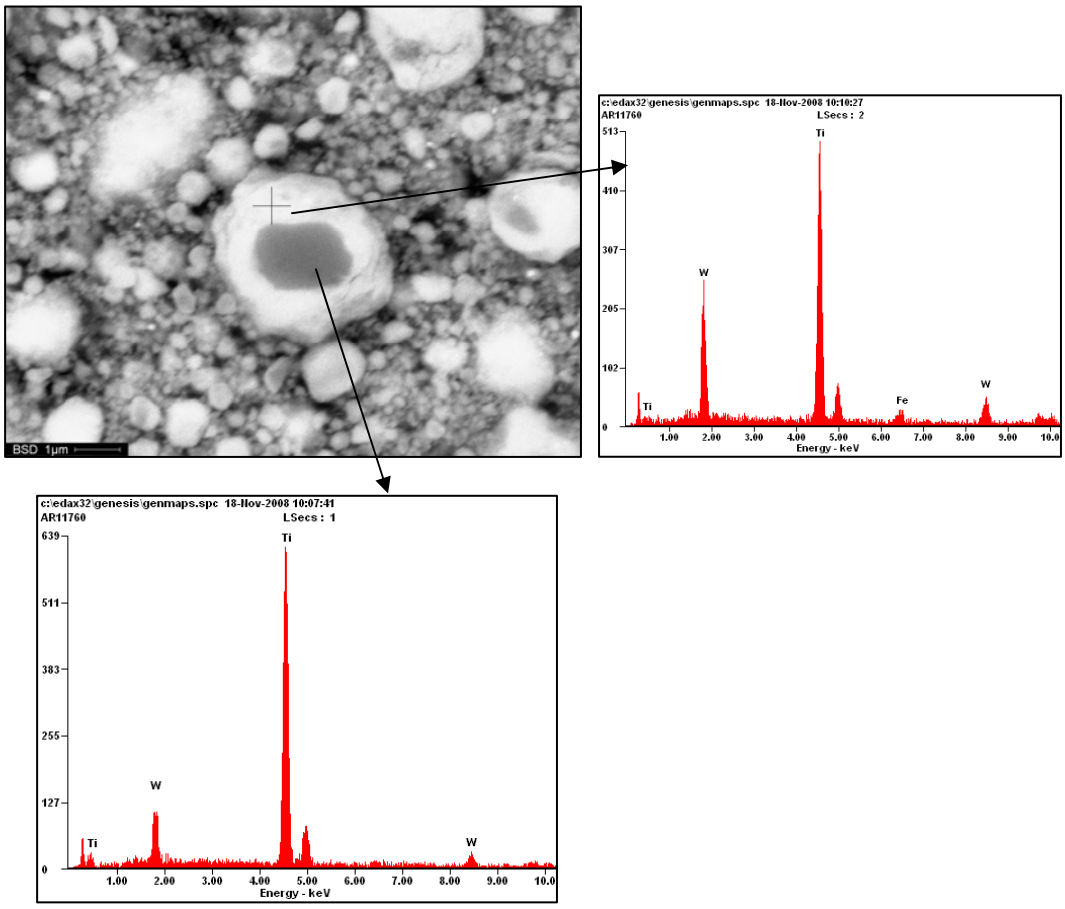

Figure 4.10. Backscattered SEM image and EDX spectra of cross sections of $TiC_{0.9}N_{0.1}$ - W mixed powder milled for 24h at 400 min^{-1} in a nitrogen atmosphere using stainless steel balls.

The absence of Fe in the core of the powder particles milled for 24h indicates that the powder particles were contaminated from their surface by stainless steel ball constituents. Iron was well distributed in the rims of the milled particles, as was tungsten.

There was no detectable presence of steel particles that could come from broken balls. Hence, the Fe-contamination occurred through diffusion from the milling balls.

The cross sections of particles obtained after 48h ball milling consisted of one homogeneous phase as shown in Figure 4.11. The iron content in the final product particles was 3 - 4wt% and was presumed to be limited once the ball surfaces were covered with the charge. Iron contamination up to 4wt% did not have adverse effects on the process of dissolution of W in the strained phase (1´) of $Ti(C_{0.5}N_{0.05})$.

The concentration gradients of both W and Fe across the sections of the milled particles suggest that surface diffusion of atoms into the particles of the strained FCC phase (1') on Figure 4.1 was the mechanism of solid solution taking place at shorter milling times. The chemical concentration gradient and the release of the lattice strain energy contributed to the total driving force for the solid state diffusion of W atoms throughout the core of the host particles.

The driving force for the MA process will therefore include a chemical term (ΔG_V) due to the concentration gradient through the cross section of the particles, the lattice strain energy (ΔG_e) [107] stored in the FCC phase (1') of $Ti(C_{0.5}N_{0.05})$, and the retarding force required for the formation of new fresh surfaces during the fracturing of particles [6, 76, 78].

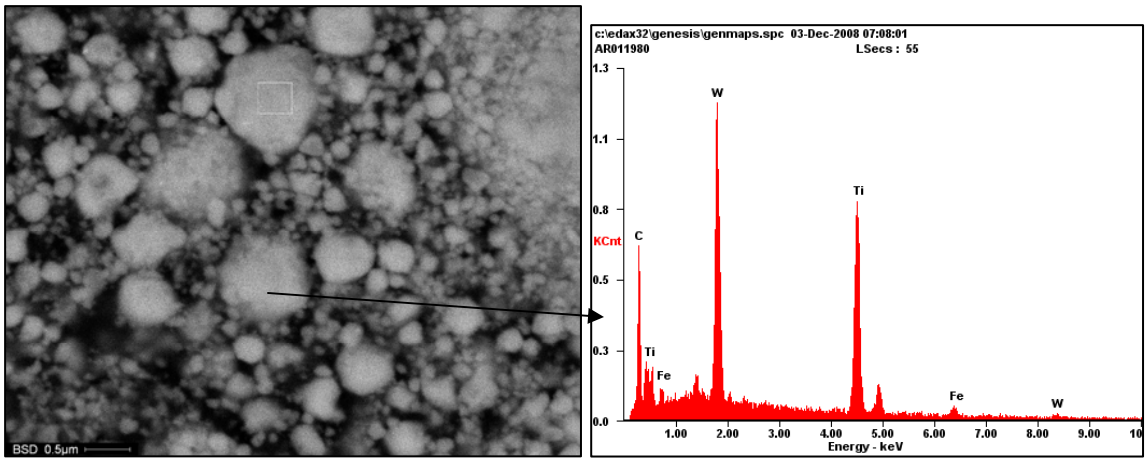

Figure 4.11. Backscattered SEM image and EDX spectrum of cross sections of the $Ti(C_{0.5}N_{0.05})$ particles milled for 48h at 400 min^{-1} in a nitrogen atmosphere using stainless steel balls, showing homogeneous phase formed and sub-micron particles.

Surface adhesion of W atoms onto the Ti(C,N) particles and the dislocation density near the surface of these particles would also determine the surface diffusion in the initial stage of MA. The driving force total for formation of MA during ball milling could hence be obtained as follows:

$$\Delta G = \Gamma.A + \Delta G_V.V + \Delta G_e.V - \gamma_A.A \qquad (4.1)$$

where Γ is the specific surface energy, γ_A is the required energy for formation of new surfaces. Assuming spherical particles of equal volume gives the surface area $A = \pi L^2$ and the volume $V = \frac{1}{6}\pi L^3$, where L is the particle size. Substituting these expressions in Equation (4.1) gives:

$$\Delta G = V\left(\frac{6}{L}(\Gamma - \gamma_A) + \Delta G_V + \Delta G_e\right) \qquad (4.2)$$

The increase of the lattice strain of the deformed phase (1') in Figure 4.1 of $Ti(C_{0.5}N_{0.05})$ after milling for 12 to 24h, and the subsequent decrease observed after milling for 48h

suggest that the relief of the lattice strain energy contributed to the driving force for surface diffusion of W atoms at the beginning of the alloying process. Both the surface diffusion and the diffusion under the concentration gradient inside the particles of $Ti(C_{0.5}N_{0.05})$ have been therefore enhanced by the high pressure and high dislocation densities generated in the particles.

Hence the energy of formation of dislocations near the surface of the particles and the potential for diffusion due to the concentration gradient can be expressed as function of the variation in crystal lattice strain as follows:

$$\Delta G_V + \Delta G_e = \tau.\Delta e \tag{4.3}$$

where τ is the bulk modulus of the particles and Δe is the strain. Substituting 4.3 into 4.2 gives:

$$\Delta G = V\left(\frac{6}{L}\left(\Gamma - \gamma_A\right) + \tau.\Delta e\right) \tag{4.4}$$

Equation (4.4) predicts the possibility of occurrence of a dynamic equilibrium when

$$\frac{6}{L}\left(\Gamma - \gamma_A\right) + \tau.\Delta e = 0 \tag{4.5}$$

The equilibrium is reached when the crystallite size of the solvent phase is refined to a critical limit obtained as follows:

$$L_{critic} = \frac{6\left(\gamma_A - \Gamma\right)}{\tau.\Delta e} \tag{4.6}$$

L_{critic} is the intrinsic crystallite size at which the matrix phase cannot dissolve atoms of other mixture constituents to form solid solutions by mechanical alloying.

It infers from Equation (4.6) that materials which present the bigger variation in lattice strain, Δe, will have the smallest L_{critic} size.

The implications of this analysis may be multiple. Mechanical alloying by high energy ball milling is well known as a capable route for alloying of metal systems which present positive Gibbs' free energies, and that are not obtainable by conventional investment casting processes. However, it is always uncertain which of the ball milling processing parameters or the materials properties determine the mixture constituent that acts as solvent or solute. Different reported roles played by the constituents of Ti-Mg systems for electrochemical hydrogen storage [164-172] and in ceramic – metal composite materials processed by MA [173-177] illustrate the necessity of an understanding of the factors that determine the role of the constituents in MA.

According to Equation 4.6 that the mixture constituent that readily releases the largest amount of lattice strain energy, $\tau.\Delta e$, or required less energy to form new fresh surfaces, $\gamma_{A,}$ will have the smallest L_{critic}, thus readily dissolve the other constituents upon high energy ball milling. The analysis also shows there is a critical starting particle size of the solid solvent, below which it is impossible to strain the crystallites or to produce the necessary dislocations for solid state diffusion of the solute atoms.

A physical analogy can be established between Equations 2.4, proposed by Nieh and Wadsworth [106] and 4.6 as the two conclusions on the existence and definition of a critical particle size for MA.

The two models include the concept of surface energy-to-strain energy ratio. The thermodynamic analysis of Aguilar *et al.* [107] on the extended solubility of systems processed by MA suggested that the surface energy had a larger influence compared with the elastic strain energy due to the presence of dislocations. It is therefore suggested that the two equations may be interchangeable, depending on the experimental accessible measurements.

4.2. Ball mill processing of 60wt% $Ti(C_{0.5}N_{0.5})_{0.6}$-40wt% W mixtures

The evolution of the crystal structure, microstructure and alloying was investigated by the same means as previously for the $Ti(C_{0.5}N_{0.05})$-W system. Once again, the XRD peaks of tungsten decreased with milling time, only a small peak being observable after 48h (Figure 4.12), whereas this was not seen in the first system (Figure 4.1). On the other hand, the corresponding peaks had vanished after 24h ball milling of the first system composed of $Ti(C_{0.5}N_{0.05})$ - 40 wt% W, represented in Figure 4.1.
Thus, XRD shows that the dissolution kinetics of W atoms in $Ti(C_{0.5}N_{0.5})_{0.6}$ was slower than in $Ti(C_{0.5}N_{0.05})$. An FCC product encompassing W (6) was formed after 48h milling.

The 2θ angles of the XRD peaks of $Ti(C_{0.5}N_{0.5})_{0.6}$ were 0.5 to 1.5˚ larger than those of $Ti(C_{0.5}N_{0.05})$. Therefore the d-spacings of $Ti(C_{0.5}N_{0.5})_{0.6}$ are 2.3 to 2.4% smaller than those of $Ti(C_{0.5}N_{0.05})$. The slower dissolution rate of W atoms could be attributed to this difference, with $Ti(C_{0.5}N_{0.5})_{0.6}$ having smaller d-spacing. Thus, the solid state diffusion of W atoms in $Ti(C_{0.5}N_{0.5})_{0.6}$ lattices would necessitate more energy to be activated.

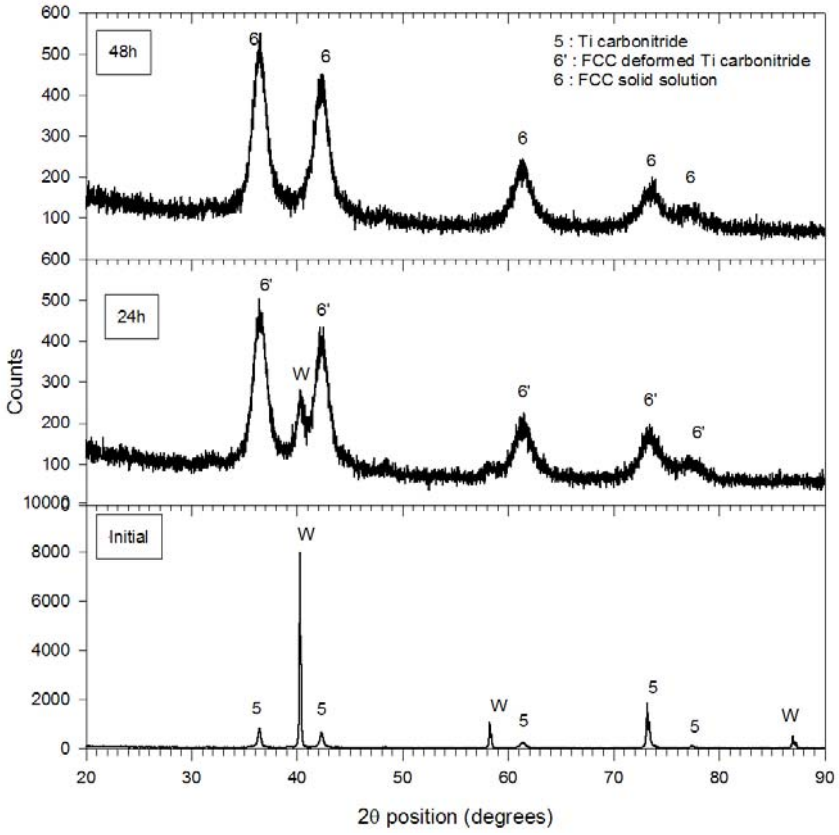

Figure 4.12. Effect of milling time on X-ray diffraction of the $Ti(C_{0.5}.N_{0.05})$ - 40 wt% W system processed in a high energy ball mill in an argon atmosphere.

A different approach to the understanding of the difference in the kinetics of dissolution of W atoms in the two titanium carbonitrides is suggested in terms of strain energy. The $Ti(C_{0.5}N_{0.5})_{0.6}$ peaks had broadened and shifted toward the lower 2θ positions as milling time increased. Similar behaviour was observed during ball milling of the $Ti(C_{0.5}N_{0.05})$ – W mixtures in an argon and in a nitrogen atmosphere. A single phase product (6), in Figure 4.12, was formed after 48h milling. The phase (6) had identical XRD peaks as the FCC phase (1), in Figure 4.1. The chemistries of the two FCC phases (1) and (6) determined by EDX and EPMA revealed a solubility of W in the two Ti(C,N) in atoms ratios ranging between 10Ti:1W to 5Ti:1W as the milling time increased from

12 to 48h. The dissolution of W in the $Ti(C_{0.5}N_{0.5})_{0.6}$ particles was nearly completed after 48h milling.

The W content was near to 2Ti:1W in the finer particles obtained after 12h processing. The atom ratio changed to 5Ti:1W for longer milling times, indicating that alloying first occurred between the finer particles of the two constituents of the powder mixtures. These fine pre-alloyed particles were later dissolved in the larger Ti(C,N), while the fracturing of the coarse particles continued.

The particle size distribution of the $Ti(C_{0.5}N_{0.5})_{0.6}$ - 40 wt% W mixtures processed by argon was bimodal (Figure 4.13), which did not change significantly for the milling times of 24h or longer, as was observed for the $Ti(C_{0.5}N_{0.05})$ - W mixtures. It was observed in Figure 4.10 that the larger particles had a core-rim structure with higher W content in the rim than in the core. The cross sections of the smaller particles were homogeneous for the same milling time.

The small particles with homogeneous composition were generated by fracturing the alloyed rims of the large particles. This process had two effects:

- the generation of new finer particles of the alloy
- and the refinement of Ti(C,N) particles and formation of fresh surfaces.

Thus, the resulting particle size distribution was bimodal for the alloying process. However, it was observed that the two mode values of the distribution were closer in

milled powders than in the initial mixtures. Thus, a single mode distribution might be expected in milling times longer than those used in the current experiments.

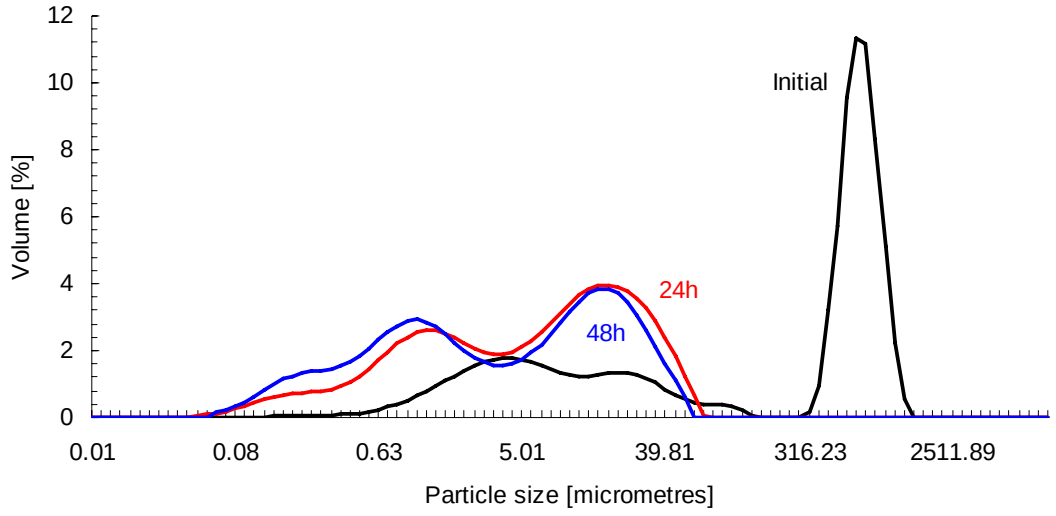

Figure 4.13. Particle size distribution of $Ti(C_{0.5}N_{0.5})_{0.6}$ - 40wt% W powder mixtures processed by high energy ball mill in argon.

The initial particle size of the $Ti(C_{0.5}N_{0.5})_{0.6}$ - W mixture was 20 to 30% coarser than that of the starting $Ti(C_{0.5}N_{0.05})$ - W mixtures. However, the d_{10} = 0.31µm, d_{50} = 4.0µm and d_{90} = 27.6µm of the final product processed in argon were about half the corresponding values achieved for the $Ti(C_{0.5}N_{0.05})$ - W under the same conditions. This indicated that fracturing the particles of $Ti(C_{0.5}N_{0.5})_{0.6}$ required less energy than $Ti(C_{0.5}N_{0.05})$. However, the finer particle size achieved did not enhance the kinetics of dissolution of W in $Ti(C_{0.5}N_{0.5})_{0.6}$ compared to $Ti(C_{0.5}N_{0.05})$. Thus, the formation of new fresh surfaces by fracturing and refinement of the powder particles could only be considered as one factor, not necessarily determinant, among many others, which contributed to the mechanical alloying by high energy ball milling.

The variation of the crystallite sizes and the lattice strains of $Ti(C_{0.5}N_{0.5})_{0.6}$, the product of deformation and the solid solution phase formed as milling proceeded, are illustrated in Figure 4.14.

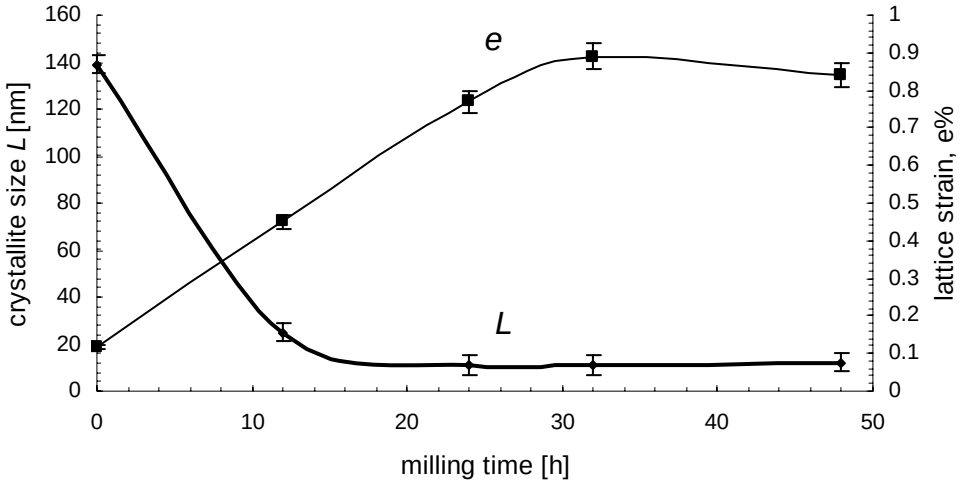

Figure 4.14. Evolution of crystallite size and lattice strain of $Ti(C_{0.5}N_{0.5})_{0.6}$ - W mixtures processed by high energy ball milling in an argon atmosphere.

The crystallite size of $Ti(C_{0.5}N_{0.5})_{0.6}$ decreased from ~140 nm to ~11 nm after 24 h milling, which was faster than for $Ti(C_{0.5}N_{0.05})$. Again, the crystallite size increased slightly, to about 17nm, after milling for 48h. The lattice strains developed were double those observed in $Ti(C_{0.5}N_{0.05})$. However, the relaxation of the lattice strain, observed after 24h milling of the $Ti(C_{0.5}N_{0.05})$ occurred later, after 48h milling of the $Ti(C_{0.5}N_{0.5})_{0.6}$, and the corresponding strain relief was smaller.

Comparing the two systems indicates that neither the high lattice strains developed on milling, nor the smaller crystallite sizes achieved were determinant for mechanical

alloying. Conversely, the comparison between the parameters calculated based on the XRD results and the TEM microstructures showed that the relaxation of the lattice strain in the matrix coincided with the onset for alloying between W and the Ti(C,N). Thus, the release of the lattice strain energy stored in the deformed matrix appears to be a major contributor to the driving force for mechanical alloying between elemental or compound powders.

4.3. Contamination by oxygen

Contamination from diverse origins and oxygen sensitivity due to increased specific surface are the main drawbacks of the MA processing [1-6]. These factors increase the reactivity with the ambient oxygen and the risk of catching fire or explosion. Oxygen can also be dissolved in the powder particles during high energy ball milling. The dissolved oxygen can later react with the powder constituents during heat treatment or forming at elevated temperature, e.g., during hot pressing or sintering. The oxide particles formed can contribute to some improved mechanical properties of the sinters, but only when their volume fraction can be controlled and kept below limits that are low in general. Beyond these limits, the sintered products become brittle and consequently unusable. The milling atmosphere is set, in principle, to minimize the oxygen uptake by the powder inside the milling bowl.

The evolution of the oxygen contents of the $Ti(C_{0.5}N_{0.05}) - W$ and $Ti(C_{0.5}N_{0.5})_{0.6} - W$ powders processed in argon and in nitrogen atmospheres were analyzed as the milling time increased (Figure 4.15).

The oxygen content reached the maximum at the intermediate times of 12 to 24h, and decreased for longer times. The decrease in oxygen content was in part attributed to the cold welding and agglomeration of the fine particles of powders that were processed for times longer than 24h.

The particle size distribution analysis showed that there were more fine particles in powders milled for 12h than in those milled for longer times. However, there is another plausible explanation to the decrease in oxygen sensitivity of the powders that were milled for longer than 24h. The XRD analysis showed that the dissolution of W atoms in the Ti(C,N) was effective in powders milled for longer times. The material milled for 12 to 24h rather consisted of deformed metastable FCC phases (1') and (6') of the two carbonitrides. These strained materials were activated and highly reactive in the presence of oxygen. This agrees with experience that these materials readily burnt by simple contact with air, or when slightly impacted between a sample holder and a spatula.

The strain energy stored in these particles contributed to the oxidation enthalpy. The powder mixtures processed for 48h were less prompt to oxidise and burn because of the lower level of strain energy remaining after part of it was released upon dissolution and alloying of W atoms in the Ti(C,N) lattices. The strain energy and the fine particle size contributed to the chemical reactivity in the presence of oxygen of the powders milled for 12h to 24h. The high oxygen contents in the powders milled for 12 to 24h resulted from the oxidation during sample collection from the milling bowl and transportation to the oxygen analyzer equipment. Samples of powders milled for short time, i.e. collected

before alloying occurred, should therefore be collected inside a glove box in an inert atmosphere. Powders milled for 48h were more stable in presence of oxygen. Their oxygen contents remained below 4% after 6 months storage in open air.

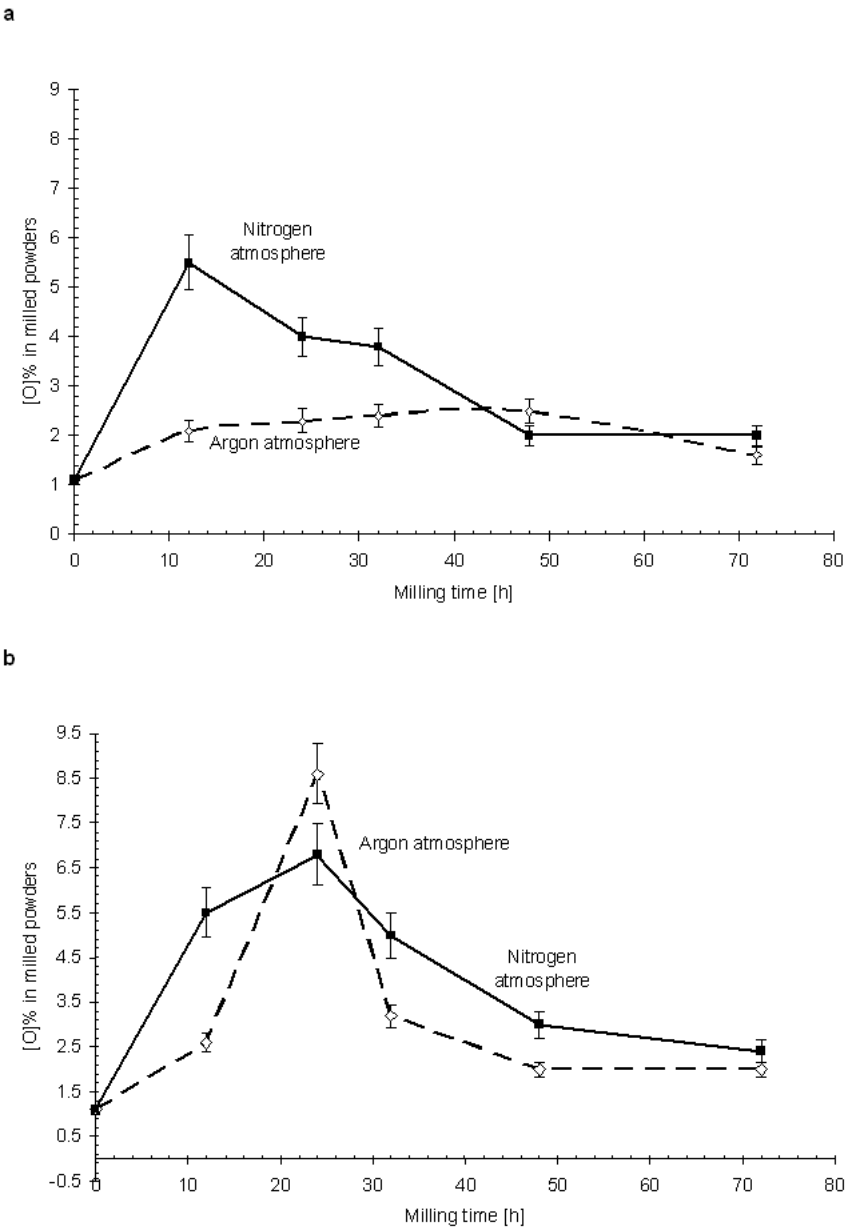

Figure 4.15. Oxygen contents in (a) $Ti(C_{0.5}N_{0.05})$ - W and (b) $Ti(C_{0.5}N_{0.5})_{0.6}$ - W powders milled in argon and nitrogen atmospheres.

It was observed in Section 4.1, Figure 4.3 that the nitrogen content of the powder mixtures milled in an argon atmosphere decreased as the milling time increased. A common cause to the simultaneous decrease of nitrogen and oxygen contents in the powders milled for 48h is the alloying process. Tungsten has a slightly smaller covalent radius than titanium [201]. The solid solution by substitution of W to the Ti atoms therefore led to a slight shrinkage of the FCC crystal lattices and the volume of interstitial sites of the Ti(C,N) matrix. The access of nitrogen or oxygen atoms to the interstitial volumes was hence restricted, which led to the simultaneous decrease of nitrogen and oxygen contents in the powders milled for longer times.

It is likely that the amorphisation of the FCC solid solution formed by excessive milling would increase the sensitivity of the powders to oxygen. The oxygen contents of the MA powders may increase again. Thus, it is suggested that an optimum processing time for MA exists for reduced oxygen uptake and for minimal sensitivity to ambient oxygen when the host matrix is alloyed with an element of smaller covalent radius.

Short milling times which generate an activated status in the material and longer milling times that may lead to the amorphisation should be avoided if the sensitivity to oxygen or the auto-combustion of the products were practical issues for a particular powder system processed by high energy ball milling.

4.4. Effect of Al addition on the mechanical alloying process

Binders for PcBN sintering may contain Al that is added into Ti(C,N) powder. The mixture of powders is processed by attrition milling for five hours in liquid hexane to refine the particle size and to homogenise the mixture before sintering. The homogeneous distribution of powders particles of boron nitride with the binder would enhance the formation of homogeneous microstructures in the sintered product, which is required for a better distribution of properties and performance of the PcBN cutting tools [10].

Attrition milling does not induce mechanical alloying of the constituents. Its action is limited to grain size refinement and homogenisation. The milled powders are then reacted at high temperature between 1050˚C and 1400˚C to dissolve Al in the binder phase, before HPHT sintering of the PcBN [10]. The brittle intermetallic binary phases TiB_2 and TiAl are formed during HPHT sintering of PcBN when the described mixing method is used.

The mechanical alloying of 55wt% Ti(C,N) - 35wt% W - 10wt% Al in a single stage was therefore investigated in this study as a means of formation of homogeneous ternary binder phases without a the pre-reaction stage of Al with the other binder constituents. Thus, experiments were conducted where sub-stoichiometric Ti(C,N), W and Al powders were processed by high energy ball milling in an argon atmosphere instead of the conventional Ti(C,N) - Al mixing by attrition milling in liquid hexane and pre – reaction at 1050˚C prior to sintering.

The BSE - SEM microstructure of the cross sections of the particles showed that the starting powder mixture (Figure 4.16) contained fine equiaxed particles of W (~2μm) and relatively large (~10μm) faceted particles of Al and Ti($C_{0.5}N_{0.05}$).

The morphology and composition of the particles evolved with the milling time as illustrated in Figure 4.17. The compositional contrast in the BSE - SEM micrographs showed that mainly single phase particles were formed after 12h milling time (Figure 4.17a1). However, the powder contained a proportion of the W-rich particles that were not dissolved (Figure 4.17a2). The EDX and EPMA of the particles indicated that the atomic ratio of the single phase formed after 12h milling was 56±2Ti : 21±2W : 23±2Al.

The composition of the particles milled for 24h was homogeneous (Figure 4.17b1), which could be ascribed to the formation of a single phase product by dissolution of W and Al in Ti(C,N). Some fine W-rich particles were still present, but in reduced proportion and size than in the product obtained after 12h milling. The general composition was more homogeneous in cold welded and in isolated particles milled for 24h (Figure 4.17b2) than in those milled for 12h. The approximate atom compositions of the main phases in the milled particles are given in Table 4.1.

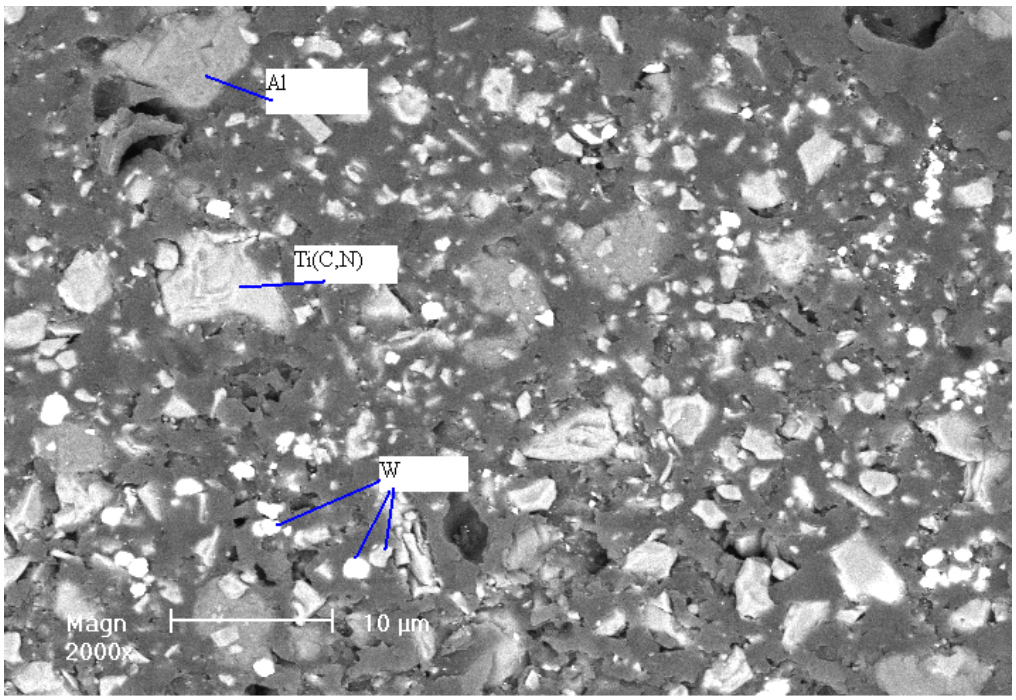

Figure 4.16. Backscattered electron SEM image of the cross section of 55wt% $Ti(C_{0.5}N_{0.05})$ - 35wt% W - 10wt% Al powder particles before milling, showing the three constituents in the starting mixture.

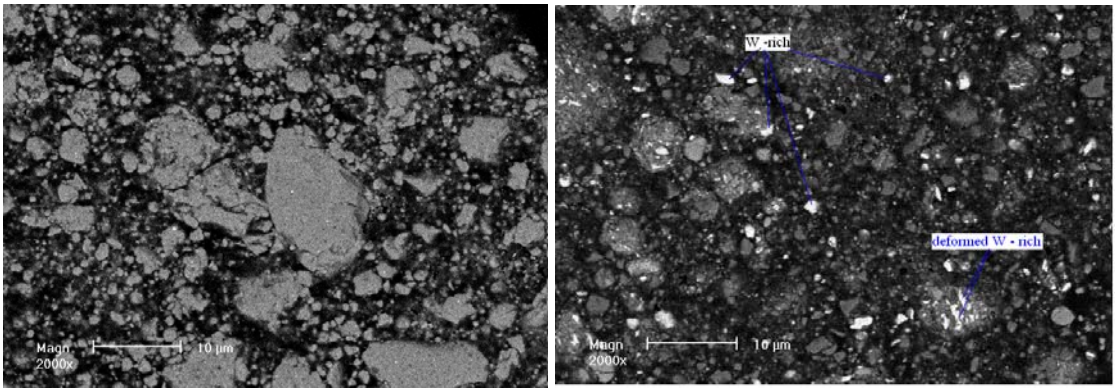

a1. 12h (cold welded) a2. 12h (isolated particles)

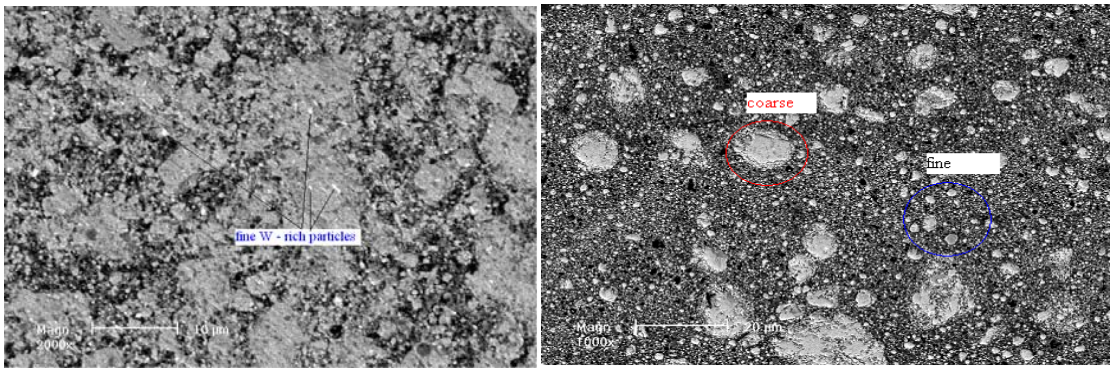

b1. 24h (cold welded) b2. 24h (general microstructure)

Figure 4.17. Backscattered electron SEM images of the cross sections of 55wt% $Ti(C_{0.5}N_{0.05})$ – 35wt% W – 10 wt% Al mechanically alloyed powder particles milled for (a) 12h and (b) 24h, showing the main phase matrix containing fine W-rich particles.

The Ti content of the main matrix phase decreased, whereas W, Al and Fe increased with the milling time. It is reasoned from these variations that W-rich particles containing Al and contaminating Fe were dissolved in $Ti(C_{0.5}N_{0.05})$ as the milling time increased. The size of W-rich particles became subsequently smaller, as observed in Figure 4.17b1.

Table 4.1. Atomic ratios in the matrices of the 55wt% Ti($C_{0.5}N_{0.05}$) - 35wt% W - 10 wt% Al milled particles.

Milling time	**Ti**	**W**	**Al**	**Fe**
12h	2.9	1	1.1	0.3
24h	2.6	1	1.3	0.4

The equilibrium phase diagrams [9] predicted solubility of Ti and Al in W that are lower than 12at.% at 25˚C. Conversely, the atom ratios in Table 4.4 showed that extended solubility of the three elements was achieved by high energy ball milling.

The Al XRD peaks (Figure 4.18) have vanished during the early stage of milling, whereas those of W and Ti($C_{0.5}N_{0.05}$) became broad and had lower intensities due to lattice straining and refinement of the crystallites. This process shows that the kinetics of dissolution of Al atoms in Ti($C_{0.5}N_{0.05}$) and in W was fast. Aguilar *et al.* [107] ascribed the fast destruction of Al structure and the high diffusion coefficient of the atoms in solid state during mechanical alloying to its lower melting temperature.

The tungsten peaks indicate that the BCC lattice was strained and could transform into a structure close to orthorhombic, before their disappearance after 48h milling. It infers from the EDX and EMPA analyses show that part of the Al contained in the mixture has been dissolved in the orthorhombic W.

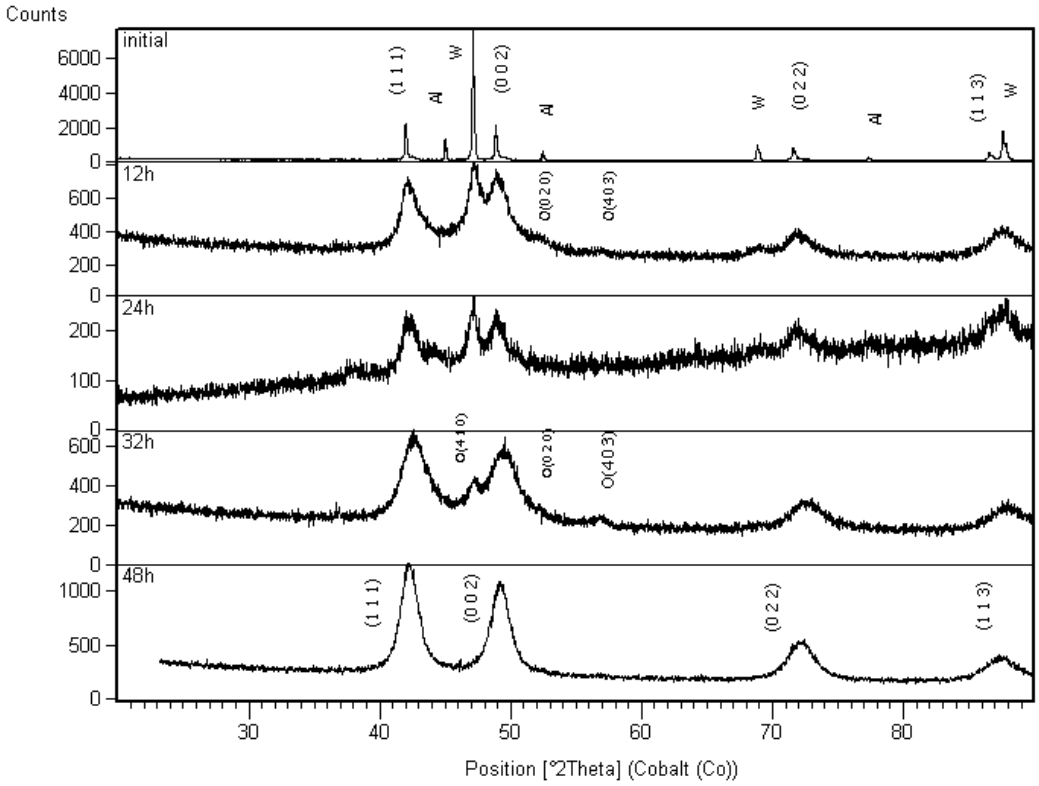

Figure 4.18. XRD peaks of 55wt% Ti($C_{0.5}N_{0.05}$)-35wt% W-10 wt% Al mixtures with the milling time in an argon atmosphere.

The calculated crystallite sizes of the Ti-rich FCC and the W-rich orthorhombic phases formed after the milling time up to 32h varied between 31 and 37 nm. The corresponding crystal lattice strains ranged from 0.21 to 0.32%, which was less than half the lattice strains in the phases formed in the absence of Al for the same time, as discussed in Section 4.1. This implies that Al lowered the lattice strains, and subsequently the strain energy stored by the deformed particles of Ti($C_{0.5}N_{0.05}$) and W, as was also reported by Chen and his co-workers [110] in their work on the competition between elements in mechanical alloying of octonary systems.

Thermodynamic calculations made using the phase diagram module in FactSage 6.1, and the data included in the SGTE database for various temperatures between 25˚C and

1500˚C under pressures up to 10^5 atmospheres showed that solid TiAl, TiN and TiC were likely to be formed in presence of Al, Ti(C,N) and W.

It was noticed (Sections 4.1 and 4.2) that a solid solution was formed by dissolution of the W atoms in the strained crystallites of Ti(C,N). However, the SEM and XRD results of mechanical alloying in the presence of Al show that Al was dissolved first in the two constituents. The crystals of the orthorhombic W(Al) solid solution were then destroyed and W and Al dissolved in the FCC Ti(Al). This process resulted in the formation of the ternary Ti(Al,W) (C,N) FCC solid solution.

The alloying process of the three constituents was completed after 48h milling, whereas dissolution of W in Ti($C_{0.5}N_{0.05}$) was completed after 24h. The slower kinetics of dissolution of W in Ti($C_{0.5}N_{0.05}$) was attributed to the stability of the orthorhombic W(Al) formed in the early stage of milling and to the lower strain energy stored in Ti(Al) crystals.

4.5. Effect of milling at subzero temperature

Another factor determining the mechanical alloying process is the fracturing mechanism. It is believed that most materials are brittle at low temperature, thus the fracturing of powder particles would be easier at lower temperature. However, the coefficients of interdiffusion between the constituents would also be lower at low temperature, which may hinder the presumed advantages of fine particle sizes of the reactants on the kinetics of mechanical alloying.

Cryomilling evolved as a variation of mechanical milling, and involves immersing the milling media in liquid nitrogen or argon [178-181]. The extremely low temperature would suppress the recovery and recrystallisation and lead to finer structures and more rapid grain refinement. It was reported that cryomilling and generally high energy ball milling could be effectively used to fabricate all metals and ceramic-reinforced metals, in which the size of the reinforcement phase can be modified, depending on the milling parameters [182-186].

Several studies have established that the minimum particle size obtainable in nanocrystalline materials milled at subzero temperature decreased as the stacking fault energy, hardness and the self-diffusion activation energy increased [187-189]. Yu *et al.* [187] showed that milling at temperatures in the range of -140˚C to -5˚C significantly enhanced the effectiveness of mechanical milling in refining the Ti/Al composite structure, but Ti(Al) and Al(Ti) solid solutions has not been formed. Cryomilling was also efficient in distributing the harder particles such AlN in a softer matrix like Ni [188].

Almathami and Brochu [190] reported the enhancing effect of Al on the strain-induced BCC-to-FCC transformation of the nanostructured 316L stainless steels by cryomilling. The authors also reported the enhancement of the reverse reaction during the annealing milled products [191]. The essential effect of Al to facilitate the achievement of thermal stability of nanocrystalline structures in cryomilled Fe was noticed by Huang *et al.* [192]. Many other advantages of cryomilling have been reported [192-199]. Zhou *et al.* [196] have reported cryomilled Al and Al alloys that are ductile, but so are most Al alloys.

Mindivan [198] noticed that cryomilling and the subsequent hot pressing steps produced a clean and strong interface between Al and B_4C.

In this work, the effects of mechanical milling at subzero temperatures, and Al addition on the strain induced transformations and reactions in the Ti(C,N) - W powder mixtures were investigated by XRD, TEM, SEM and particle size analysis. The results were discussed and compared to those achieved at about 130˚C reported in Sections 4.1 through to 4.4.

The powder mixtures were loaded in a milling pot with 3mm diameter 3Cr12 stainless steel balls and hermetically closed in a glove box filled with argon gas. The ball-to-powder weight ratio was kept constant at 10:1. The sealed pots were then quenched in liquid nitrogen until the temperature reached -150˚C. They were then mounted on the high-energy ball milling machine, and milling was carried out until the temperature reached -5˚C. The process was interrupted and the pots were again quenched in liquid nitrogen; this was repeated until total milling of 20 minutes, 1h, 4h, 12h and 24h were achieved. A silicon standard and the crystal structure data provided by the ICSD Database, version 2.3 [200] were used for the calculations. The XRD peaks of the $Ti(C_{0.5}N_{0.05})$ - W and $Ti(C_{0.5}N_{0.05})$ - W - Al powder mixtures with milling time are illustrated in Figures 4.20 and 4.21.

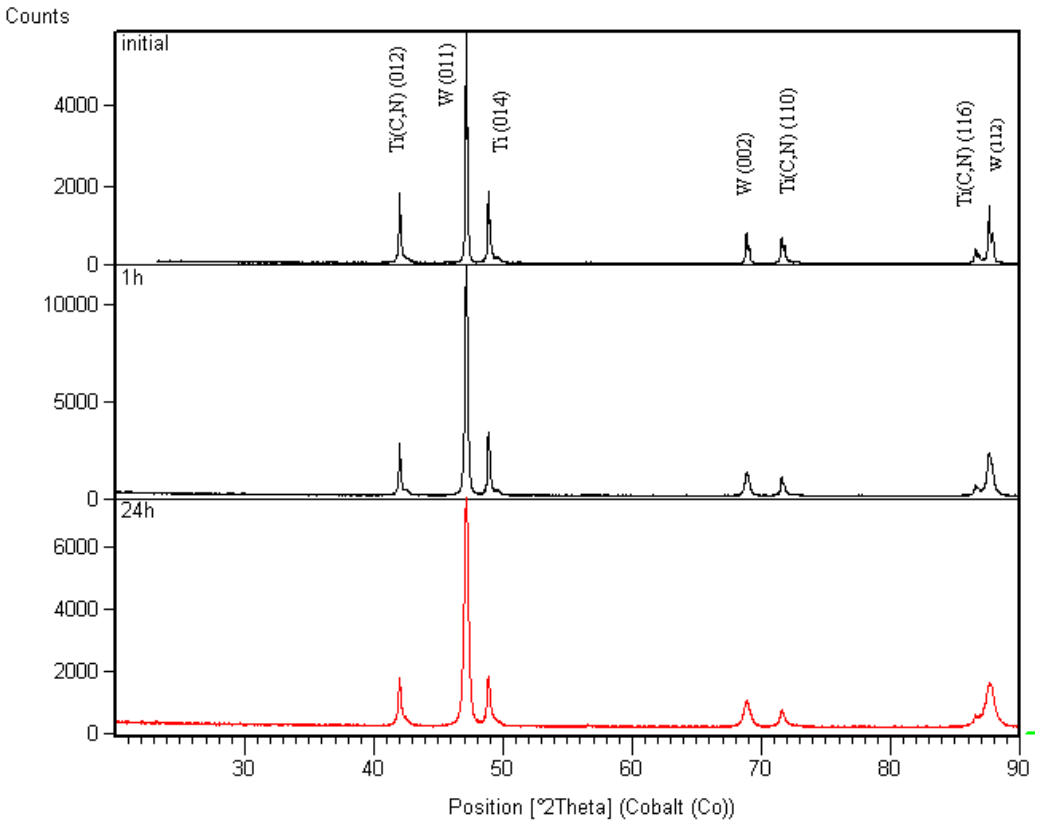

Figure 4.20. XRD peaks of $Ti(C_{0.5}N_{0.05})$ – 40wt% W powder mixtures milled between -140˚C and -5˚C for up to 24h.

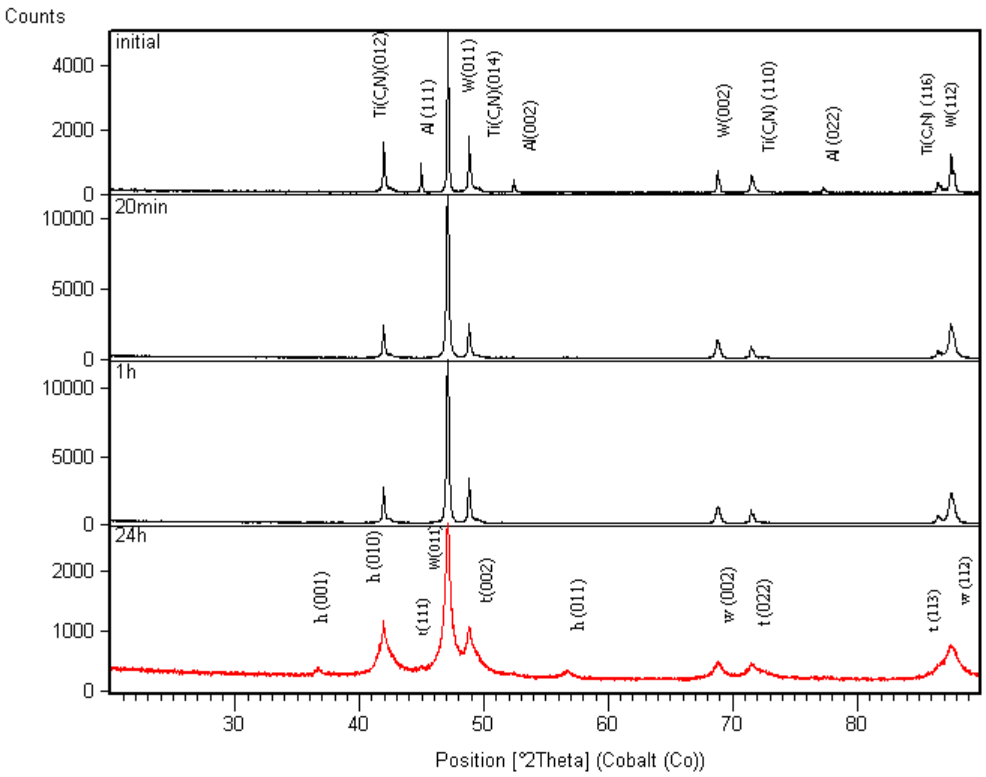

Figure 4.21. XRD peaks of 55wt% $Ti(C_{0.5}N_{0.05})$ - 35wt% W - 10 wt% Al powder mixtures milled between -140˚C and -5˚C for up 24h, showing the peaks of the HCP $W_{0.505}Al_{0.495}C_{0.5}$ phase (h), the FCC Ti-rich phase $Ti_{0.8}W_{0.2}C$ (t) and the BCC $Ti_{0.17}W_{0.66}Al_{0.17}$ (w) formed after 24h milling.

It was observed that the intensities of the W peaks milled without (Figure 4.20) or with Al (Figure 4.21) for 20 minutes doubled from their initial values and became sharper before a slow decrease was noticed at 1h milling. The increase of peak intensities of $Ti(C_{0.5}N_{0.05})$ was less significant. However, the Al XRD peaks were shorter and broader after 20 minute milling due to the refinement of the powder particles and the increased lattice strain. These peaks disappeared from the patterns (Figure 2) after 1h milling.

The diffraction angles of both $Ti(C_{0.5}N_{0.05})$ and W milled with Al increased showing a reduction of their respective d-spacings due to the solid solution by substitution of Ti and

W by the smaller Al atoms in the crystals. The Al atom radius is at about 12% smaller than that of Ti [201].

It can be inferred from the XRD analysis that Al crystals were strained and quickly destroyed after short milling times. The Al atoms then reacted with the other constituents of the mixtures to form the HCP $W_{0.505}Al_{0.495}C_{0.5}$ phase (h), the intermetallic BCC $Ti_{0.17}W_{0.66}Al_{0.17}$ compound (w) and the FCC $Ti_{0.8}W_{0.2}C$ compound (t) after 24h milling. The semi-quantitative weight composition of these compounds calculated from the areas of the XRD peaks in the final product was about 49% (t), 39% (w) and 12% (h). The transformation and reaction mechanisms were explained with respect to the evolution of the crystallite strains and sizes of the products formed as the milling time increased. The results are presented in Figure 4.22.

The lattice strains of W and Ti($C_{0.5}N_{0.05}$) milled without Al (doted lines W(1) and Ti($C_{0.5}N_{0.05}$) (1)) in Figure (4.22.a) decreased during the first 20 minutes. The decrease in lattice strains contributed to the increased XRD peak intensities observed at the short milling times of 20 minutes and one hour. The lattice strains increased thereafter as the milling was prolonged.

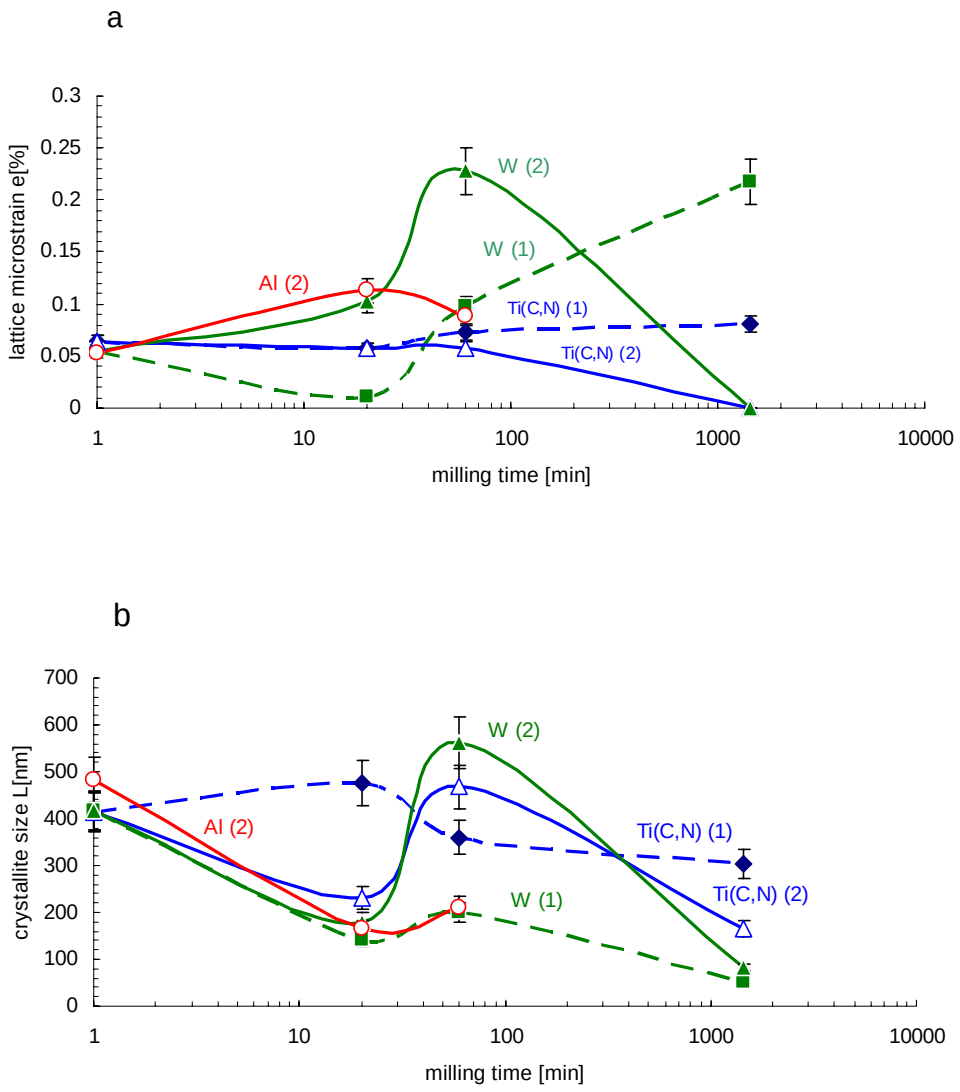

Figure 4.22. Calculated microstrains e [%] and crystallite sizes L [nm] of W and $Ti(C_{0.5}N_{0.05})$ powders and the products milled at subzero temperature – indices (1) in Ti(C,N) - 40%W mixtures and (2) in 55%Ti(C,N) - 35%W - 10%Al mixtures.

A different trend was observed in powders milled with Al (solid lines W(2) and $Ti(C_{0.5}N_{0.05})$ (2)) in Figure (4.22.a). In this case, the lattice strains increased during the first hour of milling in the W crystallites (e = 0.23%) more than $Ti(C_{0.5}N_{0.05})$ (e = 0.07%) before decreasing to minima (~0.01%) that were lower than the initial strains (~0.06%).

The relaxation after the strain maxima were reached, which was not observed in the case of milling without Al, was ascribed to the formation of the solid solutions and reactions between the powder constituents. The release of lattice strain energy stored contributed to the driving force for mechanical alloying.

The XRD results showed that the lattice strains necessary to activate the materials in W and Ti($C_{0.5}N_{0.05}$) particles before reaction were higher during milling with the soft Al. The strain of Al crystallites also increased during the first 20 minutes before the destruction of the crystals. The larger magnitude of relaxation of lattice strain of the milled W comparatively to Ti($C_{0.5}N_{0.05}$) indicates that Al preferably reacted with W and formed the compounds (h) and (w). The W excess dissolved in Ti($C_{0.5}N_{0.05}$) and formed the product (t).

Binary titanium aluminides were not formed during milling below -5˚C for 24h, as also reported by Yu *et al.* [187]. However, ternary Ti - W - Al (h), W - Al - C (w) and Ti - W - C (t) were formed in the same conditions. The large lattice strain in W crystals and the release of the stored energy as milling time increased was therefore the determinant factor of the driving force for alloying.

It was also noticed that the lattice strain of W crystals increased faster in the presence of Al than in its absence (lines W(2) and W(1) respectively in Figure 4.22.a). The increase of lattice strains in the presence of Al was ascribed to the dissolution of Al atoms in W lattices. Hence the order of reactions was as follows:

$$W + Al \rightarrow W(Al) \quad (4.7)$$

$$W(Al) + Ti(C,N) \rightarrow W(Al,Ti) + W(Al,C) + Ti(W,C,N) \quad (4.8)$$

The final products correspond to the compounds (w), (h) and (t) respectively. The crystalline W - Al compounds (h and w) formed at low temperature were stable and the subsequent dissolution of W in the Ti-rich compound (t) was limited.

Equation 4.7 represents the dissolution of Al in W, which is the missing step when milling in the absence of Al, that explains the slower increase of W lattice strain, hence the absence of alloying of W with Ti(C,N) after 24h at low temperature.

Therefore, interaction between W and Al improved the kinetics of transformation during milling at subzero temperatures by two mechanisms:

- the increase of lattice strain during short milling time before relaxation at longer time
- and the fast diffusion of Al atoms during milling.

However, the alloying of W with $Ti(C_{0.5}N_{0.05})$ was slower than observed during ball milling at higher temperatures [Sections 4.1 - 4.4].

It was noticed in Figure 4.22.b that the crystallites of the activated tungsten and titanium carbonitride (W(2) and $Ti(C_{0.5}N_{0.05})$ (2)) milled with Al for 1h were large and were refined thereafter to ~100nm and ~200nm respectively after formation of the products (w) and (t) that occurred at 24h milling.

Thus, Al decreased the rate of fracturing of the hard W and Ti($C_{0.5}N_{0.05}$) particles. This indicated that the mechanical energy input in the first stage of milling serves to deform the particles of the softer constituent of the mixtures.

The microstructures of powders processed for 1h and 24h are illustrated in Figure 4.23. The particles of the milled W-rich products (w and h) formed in the presence of Al (Figure 4.23.c) were ductile and more plastically deformed than W particles milled without Al (Figure 4.23.a). The degree of homogeneity and phase distribution in the microstructures indicated that the diffusion and dissolution of the constituents were faster in the mixtures containing Al (Figure 4.23.c) than in those without Al (Figure 4.23.a). As milling time increased to 24h, the particles of W - Al compounds (w and h) were finely dispersed in the Ti-rich matrix product (t) that dissolved a limited amount of W (Figure 4.23.d), whereas particles of Ti($C_{0.5}N_{0.05}$) and W milled without Al (Figure 4.23.b) were deformed but not alloyed.

The evolution of the morphologies of Ti($C_{0.5}N_{0.05}$) - W mixtures show that fracturing of hard particles dominated in the early stage of milling in the absence of Al (Figure 4.23.a), whereas plastic deformation of particles and cold welding of Ti($C_{0.5}N_{0.05}$) and W particles by the softer Al prevailed at the same time (Figure 4.23.c), in the second type of mixture. The contact between the strained Al particles and the Ti($C_{0.5}N_{0.05}$) and W particles enhanced the diffusion of Al atoms in the particles and the formation of the W-Al compounds (w and h) detected in the XRD patterns.

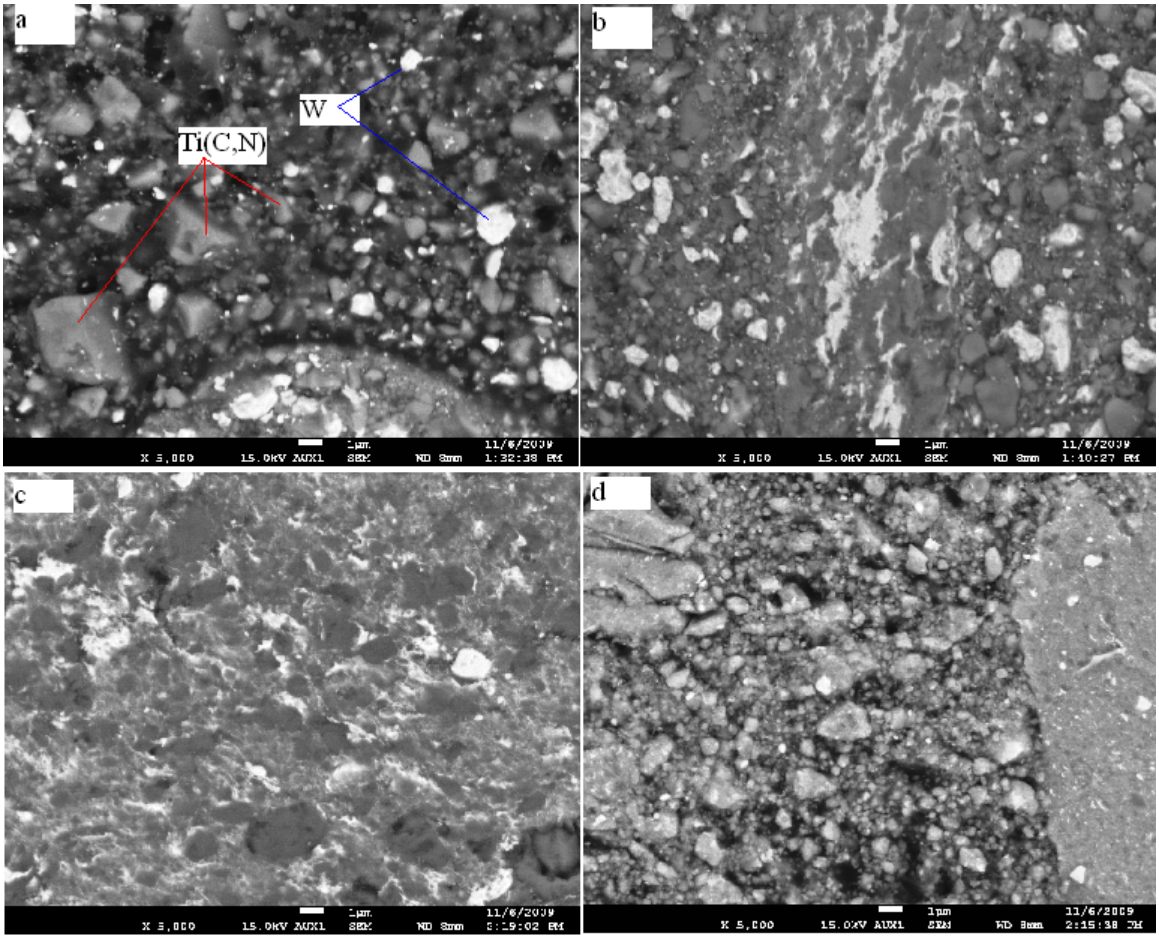

Figure 4.23. BSE - SEM micrographs of the cross sections of powder particles of $Ti(C_{0.5}N_{0.05})$ - 40%W milled for (a) 1h, (b) 24h and $Ti(C_{0.5}N_{0.05})$ - 35%W - 10%Al mixtures milled for (c) 1h and (d) 24h at subzero temperatures, showing Ti-rich particles (dark) and W-rich particles (bright).

The yield of the process decreased below 20% as the milling time increased to 1h due to cold welding, and most importantly to the low temperature high viscosity of the aluminium stearate used as the process control agent. Flocs larger than 500µm were formed as shown in Figure 4.24. Thus, the high viscosity of the process control agent (PCA) became detrimental to the alloying process. The formation of viscous films of PCA around the particles decreased the rate of deformation, and thus the strain of the crystallites necessary to initiate the dissolution of powder constituents.

The inhibition was significant in mixtures milled without Al. It would therefore be advantageous to mill at subzero temperatures without adding the PCA to the powders.

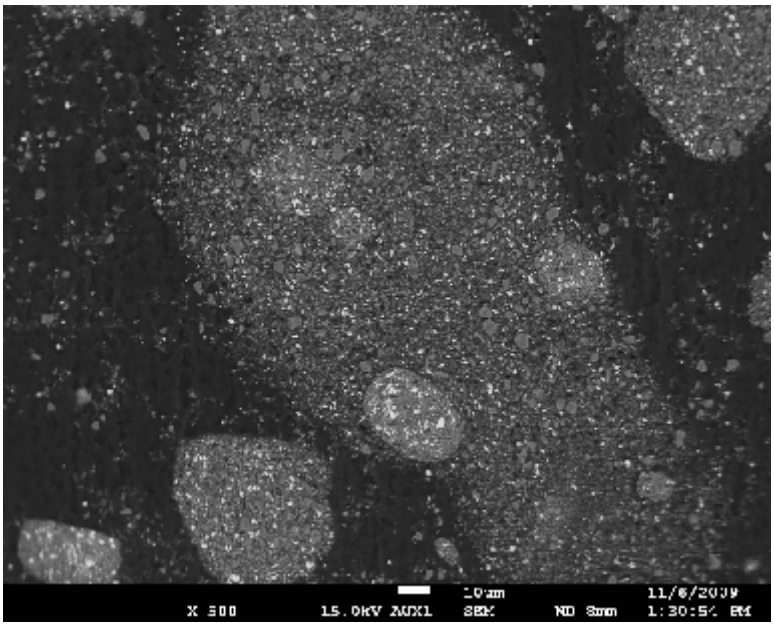

Figure 4.24. BSE-SEM of $Ti(C_{0.5}N_{0.05})$ and W particles milled at subzero temperatures for 1h in the absence of Al, showing large flocs of particles agglomerated by the PCA.

The transformation steps observed during milling at subzero temperatures could be summarised as follows in Table 4.2. Transmission electron microscopy observations confirmed the presence of non-reacted particles in mixtures milled for 24h without Al (Figure 4.25.a). Conversely, with Al, dissolution and reactions between $Ti(C_{0.5}N_{0.05})$, W and Al were achieved in the same conditions (Figure 4.25.b). The particles of W-Al compounds (dark contrast regions) were dispersed in the Ti-rich matrix (bright contrast regions) and strained due to the suppression of the recovery and recrystallisation processes at low temperature.

Table 4.2. Transformation steps during mechanical milling at subzero temperature of $Ti(C_{0.5}N_{0.05})$ - 40%W and $Ti(C_{0.5}N_{0.05})$ - 35%W - 10%Al mixtures.

	Time	**No Al**	**With Al**
		$Ti(C_{0.5}N_{0.05})$ - 40%W	**$Ti(C_{0.5}N_{0.05})$ - 35%W - 10%Al**
Early stage	20 minutes	Fracturing of W particles	Plastic deformation of Al particles; Straining of Al crystallites
Intermediate stage	1h	Straining of W and $Ti(C_{0.5}N_{0.05})$ crystallites	Dispersion of Al atoms in the activated mixtures. Formation of W(Al).
Final stage	24h	Straining of W and $Ti(C_{0.5}N_{0.05})$ crystallites	Reaction between W(Al) and Ti(C,N); Limited dissolution of W in Ti(C,N); Dispersion of W – Al compounds in the Ti – rich matrix.

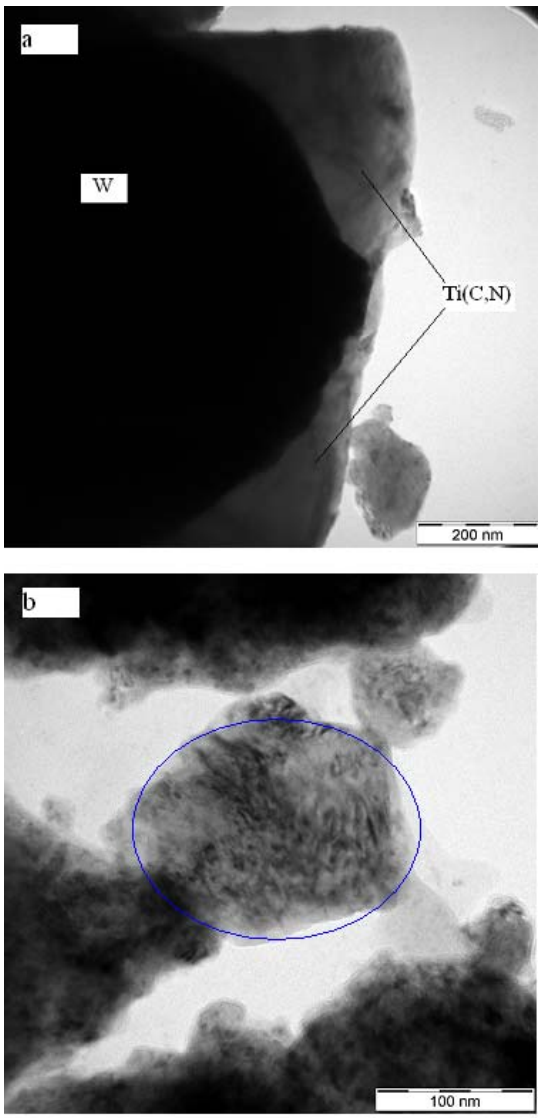

Figure 4.25. TEM micrograph of powder mixtures milled at subzero temperatures for 24h, (a) without Al showing W particles embodied in $Ti(C_{0.5}N_{0.05})$ and (b) with 10% Al showing a dispersion of W-rich phases (dark regions) in strained particles of the Ti-rich matrix particles.

CHAPTER 5. THERMALLY INDUCED TRANSFORMATIONS IN POWDERS PROCESSED BY HIGH ENERGY BALL MILLING

5.1. Purpose

The characterization of transformations taking place during the heating of mechanically alloyed powders is of interest both theoretically and practically when these powders are intended to be used as cermets or binders in hard materials, high temperature alloys and magnetic alloys.

The effect of the starting powder composition and milling conditions on the crystal structure, product phase compositions and mechanical alloying process were analysed in Chapter 4. It was particularly observed that intermediate and final products were formed during milling. The crystallite lattice strains of the intermediate phases could be high, and the release of the stored lattice strain energy contributed to the driving force for alloying of the powder constituents.

It was important to investigate the effect of annealing treatment on the transformation of the metastable phases hence formed, in order to isolate the effect of high temperature on the mechanically alloyed binders from the interactions with cubic boron nitride particles during HPHT sintering. These interactions are elaborated in Chapter 6.

Gordo *et al.* [79], Gómez *et al.* [80] and Cordoba *et al.* [71] reported that milling conditions influenced the microstructure and properties of the sintered Fe-TiCN-(Co/Ni) metal-ceramic composites materials. The authors reported the formation of finer microstructures and better mechanical properties in the sintered composites made of mechanically alloyed powders that were milled for longer times.

In the present study, the transformation temperatures of the powder products were determined by means of differential thermal analysis, DTA. The milled powders were subsequently annealed at normal pressure, in an argon atmosphere, for 2 hours at temperatures near the transformation temperatures estimated from the DTA curves. The phases formed upon annealing were characterised using SEM, TEM and XRD.

5.2. Transformation temperatures and annealing of $Ti(C_{0.5}N_{0.05})$ - W ball milled powders

The DTA heating curves of $Ti(C_{0.5}N_{0.05})$ - 40wt% W powder mixtures milled for different times are shown in Figure 5.1. The broad exothermic peaks in the temperature range from 950 to 1400˚C were ascribed to the heat of reactions between powder constituents, which were enhanced by the thermally-activated diffusion of the atoms. Two local maxima of temperature changes were recorded at about 1100˚C and 1250˚C in the heating curves of powders milled for 12h. The maxima had converged into one between 1100˚C and 1150˚C when the milling time increased to 48h.

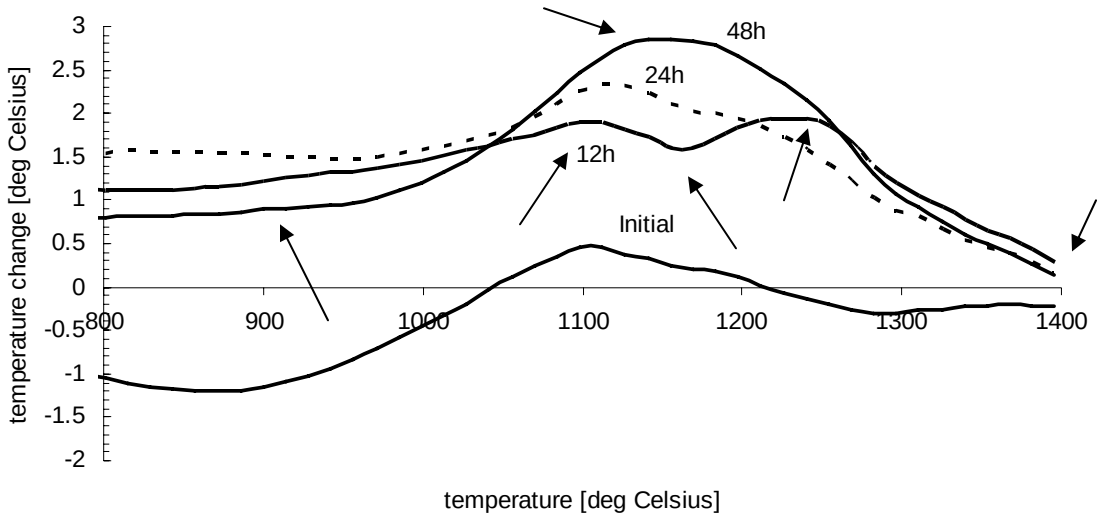

Figure 5.1. Heating curves of $Ti(C_{0.5}N_{0.05})$ - 40wt% W mixtures milled for different times in an argon atmosphere; reaction onsets, maxima of temperature changes and the reaction finish temperatures are indicated by the arrows.

The two local maxima on the heating curve of the powders milled for 12h indicate that the transformations or reactions of the constituents occurred in more stages than in the powders milled for 48h. Thus, the decrease in number of maxima and inflexion points on the DTA curves was attributed to the homogenization and completion of the solid solution process by mechanical alloying as the milling time increased from 12 to 48h.

The number of product phases decreased as the milling time increased and the number of reactions between those constituents was consequently reduced. Therefore, the formation of a single peak on the DTA curve of the powder milled for 48h was attributed to more complete dissolution and homogenization of the products milled for longer times. The peaks observed on the heating curves of the milled powders were broad and smooth. However, the maxima temperature changes recorded were 1.5, 2.3 and 3˚C for the powders milled for 12, 24 and 48h respectively.

Some maximum and inflexion points are indicated by the arrows in Figure 5.1. The large portion of the heating curve of the non-milled mixture was characterized by a negative temperature change which indicates that the heat input was consumed to compensate for the latent heat. Positive temperature changes were observed between 1050˚C and 1220˚C but they were smaller than 0.5˚C. On the other hand, the reactions between the constituents of the milled powders started at about 950˚C, peaked between 1100˚C and 1200˚C and were completed at about 1400˚C. The corresponding maximum temperature changes increased from +1.5 to +3˚C as the milling time increased from 12h to 48h.

The small temperature change observed in heating of the non-milled powders indicates that the amount of heat of reaction released was smaller. Hence, the thermally induced chemical reaction between Ti(C,N) and W pure particles was not complete. Milling improved the kinetics of reaction and hence the degree of completion of the alloying process due to the large contact surface between the fine grains and the dispersion of W atoms in the Ti(C,N) particles. The amount total of heat released and the temperature change subsequently increased with the milling time.

The low reaction start temperatures compared to the melting temperatures of the powder constituents were ascribed to the lower activation energies to thermally induce alloying or chemical reactions between the species. The lattice strain energy stored in the milled particles, and the defects introduced in the crystals contributed to the fast kinetics of reactions in the mixtures milled for longer times.

The X-ray diffraction patterns of the powder mixtures milled for 48h and annealed at different temperatures (Figure 5.2) show that the FCC solid solution, phase (2), formed after milling for 48 hours, had crystallized into an FCC phase, (2́), after heating to 1085˚C and cooling to room temperature.

The peaks of the FCC phase (*2'*) shifted to the lower 2θ angles as the annealing temperature increased, indicating an increase in d-spacing that was attributed to thermal alloying of W atoms in Ti(C,N). Amounts of the γ-Fe-Ni (7) and α-Fe-W-Cr phases (8) were formed in material annealed at 1085˚C and 1125˚C due to the contamination of the milled powders by the constituents from the 3Cr12 stainless steel milling balls. However, the corresponding peaks were not detected in the milled powders before annealing because these contaminants were dissolved in the solid solution.

A rhombohedral phase (10) was formed during annealing at 1285˚C and its proportion, along with that of an unknown product (11), increased as the temperature increased to 1485˚C. The vanishing of the peaks of phases (7) and (8) at higher temperatures was due to the dissolution in the matrix. The composition of the phases indicated that the contaminating Cr, Fe and Ni preferably alloyed with W rather than with Ti during the annealing. The calculated lattice parameters of the FCC matrix phase Ti(W,C,N) (2') are given in Table 5.1. The lattice parameters were calculated after identification of XRD peaks as shown in Figure 5.2. The increase in lattice parameters of the annealed matrix was equally ascribed to the thermal dissolution of W atoms in titanium carbonitride.

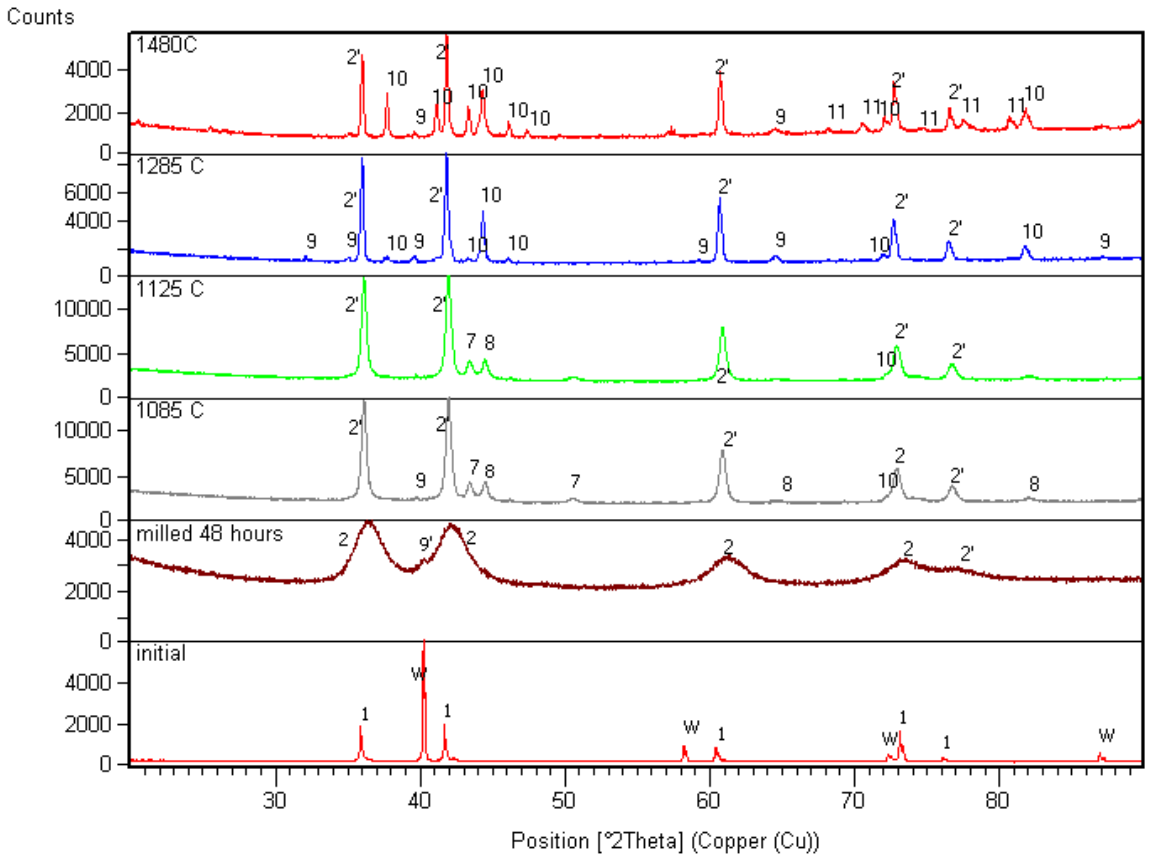

Figure 5.2. X-ray diffraction patterns of the phases formed upon annealing at various temperatures of $Ti(C_{0.5}N_{0.05})$ - 40 wt% W powders milled for 48h. Mechanically alloyed solid solution phase (2); phase (2′) crystallized after annealing and cooling to room temperature; Tungsten (9); γ-Fe-Ni phase (7); α-Fe-W-Cr phase (8) and an unknown rhombohedral phase (10).

Table 5.1. Lattice parameters [nm] of the matrix phase (2') formed in $Ti(C_{0.5}N_{0.05})$-40 wt% W powders milled for 12h or 48h and annealed at 1085 or 1285˚C

	As milled	**Annealed at 1085˚C**	**Annealed at 1285˚C**
Milled 12h	4.3058	4.3042	4.3167
Milled 48h	4.2764	4.2998	4.3070

The formation of the two contaminant phases shows that Cr, Fe and Ni separated from the mechanically alloyed solid solution during annealing. These contaminant atoms then readily reacted and formed new compounds, preferably with tungsten rather than with titanium during the annealing treatment.

The XRD patterns of the mixtures milled for 12h and subsequently annealed at various temperatures (Figure 5.3) indicated a separation of the constituents annealed below 1285˚C and the formation of new phases at higher temperatures. Tungsten peaks disappeared after annealing at 1480˚C. However, unlike the thermal alloying of W with Ti(C,N) during the annealing of powders milled for 48h, the XRD results showed that the disappearance of the W peaks of the powders milled for 12h annealed at 1480˚C resulted from the formation of the Fe_7W_6 intermetallic phase (13).

Comparison of the XRD peaks (Figures 5.2 and 5.3) shows that milling time influenced the phases formation upon annealing. The characteristic peaks of the products of samples milled became sharper after annealing at 1085˚C.

It was earlier noticed from the DTA heating curves that the transformation temperatures were lower than this temperature and the heat effects were higher for the products of the longer milling times. The crystallisation of the mechanically alloyed matrix, the crystallite growth and the thermal relaxation of lattice strains were therefore faster in mechanically alloyed powders which were milled for longer times.

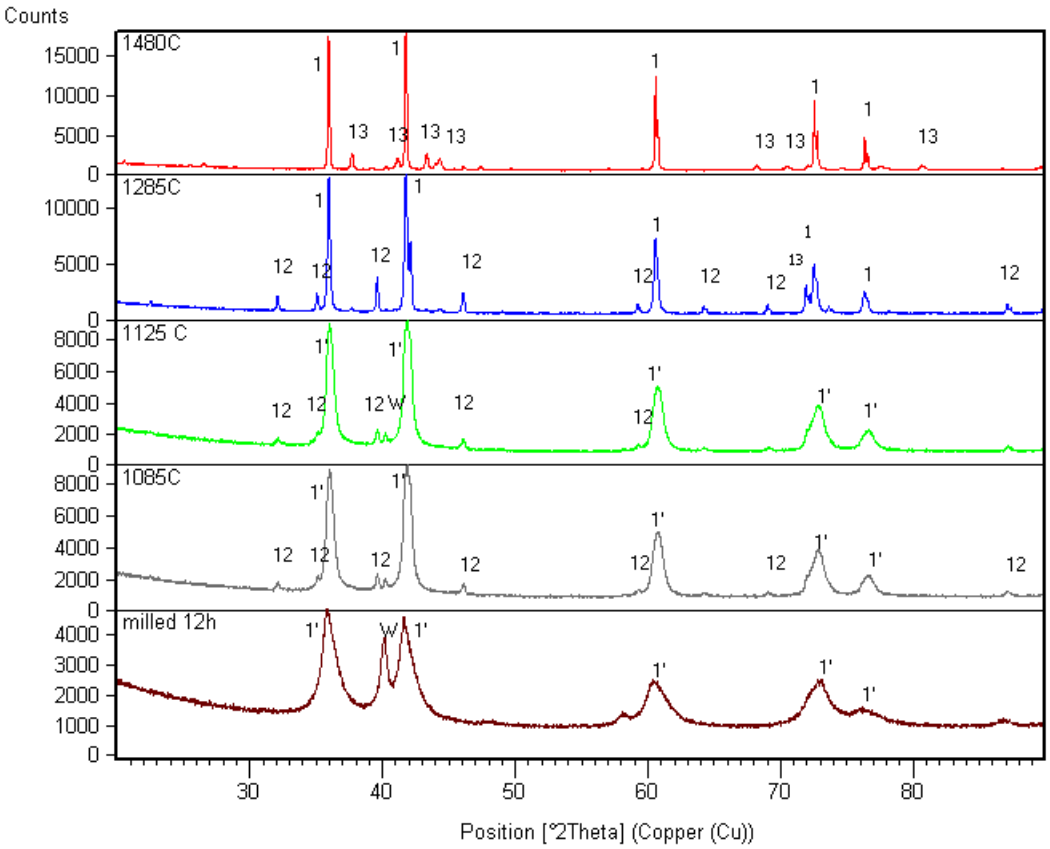

Figure 5.3. X-ray diffraction patterns of phases formed upon annealing at various temperatures of the Ti($C_{0.5}N_{0.05}$) - 40 wt% W milled for 12h. Strained Ti($C_{0.5}N_{0.05}$) phase (1´); annealed Ti($C_{0.5}N_{0.05}$) phase (1); Fe_3W_3N FCC phase (12); Fe_7W_6 intermetallic phase (13).

The XRD patterns indicate a separation of the constituents of the Ti($C_{0.5}N_{0.05}$) - W powder mixture milled for 12h, and annealed at 1285˚C. The characteristic peaks of Fe_3W_3N, FCC phase (12), and W appeared beside those of the initial Ti($C_{0.5}N_{0.05}$) phase (1) as shown in figure 5.3.

The matrix of the material obtained after milling for 12h and annealing at 1480˚C consisted of Ti($C_{0.5}N_{0.05}$) rather than a Ti($C_{0.5}N_{0.05}$) - W solid solution. It can be inferred from Table 5.1 that the lattice parameters of the matrix phase (1') were bigger than those

of (2') due to the thermal relief of the lattice strain of the powder particles and the de-mixing of W which thermally alloyed with Fe and the other contaminants.

The thermally induced dissolution of W and the formation of intermetallic compounds during annealing of milled powders led to the decrease in lattice strains of the Ti-rich matrices as shown in Figure 5.4. Hence, the release of the stored lattice strain energy from the crystals contributed to the driving force for the annealing reactions.
It is reasoned from this observation that the stable solid solutions or intermetallic compounds formed upon annealing corresponded to the lowest lattice strains, but surely only if they reached equilibrium.

It was noticed that the crystallite sizes increased, whereas the lattice strains decreased as the annealing temperature increased. However, a sort of plateau (constant strain/constant crystallite size) was observed between 1050˚C and 1250˚C, which was ascribed to the thermally-induced dissolution/precipitation of the non-dissolved W-rich and the contaminating phases.

The increase of the lattice strain of the powder milled for 12h, and the decrease in crystallite size when annealed at about between 1125 and 1285˚C, was attributed to the decomposition of the metastable product, and separation of W atoms from the titanium carbonitride. Tungsten atoms reacted with iron to form Fe_3W_3N. The lattice strains of the matrix decreased from 0.46% for powders milled for 12h, to values below 0.08% as the annealing temperature increased to 1480˚C.

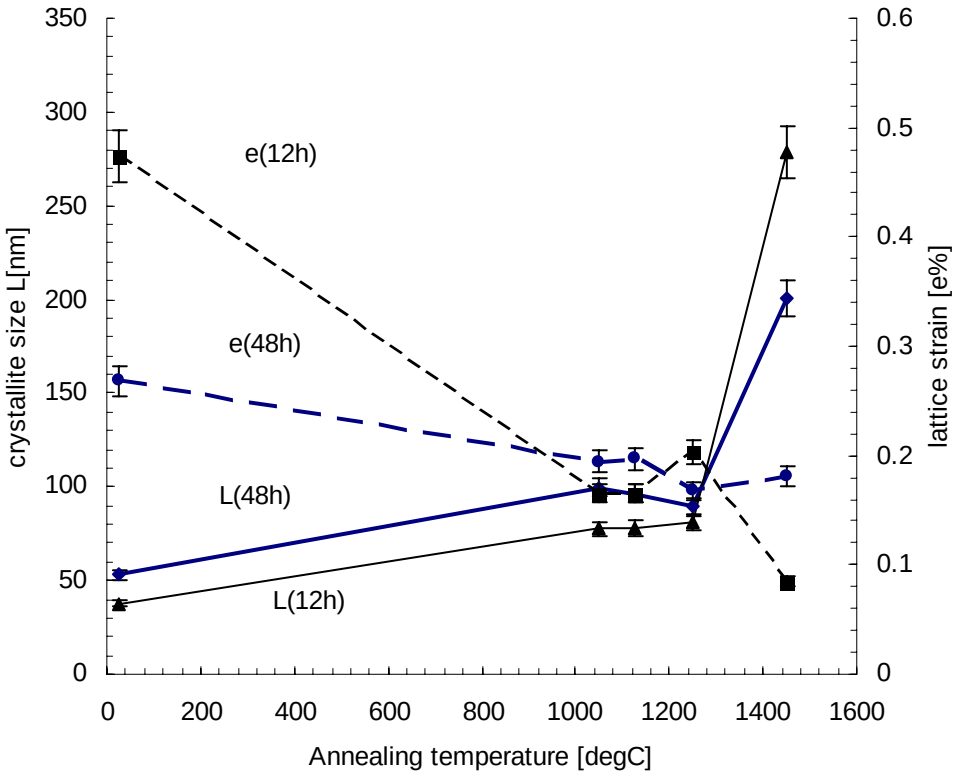

Figure 5.4. Variation of the crystallite sizes (*L*) and lattice strains (*e*) of the matrices of $Ti(C_{0.5}N_{0.05})$ - 40 wt% W powders milled for 12h and 48h with annealing temperature.

The decrease of the lattice strain in the powder matrix milled for 48h was 0.25 to 0.18%, which was smaller than in the powders milled for 12h. The smaller residual lattice strain was attributed to a proportion being relieved upon dissolution of W atoms that led to mechanical alloying with $Ti(C_{0.5}N_{0.05})$.

Selected area electron diffraction patterns (SADP) of the products milled for 48h and annealed at 1480˚C exhibited Kikuchi lines characteristic of strain free crystals as illustrated in Figure 5.5.

The lattice strains of the Ti-rich phases determined by XRD were below 0.08% and 0.18% for the annealed products initially milled for 12 and 48h respectively.

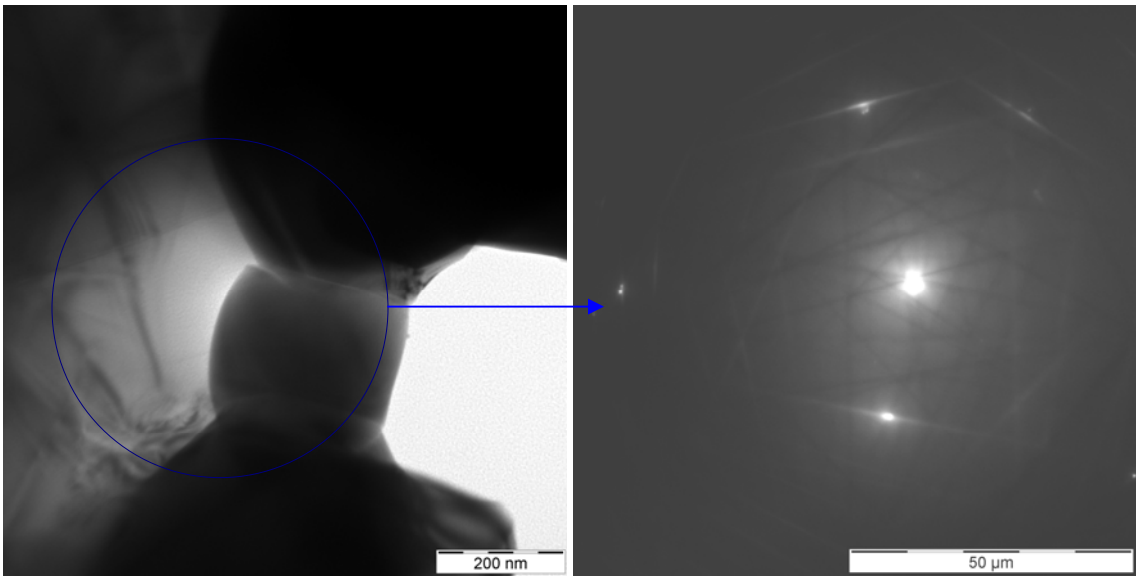

Figure 5.5: TEM image of crystals of $Ti(C_{0.5}N_{0.05})$ – W matrix milled for 48h and annealed at 1480˚C, and the corresponding electron diffraction pattern showing the Kikuchi lines.

Unlike in the electron diffraction patterns of alloyed particles annealed at 1480˚C, the SADP of powder annealed between 1085 and 1125˚C did not contain Kikuchi lines (Figure 5.6). The corresponding electron diffraction pattern showed that the powder product milled for 48h and annealed at low temperatures contained small randomly orientated crystals of an FCC phase. The lattice strain was not fully relieved at these temperatures, although it decreased after annealing at higher temperature as was concluded from the XRD analysis.

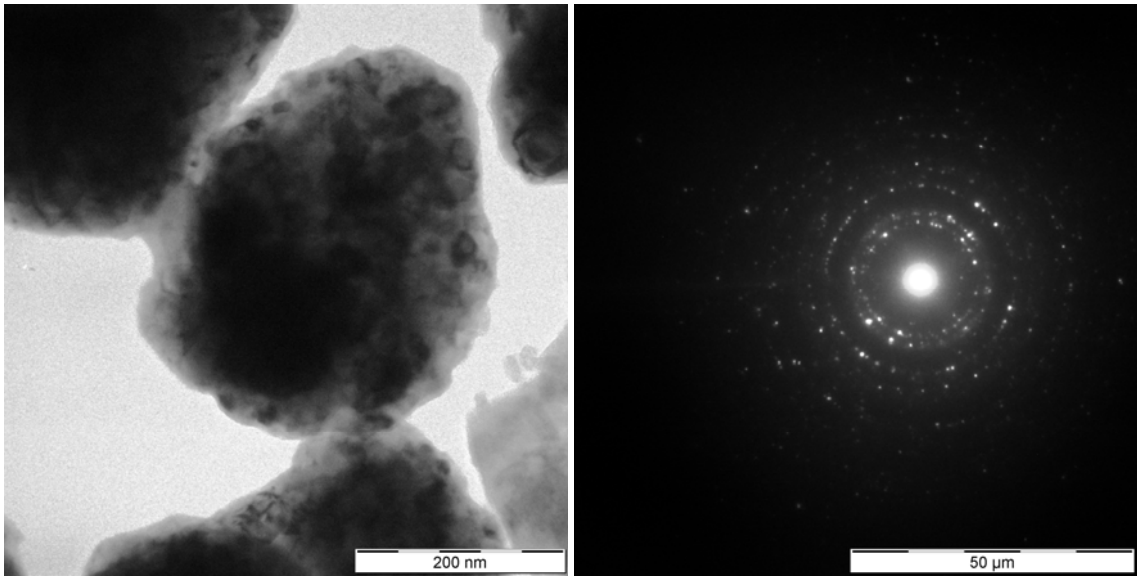

Figure 5.6. TEM of particles of Ti($C_{0.5}N_{0.05}$) -W-Al particles milled for 48h and annealed in the temperature range 1085 - 1125˚C, with the corresponding electron diffraction pattern revealing the presence of small particles of an FCC crystalline phase.

5.3. Microstructure of Ti($C_{0.5}N_{0.05}$) - W mechanical alloys annealed in argon atmosphere at ambient pressure

The effect of the milling time and the annealing temperature on the microstructure and the phase compositions of Ti($C_{0.5}N_{0.05}$) - 40wt% W are discussed in relation with the XRD and TEM results presented in Section 5.2. The evolution of the microstructure is illustrated in Figures 5.9.

The cross sections of the powder particles annealed at 1480˚C (Figure 5.9c) contained two phases with different Ti:W atom ratios; e.g. 3:1 in the main constituent and 1:6 in the second phase. The Ti-rich phase only contained ~2wt% Fe with no Cr, whereas the W-rich phase contained ~13% Fe and ~4% Cr. Hence, agreeing with the XRD analyses,

EDX confirmed that the contaminants from the stainless steel milling balls mainly alloyed with W. The decrease of Ti:W atomic ratio of the major phase formed at the higher temperatures was attributed to the dissolution of the Fe-Cr-W phase constituents into the Ti-rich particles.

Part of the W-rich phase containing atomic ratio (1 Ti : 6 W) formed at 1285˚C was thermally dissolved and alloyed to the Ti-rich phase (7 Ti : 1 W) as the annealing temperature increased to 1480˚C. This process resulted in the formation of the phase containing atomic ration (3 Ti : 1 W). Thermal alloying of the elements occurred simultaneously with the formation of the Fe_3W_3N and FeWCr intermetallic compounds detected in the annealed powders by XRD.

The selective partition of the contaminating elements suggests that W, Fe and Cr powders can form ternary alloys when processed by high energy ball milling and annealed at about 1285˚C. Mechanical alloying of Ti with Cr would be unlikely to happen in the same conditions in the presence of W, which has higher affinity for Cr and Fe.

The Ti-W equilibrium phase diagram (Figure 1.a) shows negligible solubility W in Ti and about 10at.% Ti at 25˚C (room temperature). However, the major constituent of the milled and annealed powders contained more or less 25at.% W dissolved in Ti. High energy ball milling and the presence of carbon in the sub-stoichiometric titanium carbonitride appeared to have enhanced the solubility of W in Ti beyond the equilibrium composition range as also reported in other material systems prepared by mechanical

alloying [1, 2, 7, 8, 72-78]. It was therefore a metastable phase, an intermetallic compound or a new solid solution.

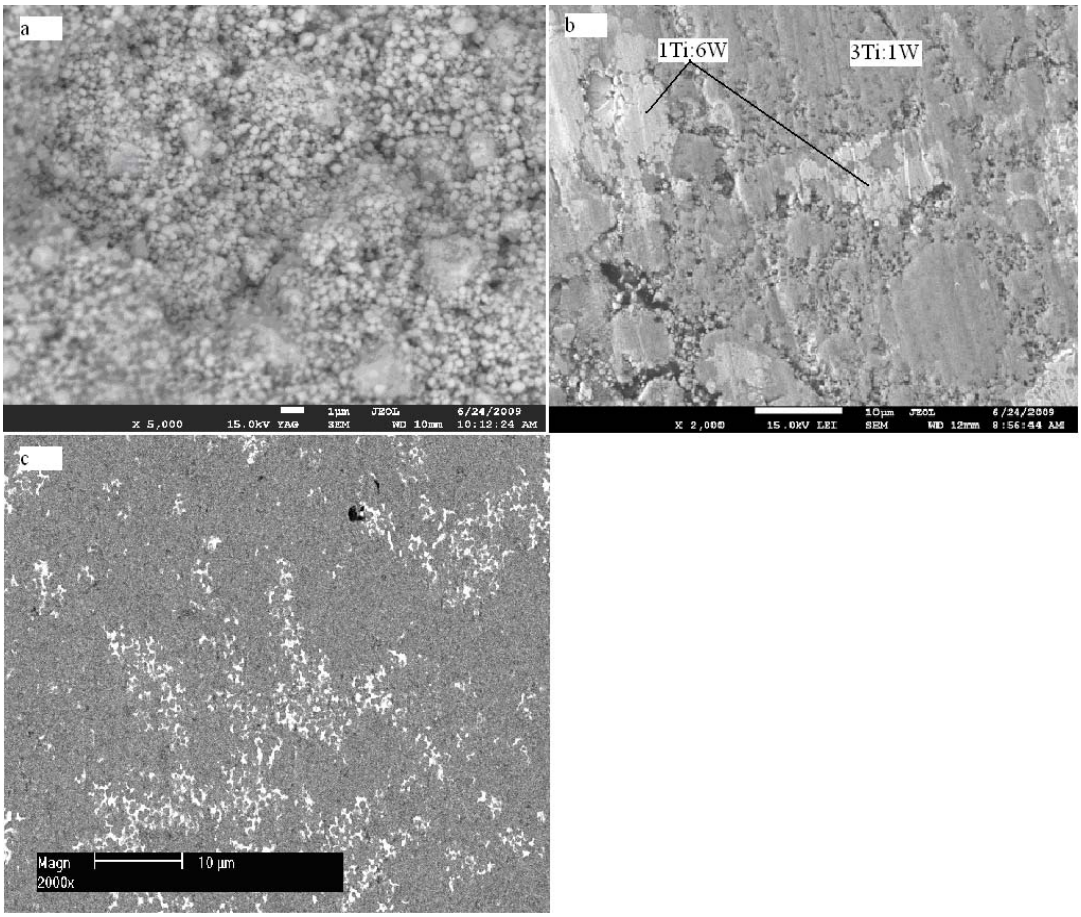

Figure 5.9. BSE-SEM micrographs showing the microstructures of $Ti(C_{0.5}N_{0.05})$ - 40 wt% W mixtures milled for 48h and annealed in argon (a) at 1085˚C, (b) at 1285˚C and (c) at 1480˚C.

As observed from the SEM results, it was noticed that materials annealed at 1085˚C consisted of isolated powder particles (Figure 5.9a). Bonding between particles occurred above 1285˚C as shown in Figures 5.9b and 5.9c. The effect of the milling time on the microstructure of the powders annealed at 1480˚C is illustrated in Figure 5.10. The powder that was annealed without being milled was characterized by a coarser

distribution of Ti and W phases (Figure 5.10a). The microstructure became better mixed, and thus more homogeneous, for the annealed powders that were milled for longer times (Figures 5.10b and 5.10c), and for the powders that were milled for 12 and 48h respectively.

It is understood that the longer milling times had improved the homogeneity of the milled powders and enhanced the kinetics of atoms diffusion during annealing. The morphology of the W-rich phase (bright contrast) and its coherent interfaces with the Ti-rich particles suggests that the W-Fe-Cr phase formed had a melting temperature lower than 1480˚C. A liquid phase rich in W was formed during the annealing, and it acted as binder of the solid Ti-rich particles.

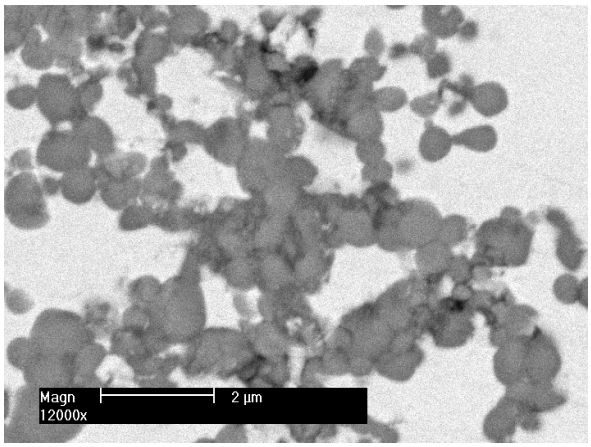

5.10a. as-mixed (not milled) powders annealed at 1480˚C.

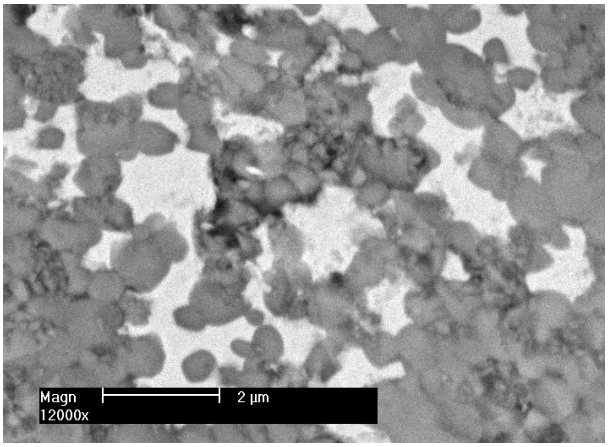

5.10b. milled for 12h and annealed at 1480˚C.

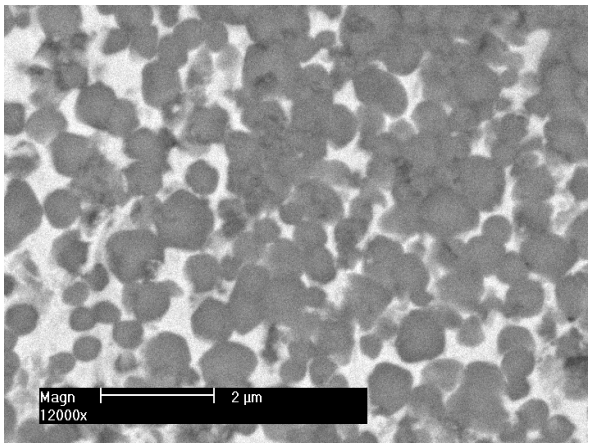

5.10c. milled for 48h and annealed at 1480˚C.

Figure 5.10. BSE - SEM images illustrating the effect of milling time on the refinement and homogenization of the microstructure of the powders annealed at 1480˚C in an argon atmosphere. It shows the W-rich W-Fe-Cr phase (bright contrast) and the Ti-rich mechanically alloyed particles (dark).

Contaminant iron and chromium preferably alloyed with tungsten and formed lower melting intermetallic phase. Contamination by steel constituents from the milling balls may therefore have a detrimental effect on the development of single phase binders. Iron and chromium contamination would enhance a partial thermal decomposition of metastable Ti(W,C,N) formed during milling.

The particles that were cold welded during the high energy ball milling of the powder mixtures evolved into hard plate-like particles during annealing at 1480˚C. Their annealed microstructure typically consisted of a phase containing titanium and tungsten in the atomic ratio 3Ti : 1W. Elongated W-rich particles of hard metallic compounds were formed as shown in Figure 5.11. The network of elongated W-rich particles was better distributed in the matrix of powder products that were milled for 48h and annealed (Figure 5.11b) than in those milled for 12h before annealing (Figure 5.11a). Therefore, the milling time of the Ti($C_{0.5}N_{0.05}$)-40wt% W powders had a significant effect on the microstructures of the annealed products. The plates formed in the powders milled for 48h and annealed at 1480˚C were larger than those formed in the powder particles milled for 12h, which was ascribed to cold welding of the particles milled for longer times and the grain growth during annealing.

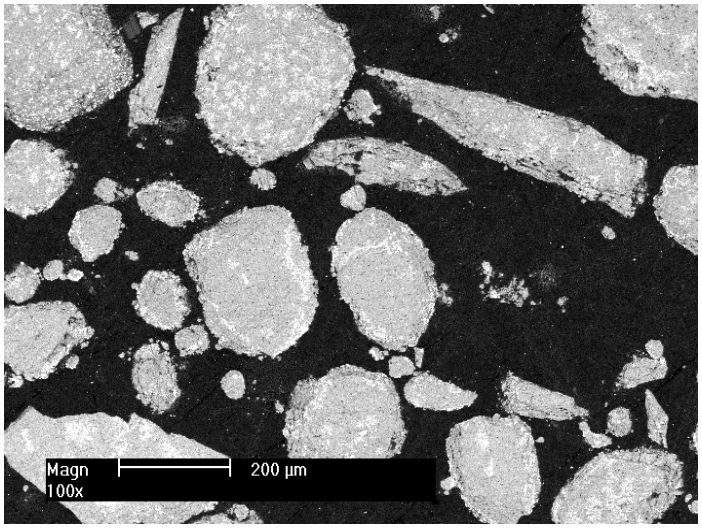

5.11a. cold welded particles milled for 12h and annealed.

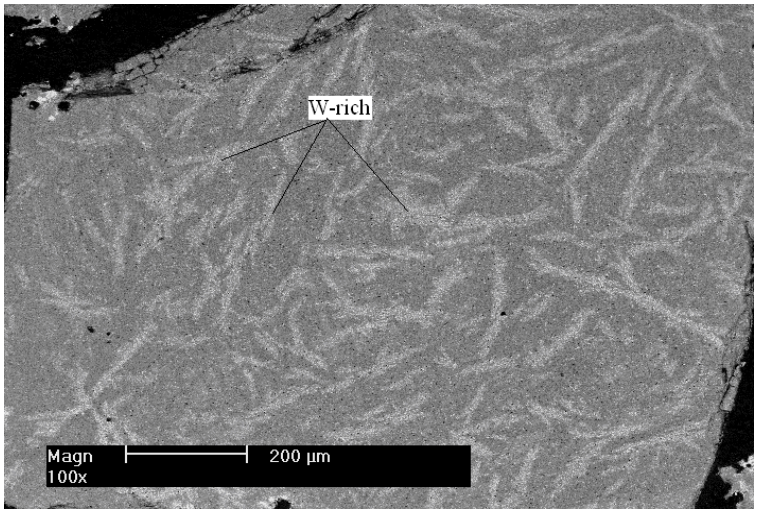

5.11b. Cold welded particles milled for 48h and annealed.

Figure 5.11. BSE - SEM images of cold welded particles annealed at 1480˚C showing large particle containing W-rich elongated particles formed in the Ti-rich matrix.

5.4. Annealing behaviour of milled $Ti(C_{0.5}N_{0.5})_{0.6}$ - 40 wt% W powders

The effect of milling time on the DTA heating curves of powders of the second system is illustrated in Figure 5.12. The heating curves showed that the constituents of $Ti(C_{0.5}N_{0.5})_{0.6}$ – 40 wt% W milled powders transformed in the temperature range extending between 600˚C and 1250˚C, which was about 200˚C lower than the transformation range of $Ti(C_{0.5}N_{0.05})$ - 40 wt% W milled mixtures. It had been observed, in Chapter 4, that the kinetics of dissolution of W in $Ti(C_{0.5}N_{0.05})$ particles was faster than in $Ti(C_{0.5}N_{0.5})_{0.6}$. However, it was also noticed that the lattice strains induced by high energy ball milling of $Ti(C_{0.5}N_{0.5})_{0.6}$ were higher than those developed in milled $Ti(C_{0.5}N_{0.05})$ powder particles as shown in Figure 5.13. As milling was prolonged the subsequent strain relaxation was smaller. Thus the residual lattice strains of milled

$Ti(C_{0.5}N_{0.5})_{0.6}$ - 40wt% W mixtures were higher, and the mechanical alloy was far from stability.

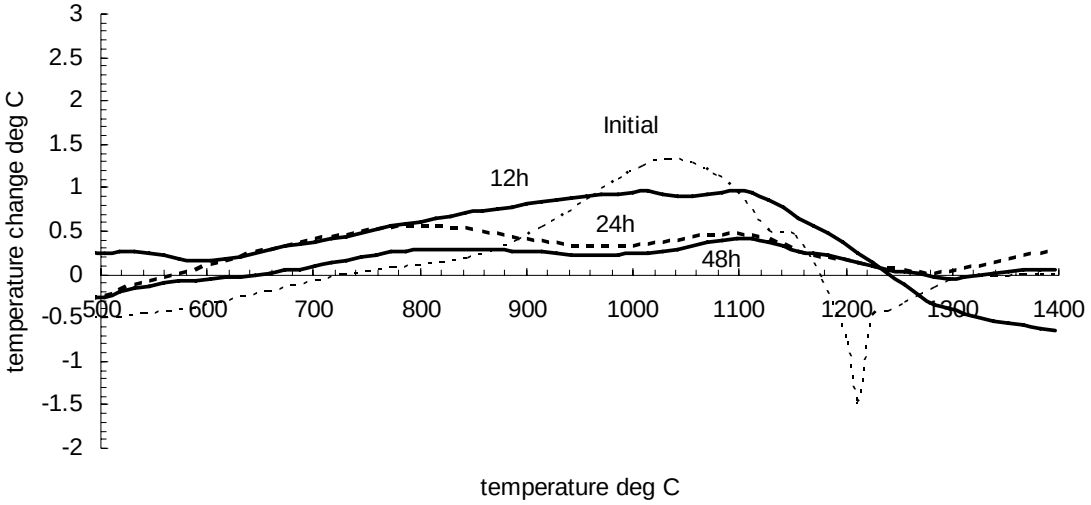

Figure 5.12. Heating curves of $Ti(C_{0.5}N_{0.5})_{0.6}$ - 40 wt% W powder mixtures processed by high energy ball mill for 12h, 24 and 48h showing a decrease in temperature change as the milling time increased.

The lower reaction start and finish temperatures observed upon heating of milled $Ti(C_{0.5}N_{0.5})_{0.6}$ - 40 wt% W powders were therefore ascribed to the metastable state of the starting material. The residual lattice strain energy in milled $Ti(C_{0.5}N_{0.5})_{0.6}$ - 40 wt% W mixtures was subsequently released upon heating to lower temperatures than was needed for the thermal transformation of the milled $Ti(C_{0.5}N_{0.05})$ - W mixtures. The faster kinetics of dissolution in the $Ti(C_{0.5}N_{0.05})$ - W system was ascribed to the release of the lattice strain energy stored in $Ti(C_{0.5}N_{0.05})$ crystals, which contributed to the driving force for mechanical alloying. The magnitude of energy release during ball milling was significant and occurred earlier for $Ti(C_{0.5}N_{0.05})$ based systems than in those containing $Ti(C_{0.5}N_{0.5})_{0.6}$.

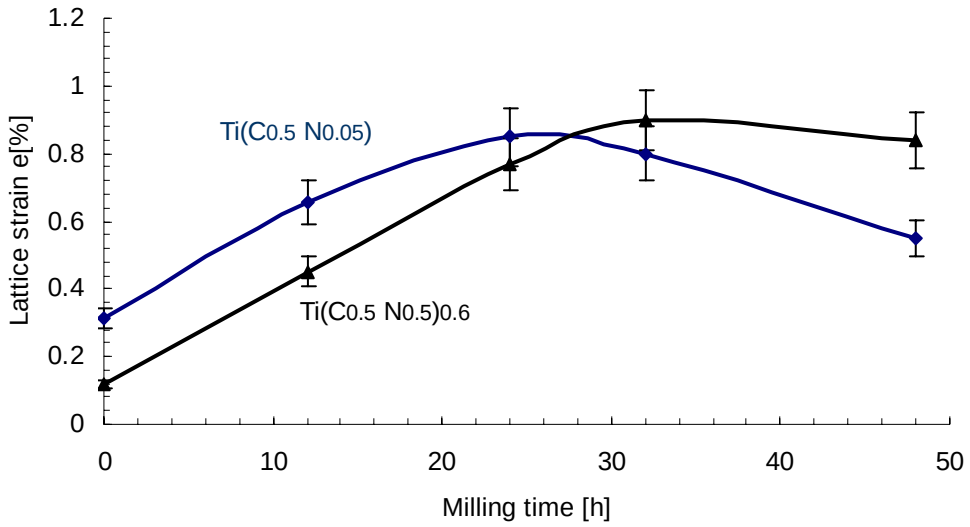

Figure 5.13. Calculated crystal lattice strains of $Ti(C_{0.5}N_{0.05})$ and $Ti(C_{0.5}N_{0.5})_{0.6}$ matrices powder milled with W.

The DTA curves in Figures 5.1 and 5.12 also suggest different thermally induced transformations upon heating the powder mixtures of the two systems. The maximum temperature change during the heating of $Ti(C_{0.5}N_{0.5})_{0.6}$ - 40 wt% W milled powders in the DTA machine decreased from +0.9˚C to +0.4˚C as the milling time increased from 12h to 48h, whereas an opposite trend was observed for the $Ti(C_{0.5}N_{0.05})$ - 40wt% W milled powders.

XRD and SEM analyses were subsequently conducted on samples of $Ti(C_{0.5}N_{0.5})_{0.6}$ - W milled powders that were annealed at 950˚C, 1050˚C,1250˚C and 1350˚C. The analyses were to determine the products formed at these temperatures, which were hypothesized to be different from those formed upon annealing of the milled $Ti(C_{0.5}N_{0.05})$ - W powders.

The XRD patterns (Figure 5.14) showed that the metastable solid solution (6) formed by high energy milling of $Ti(C_{0.5}N_{0.5})_{0.6}$ - W powders was decomposed to a Ti-rich FCC phase (5) and W at 950˚C. The two phases remained stable during heating to 1250˚C. Some of the W then reacted with the contaminant Fe above 1250˚C to form the Fe_7W_6 intermetallic phase (14).

The differences between the trends of the heating curves were therefore attributed to the thermal alloying of constituents of $Ti(C_{0.5}N_{0.05})$ - W milled powders, whereas the metastable $Ti(C_{0.5}N_{0.5})_{0.6}$ - W solid solution was decomposed to its primary W and $Ti(C_{0.5}N_{0.5})_{0.6}$ constituents. The first reaction is exothermic, whereas the second is endothermic.

The stability of the metastable $Ti(C_{0.5}N_{0.5})_{0.6}$ - W solid solution increased with the milling time, therefore its decomposition required more energy. Subsequently, the maximum temperature change during heating of the milled $Ti(C_{0.5}N_{0.5})_{0.6}$ - W powders in the DTA machine decreased. The SEM microstructures (Figure 5.15) also showed a homogeneous microstructure of the $Ti(C_{0.5}N_{0.5})_{0.6}$ - W powder milled for 48h, whereas decomposition-precipitation of submicron W-rich particles from the matrix was observed in products annealed at 1350˚C.

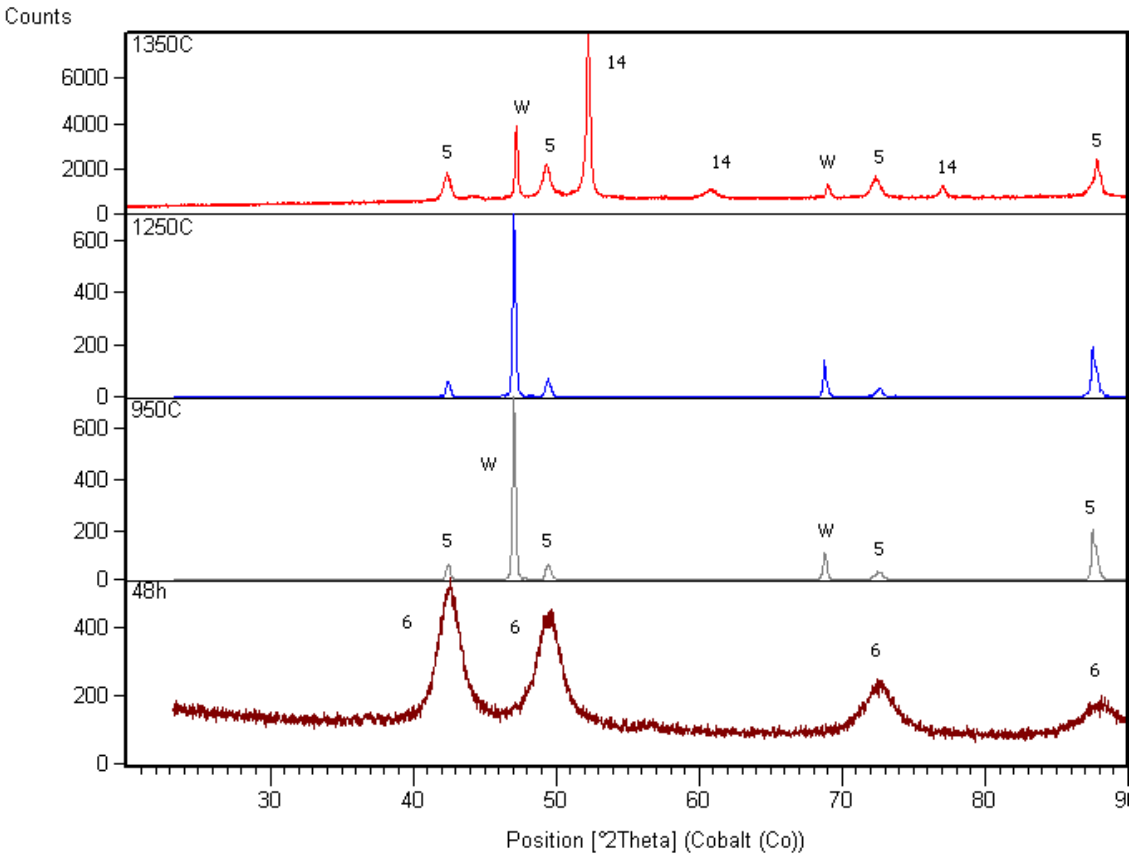

Figure 5.14. X-ray diffraction patterns of $Ti(C_{0.5}N_{0.5})_{0.6}$ - W powder mixtures milled for 48h, and annealed at different temperatures showing the peaks of the mechanically alloyed phase (6) and the decomposed mixtures containing W, the Ti-rich phase (5) and the BCC Fe_7W_6 intermetallic phase (14) formed at elevated temperature.

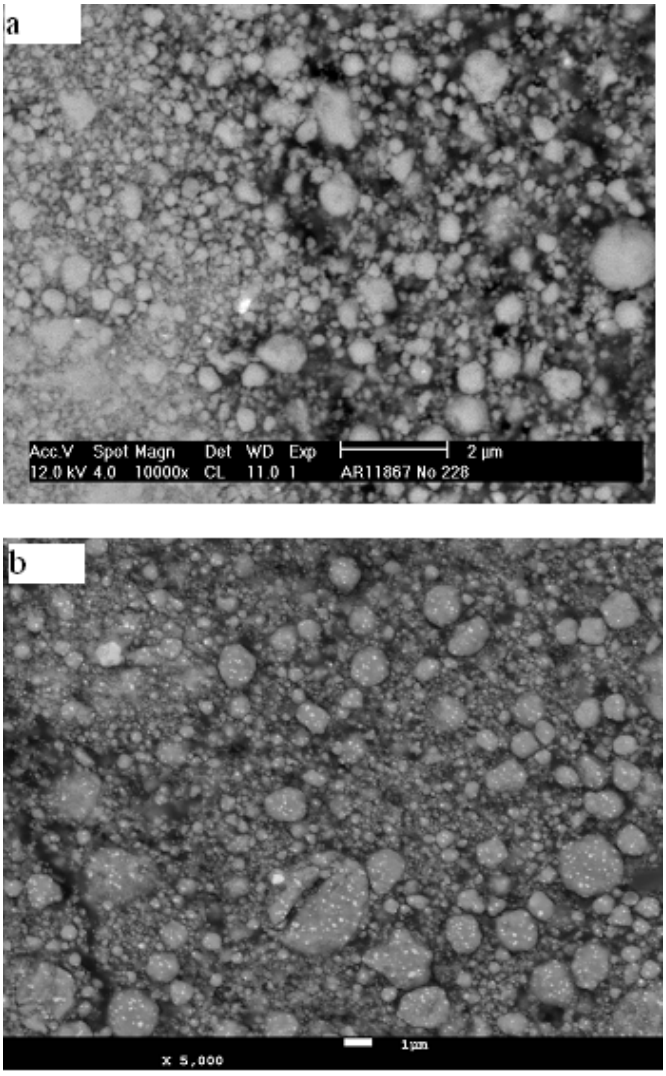

Figure 5.15. BSE - SEM micrographs of $Ti(C_{0.5}N_{0.5})_{0.6}$ - W powder showing (a) the homogeneous particles milled for 48h and (b) the decomposition of the solid solution and precipitation of fine W-rich particles (bright contrast) in the $Ti(C_{0.5}N_{0.5})_{0.6}$ particles annealed at 1350˚C.

5.5. Effect of Al on the phase formation in annealed Ti(C,N) - W alloy powders

5.5.1. Aluminium added at the annealing stage of Ti(C,N) - W mechanically alloyed powders

Aluminium powder is commonly added to Ti(C,N) binders to enhance liquid phase sintering and the formation of strong bonding with PcBN particles by controlled dissolution between the components of the sintered materials. Two different procedures were applied in this work for Al addition into the binder phase. The first method was close to the current industrial practice, where Al powder was added in 10wt% proportion to the binder powder. Thus, Al was added to the mechanically alloyed $Ti(C_{0.5}N_{0.05})$ - W powders milled for 12h, 24h or 48h as described in Chapter 4. Mixing-homogenization was then achieved by attrition milling for five hours in liquid hexane. The slurry obtained was dried, and then pre-reacted at 1050˚C or 1400˚C for ten hours to dissolve Al in the binder materials.

The XRD peaks of the pre-reacted mixtures (Figure 5.16) indicate the formation of an $fm\bar{3}m$ FCC matrix (15) product of dissolution of W and Al atoms in the Ti(C,N) lattices. Limited amounts of Al, Fe and Ti reacted with undissolved W in the milled powder to form the ordered FCC W(Al,Fe,Ti) compound (16) at 1050˚C. A product of dissolution of W and Ti in Al (17) was also formed at the same temperature. The XRD peaks of W(Al,Fe,Ti) vanished, whereas those of Al(Ti,W) decreased in proportion after annealing

at 1400˚C. The disappearance of W(Al,Fe,Ti) peaks was attributed to the dissolution of phases (16) in the matrix (15).

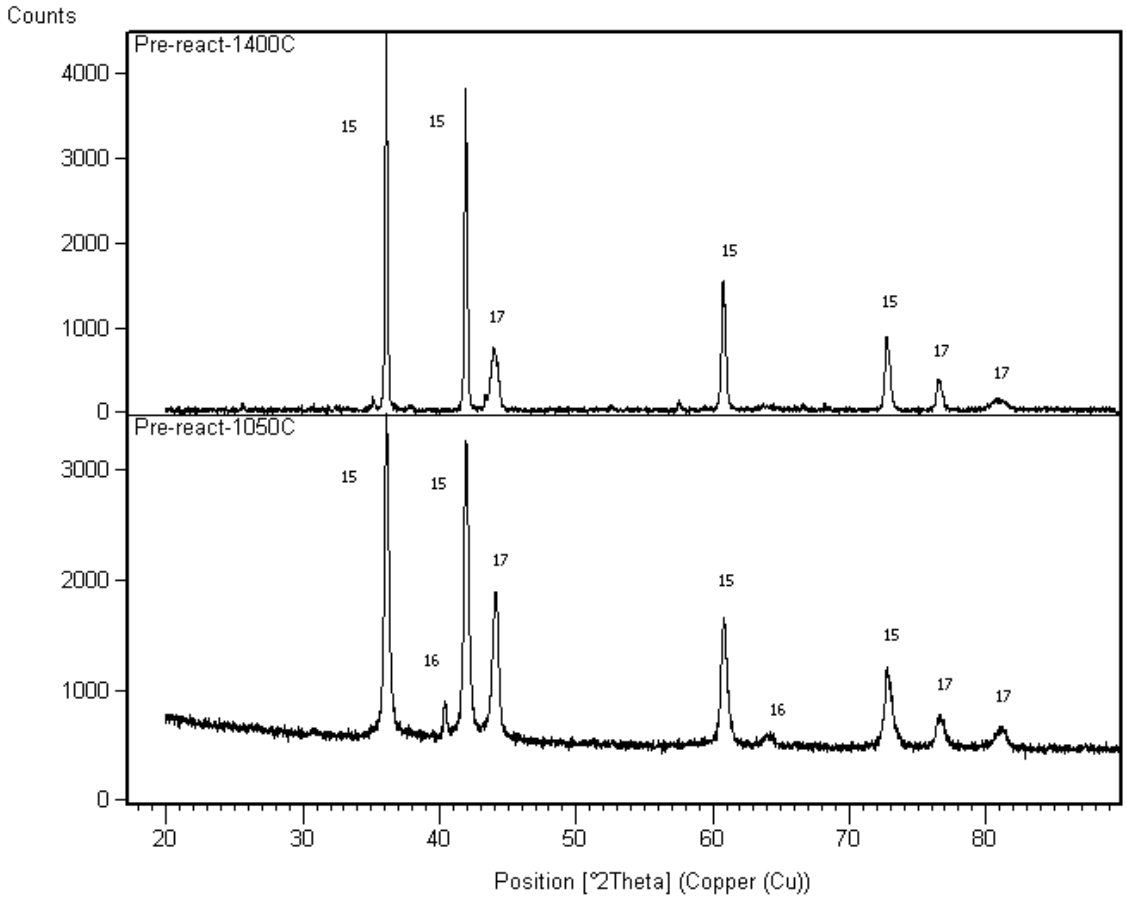

Figure 5.16. XRD peaks of $Ti(C_{0.5}N_{0.05})$ – W milled for 48h mixed with Al by attrition milling and pre – reacted at 1050˚C and 1400˚C, showing the formation of the FCC Ti(W,Al) matrix (15), the FCC W(Al,Fe,Ti) phase (16) and Al(Ti,W) compound (17).

Crystals of compound (16) had large polygonal sections (Figure 5.17), whereas compound (17) contained elongated needles that grew along their longitudinal axis (Figure 5.18). These phases melted at 1400˚C and cemented the particles of mechanically alloyed $Ti(C_{0.5}N_{0.05})$ - W (Figure 5.19).

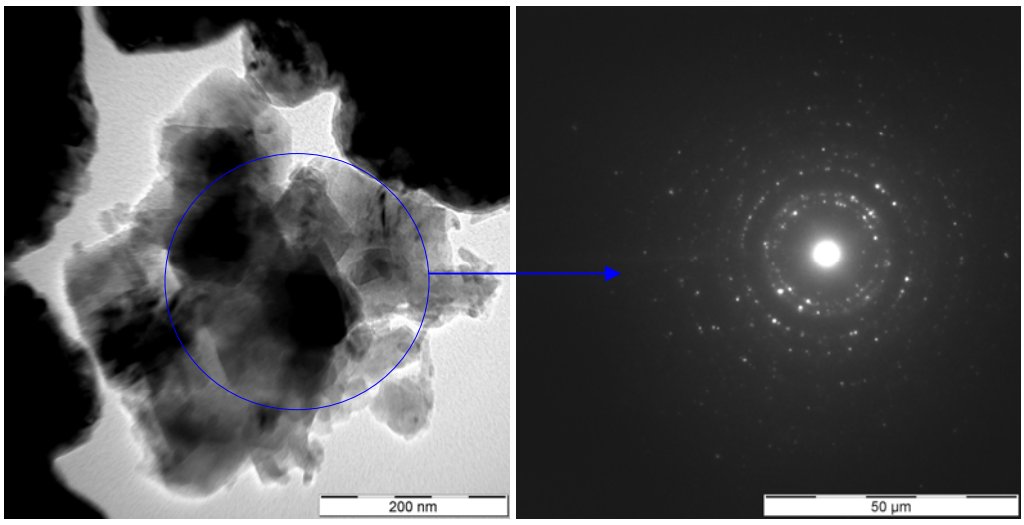

Figure 5.17. TEM micrograph showing agglomerates of prismatic crystals of the FCC W(Al,Fe,Ti) phase (16) formed at 1050˚C and the corresponding SADP.

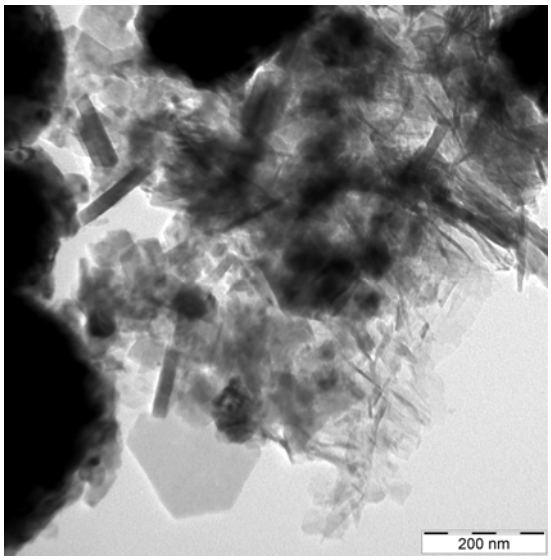

Figure 5.18. TEM micrograph showing agglomerates of crystals of Al(Ti,W) compound (17) formed at 1050˚C.

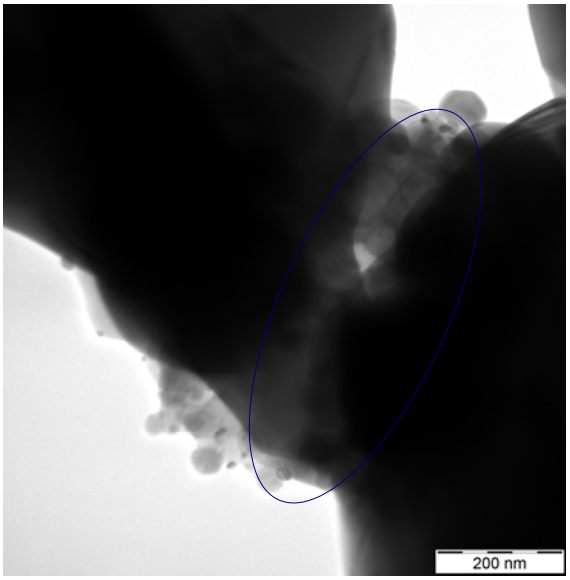

Figure 5.19. TEM micrograph showing bonding between mechanically alloyed $Ti(C_{0.5}N_{0.05})$ - W particles milled for 48h and pre-reacted with Al at 1400˚C in an argon atmosphere.

Scanning electron microscopy of the cross sections of the annealed powder particles showed that pre-reaction with Al at 1400˚C produced a homogeneous matrix (Figure 5.20). The EDX analysis indicate that the dark phase (17) contained oxygen, thus Al(Ti,W) formed at 1050˚C has reacted with the oxygen dissolved in the powders during ball milling, or oxygen adsorbed on the particles surfaces during the manipulation out of the glove box. The persistence of the corresponding XRD peaks in the high temperature product was therefore attributed to the non-solubility of the oxidised form of the phase (17) in the matrix (15). It therefore reasoned that the FCC W(Al,Fe,Ti) product (16) formed in the same conditions did not react with oxygen, thus the atom bonding has been broken and dissolved in the matrix (15) at 1400˚C, which corresponds to its disappearance from the XRD pattern.

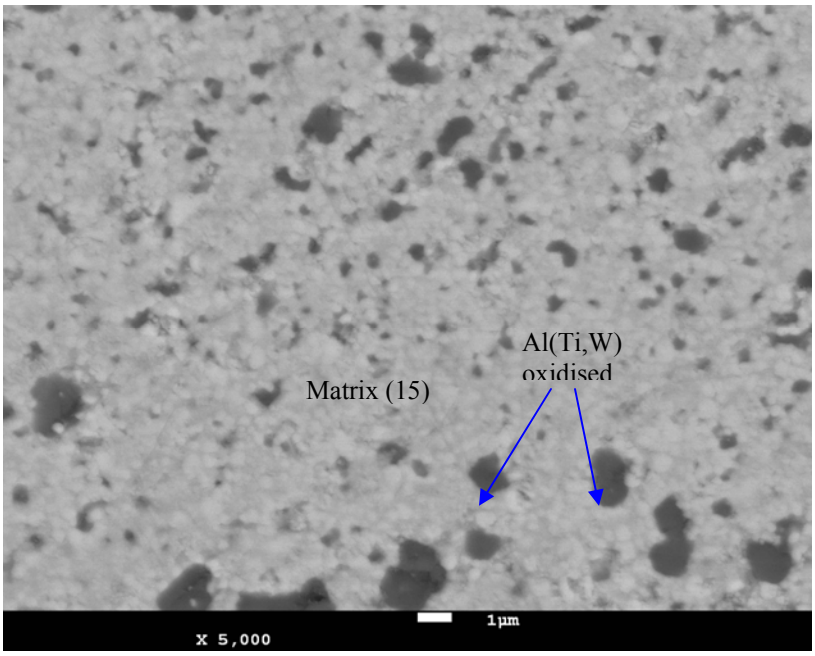

Figure 5.20. BSE - SEM micrograph of sample cross section, showing the particles of the matrix product (15) and the oxidised phase (17) formed in mechanically alloyed $Ti(C_{0.5}N_{0.05})$ - W powders pre-reacted with Al at 1400˚C.

5.5.2. Aluminium added at the mechanical alloying stage of Ti(C,N) - W - Al powder mixtures

In the second method, Al, $Ti(C_{0.5}N_{0.05})$ and W were mechanically alloyed in a planetary high energy ball mill to form a solid solution with three metals. The milled powders were then annealed at 1400˚C for one hour. It was hypothesized that the kinetics of reaction and the homogeneity of the binder phase would be enhanced by this method, which would also have the advantage of a reduced number of processing stages, thus reducing the risk of oxidation, combustion and burning during powder preparation.

The XRD analysis showed that the matrix consisted of the solid solution Ti(W,Al) (15). Some proportion of W and Ti has been dissolved in Al to form the phase (17), as was observed in the first method. However, the FCC W(Al,Fe,Ti) compound formed has not been dissolved in the matrix of the product annealed at 1400˚C.

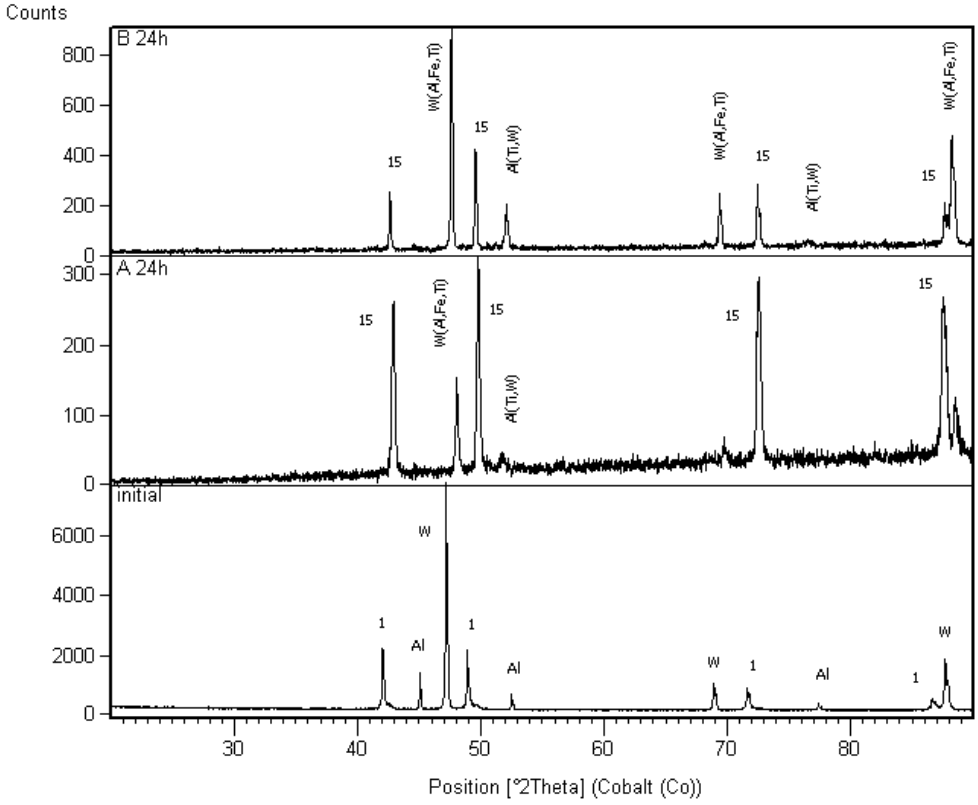

Figure 5.21. XRD peaks of (a) $Ti(C_{0.5}N_{0.05})$ - W - Al and (b) $Ti(C_{0.5}N_{0.5})_{0.5}$ - W - Al mechanically alloyed powders annealed at 1400˚C for 1h and the initial (not milled – not annealed) mixtures.

The diffraction 2θ angles of W(Al,Fe,Ti) (16) formed in milled and annealed $Ti(C_{0.5}N_{0.5})_{0.6}$ - W - Al powders were closer to pure W, which was attributed to the low solubility between Ti(W,Al) and the W(Al,Fe,Ti) formed during milling and to the limited dissolution of Al, Fe and Ti in W. The EDX analysis of the phases formed after

annealing at 1400˚C of $Ti(C_{0.5}N_{0.5})_{0.6}$ - W - Al milled powders confirmed the phases (Figure 5.22) with compositions indicated in Table 5.1.

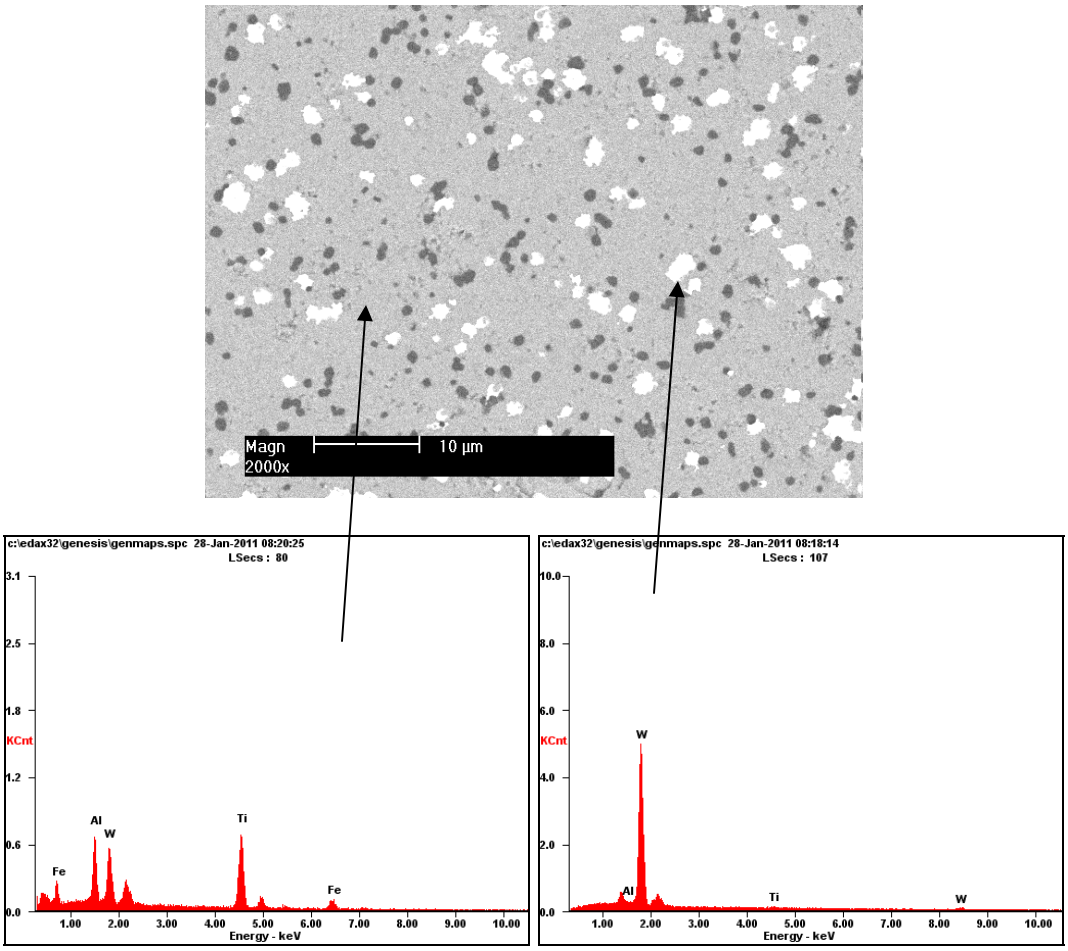

Figure 5.22. BSE-SEM micrograph showing the matrix Ti(Al,Fe,W), the W-rich particles of phase (16) and the dark particles of the phase (17).

Table 5.1. Compositions (EDS) of the phases formed in milled and annealed powders. Matrix (A) and (B) correspond to $Ti(C_{0.5}N_{0.05})$-W-Al and $Ti(C_{0.5}N_{0.5})_{0.6}$-W-Al systems respectively.

	Element composition [at.%]			
	Ti	**W**	**Al**	**Fe**
Matrix (A)	56	19	16	9
Matrix (B)	55	10	18	17
W(Al,Fe,Ti) (16)	2	94	1	3
Al(Ti,W,Fe) (17)	22	8	69	1

More W was dissolved in matrix A than in matrix B, whereas iron content was higher in matrix B than in matrix A. However, the sum total of tungsten and iron contents in the two matrices were practically equal. It was also observed in Section 4.1 (Figure 4.10) that iron and tungsten were present in the rim part of milled powder particles. It is inferred from these observations that tungsten and contaminant iron atoms would compete to occupy substitution positions in Ti(C,N) structures. The effect of iron contamination is discussed in Section 5.3 (page 114). Milling of Ti(C,N) alone at low rotation speed may reduce the contamination by protective forming layers on the surfaces of stainless steel balls and jars.

The microstructure of milled and annealed $Ti(C_{0.5}N_{0.05})$-W-Al (Figure 5.23) mainly consisted of Al(Ti,W,Fe) particles dispersed in the Ti(W,Al,Fe) matrix, whose W content was double that dissolved in the annealed $Ti(C_{0.5}N_{0.5})_{0.6}$-W-Al. The Higher solubility of W in $Ti(C_{0.5}N_{0.05})$ was noticed during milling (Chapter 4). It was also observed that thermal dissolution of W-rich phases occurred during annealing, whereas the metastable

solid solution of $Ti(C_{0.5}N_{0.5})_{0.6}$ - W were decomposed and W-rich phases were formed during annealing.

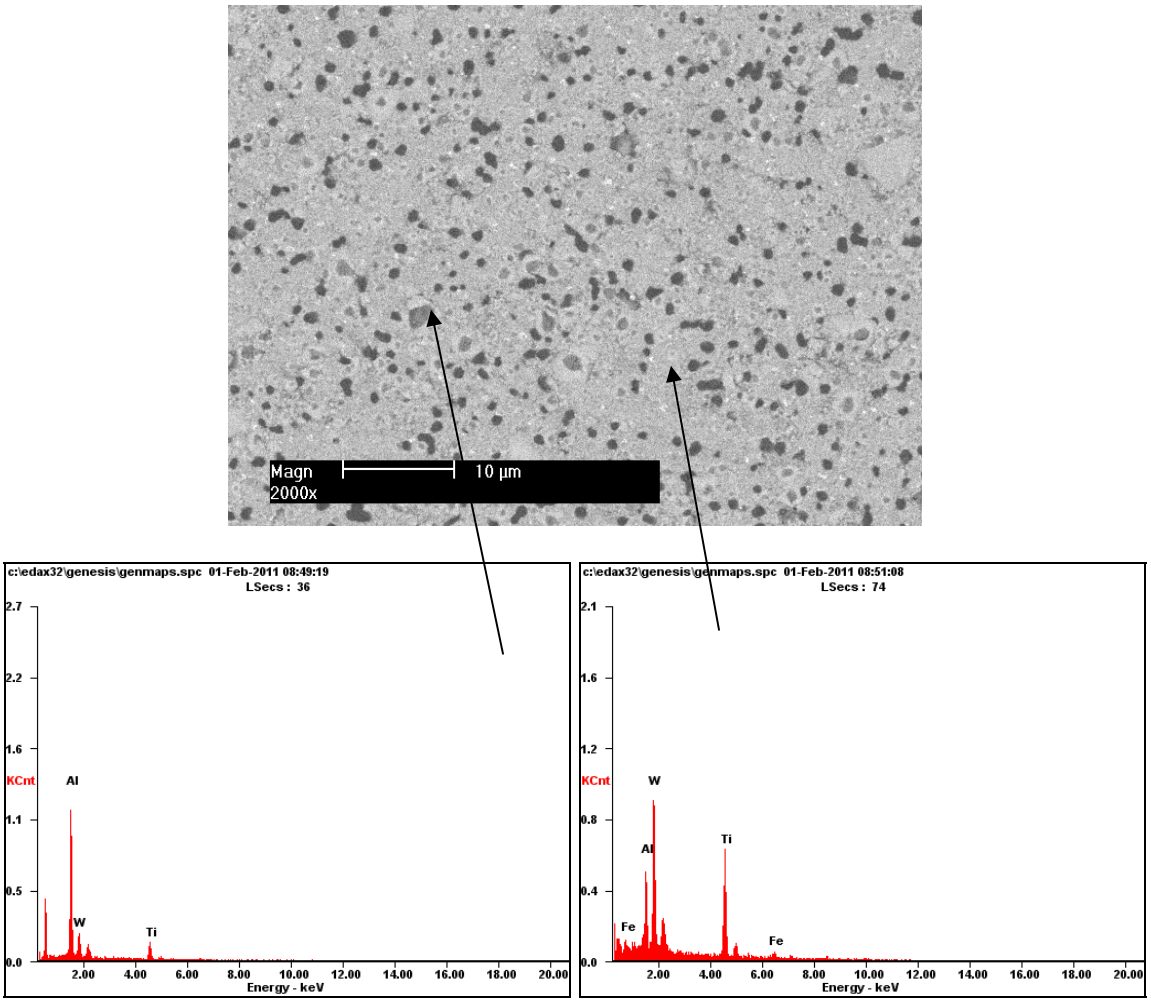

Figure 5.23. BSE - SEM micrograph showing the matrix Ti(Al,Fe,W) and the the dark particles of the Al(Ti,W,Fe) phase (17).

CHAPTER 6. POLYCRYSTALLINE CUBIC BORON NITRIDE SINTERING WITH Ti(C,N) - *x* W - *y* Al MECHANICALLY ALLOYED BINDERS

6.1. Material preparation

The 55wt% Ti(C,N) - 35wt% W - 10wt% Al binder mixtures were prepared following two procedures using $Ti(C_{0.5}N_{0.05})$ or $Ti(C_{0.5}N_{0.5})_{0.6}$, i.e.:

a) Two constituents Ti(C,N) and W powder mixtures were processed by high energy milling for 12h, 24h and 48h in a Retch planetary ball mill, PM400 MA-type. The milled products were then mixed with Al powder and boron nitride by attrition milling in liquid hexane for five hours to achieve a low cBN mixture containing 60wt% cBN with 40wt% of binder. The slurries were dried at 70˚C and out-gassed at a 1050˚C under 10^{-4} mbar vacuum for eight hours.

b) Alternatively, the mixtures of the three constituent powders, Ti(C,N), W and Al, were processed by the Retch equipment. This process aimed to form solid solutions at relatively low temperature before mixing with the boron nitride powder. The alloyed powders were also added into boron nitride powder and homogenized by attrition milling.

The cBN mixtures were sintered on WC-8% Co substrates in a HPHT system under 5GPa at 1400˚C. The transformations were investigated using XRD, SEM and TEM techniques. The effect of the applied pressure on the occurring transformations was also investigated by XRD analysis of milled powder mixtures heated under 10^{-4} mbar, 1bar and 50000 bars

(5GPa) respectively. High temperature XRD conducted under vacuum at different temperatures between 25˚C and 1200˚C using a Philips Analytical X-Ray B.V. X-Pert diffractometer machine, equipped with a hot stage, allowed the determination of the transformation temperatures of the compounds formed as temperature increased. The results of these investigations are discussed in the next sections.

6.2. Structure and microstructure of PcBN sintered with binders prepared using Ti(C,N) - W mechanically alloyed powders mixed with Al by attrition milling

The XRD diffractograms of the cBN mixtures with $Ti(C_{0.5}N_{0.05})$ - W powders milled for 12h and 48h (Figures 6.1. a1 and b1) and with $Ti(C_{0.5}N_{0.5})_{0.6}$ - W powder milled for 48h (Figure 6.c1) annealed for 1h at 1050˚C under an argon atmosphere and those of the corresponding HPHT sintered products (Figures 6.1.b2 and c2) contained no Al peaks. The absence of Al peaks was ascribed to the fast diffusion and alloying of Al atoms with Ti and W at high temperature. The proportion of W not dissolved in $Ti(C_{0.5}N_{0.05})$ after milling the mixtures for 12h remained stable and did not react with Al or cBN annealed at 1050˚C under an argon atmosphere (Figure 6.1.a1). However, it was observed that the constituents of the powders milled for 48h had completely alloyed with Al and formed an FCC (σ) product (Figure 6.1.b1).

Peaks of a HCP (ω) phase of composition $WC_{0.9}$ were also perceptible, more in mixtures prepared using $Ti(C_{0.5}N_{0.5})_{0.6}$ than in those made using $Ti(C_{0.5}N_{0.05})$ powders, which were ascribed to the reaction between C from the Ti(C,N) and the non-dissolved W that was

activated by straining during milling or with the particles formed by thermal decomposition of the mechanical alloys.

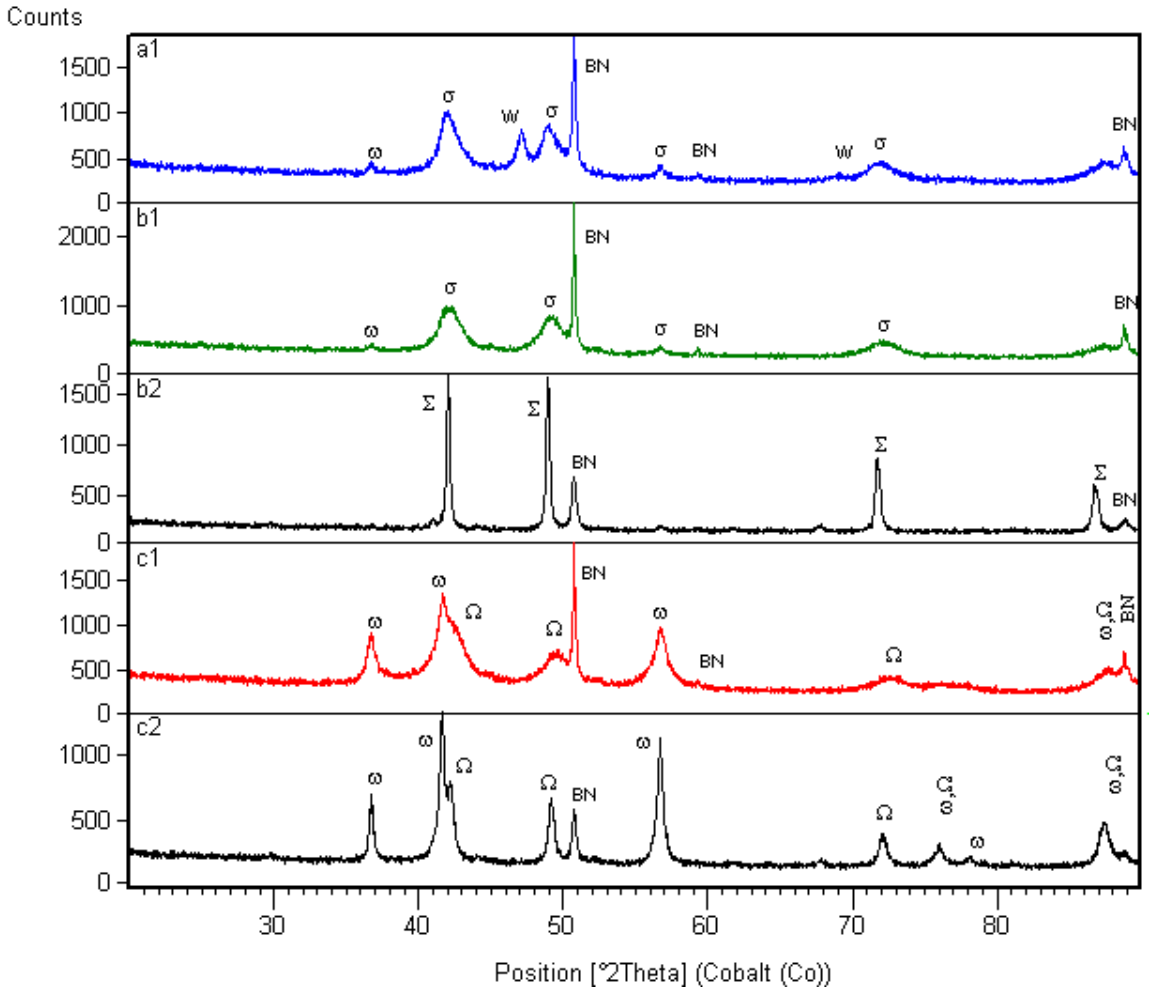

Figure 6.1. XRD peaks of the mixtures of cBN with $Ti(C_{0.5}N_{0.05})$ - W powders milled for 12h and 48h (a1 and b1) and mixed with $Ti(C_{0.5}N_{0.5})_{0.6}$ - W milled for 48h (c1) mixed with Al. Peaks of the corresponding HPHT sintered PcBN products (b2 for a1 and a2) and (c2) for (c1) showing the characteristic peaks of the FCC phase (σ), the HCP (ω) of composition $WC_{0.9}$, the HPHT sintered binders (Σ) and (Ω) formed.

The proportion of non-dissolved W after milling for 12h remained stable after mixing with cBN and Al as one characteristic peak was still perceptible in the X-ray pattern (Figure 6.a1).

The products of sintering PcBN with the mechanically alloyed $Ti(C_{0.5}N_{0.05})$ - W mixed with Al contained a FCC (Σ) binder phase. The W and $WC_{0.9}$ peaks observed in the non-sintered mixtures (Figure 6.1.a1) had disappeared subsequently to their dissolution in the FCC (σ) material, which transformed into the final binder product (Σ) under the high pressure and temperature.

The lattice strains calculated by means of the Scherrer equations using the XRD data of the binder phases decreased from 0.267% in the non-sintered material (σ) to 0.177% in the HPHT sintered phase (Σ). The relaxation of the lattice strain was attributed to the thermal dissolution in the phase (σ) of the atoms of the strained W crystals that were not alloyed during the ball milling processing of the $Ti(C_{0.5}N_{0.05})$ - W mixtures. The corresponding crystallite sizes of the binder increased from 11nm to 121nm.

On the other hand, the lattice strain in the PcBN phase increased from 0.050% in the starting mixture to 0.176% in the sintered product. The crystallite size was refined from 278±30 nm to 27±3 nm upon sintering. Thus, the high pressure and temperature applied during sintering have induced opposite structural effects in the binder phase than in the PcBN.

The XRD peaks of the mixtures of BN with the mechanically alloyed $Ti(C_{0.5}N_{0.5})_{0.6}$ - W powders milled for 48h and doped with Al by attrition milling (Figure 6.1.c1) indicate the formation of two phases, the HCP $WC_{0.9}$ phase (ω) and a cubic phase (Ω) that had a

structure close to $TiAl_{0.11}(C_{0.38}N_{0.35})$ [200], in the binder material of the sintered PcBN (Figure 6.1.c2).

The cubic phase (Ω) had formed already in the non sintered mixtures (Figure 6.1.c1). The XRD peaks of the two phases (Ω) and (ω) became sharper after HPHT sintering, showing the increased crystallite sizes and the decrease in lattice strains of the binder constituents, an effect similar to that observed in the single phase binder (Σ) formed in the system sintered using mechanically alloyed $Ti(C_{0.5}N_{0.05})$ - W mixed with Al powders.

The calculated lattice strains and crystallite sizes of the phases present before and after sintering of cBN with $Ti(C_{0.5}N_{0.5})_{0.6}$ - W are given in Tables 6.1 and 6.2, where it was noticed that the crystallite size of PcBN was refined as was also observed in PcBN sintered with the $Ti(C_{0.5}N_{0.05})$ - W based binders.

It was noticed that the lattice strains of the binder and the PcBN products were higher in the sinters prepared with the $Ti(C_{0.5}N_{0.5})_{0.6}$ - W binder than in those made using the $Ti(C_{0.5}N_{0.05})$ - W alloys. It can be inferred from the XRD peaks that formation of the HCP phase $WC_{0.9}$ (ω) was the cause of differences between the two binder materials. Thus, the differences in lattice strains and crystallites sizes of the sintered products were ascribed to the differences of C and N contents of the Ti(C,N) and the milling parameters, which determined the dissolution rates of W, hence the residual strains, generated in the sintered PcBN particles. The higher dissolution rate of W in Ti(C,N) with higher contents of C and interstitial N led to lower lattice strains in the sintered products.

Table 6.1. Calculated lattice strains of the phases formed after PcBN sintering with the milled $Ti(C_{0.5}N_{0.5})_{0.6}$ - W mixed with Al powders.

Phases	**Annealed at 1050˚C** ***e* [%]**	**After HPHT sintering** ***e* [%]**
cBN	0.050	0.218
Ω	0.218	0.362
ω	0.589	0.222

Table 6.2. Calculated crystallite sizes of the phases formed after PcBN sintering with the milled $Ti(C_{0.5}N_{0.5})_{0.6}$ - W mixed with Al powders.

Phases	**Annealed at 1050˚C** ***L* [nm]**	**After HPHT sintering** ***L* [nm]**
BN	431	48
Ω	15	32
ω	14	44

The difference in microstructures between a custom low cBN PcBN sintered with a Ti(C,N) - Al attrition milled binder (Figure 6.2a) and those of three products prepared with the mechanically alloyed binders described in Section 6.1 are illustrated in Figure 6.2. The sizes of PcBN particles and the binder materials were finer in the products sintered with the mechanically alloyed binders (Figure 6.2.b, c and d) than in the custom product. Industrial practice [31] has shown that the heterogeneous microstructure due to the formation of a Ti-rich second phase in the binder of the custom PcBN

(bright spots in Figure 6.2.a) contributed to the limited performance observed of the tools used in machining of metal alloys such as cast iron and high speed-steels.
Conversely, high energy ball milling has improved the homogeneity of the mechanically alloyed binders as shown in Figure 6.2b through to d.

The $Ti(C_{0.5}N_{0.05})$ - W mixtures milled for 48h formed more homogeneous binder pools (Figure 6.2.c), whereas the particles of binder formed in MA powders milled for 12h were characterized by core/rim structures after sintering as shown in Figure 6.3. The core/rim structure was ascribed to incomplete diffusion of W atoms through the core of the particles of Ti(C,N), hence to the concentration gradient developed during milling.

The crystals in the core of the binder particles were smaller than 200nm (Figure 6.3). Transmission electron microscopy of the binder phase also showed the formation of the nanocrystals in the rim part of the binder particles where W had diffused in the Ti(C,N) particles during ball milling (Figure 6.4).

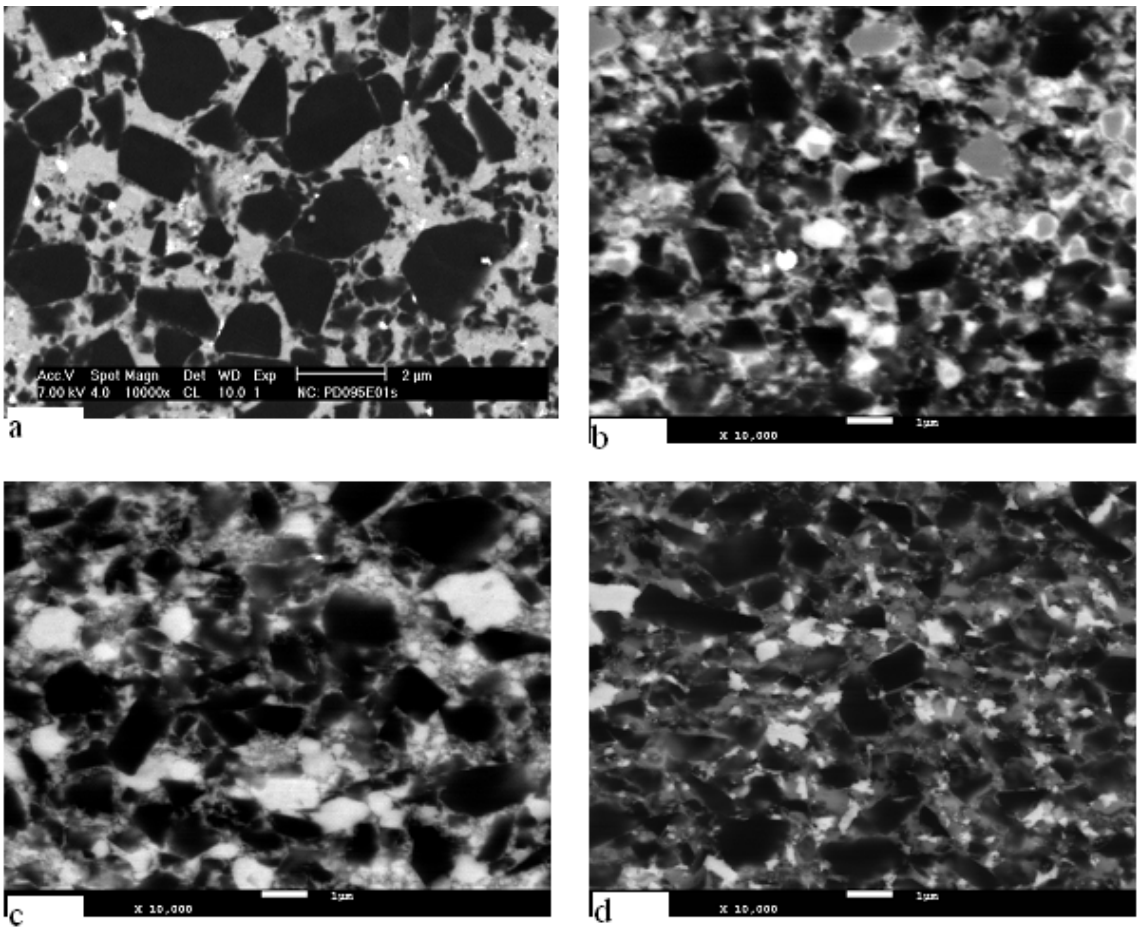

Figure 6.2. SEM - BSE images of (a) custom low cBN PcBN sintered with Ti(C,N) pre-reacted with Al, (b) and (c) PcBN sintered using $Ti(C_{0.5}N_{0.05})$ - W based binders milled for 12h and 48h respectively and mixed with Al by attrition milling, (d) sintered with $Ti(C_{0.5}N_{0.5})_{0.6}$ - W binder milled for 48h and doped with Al; showing cBN particles (dark contrast) and the binder pools (bright).

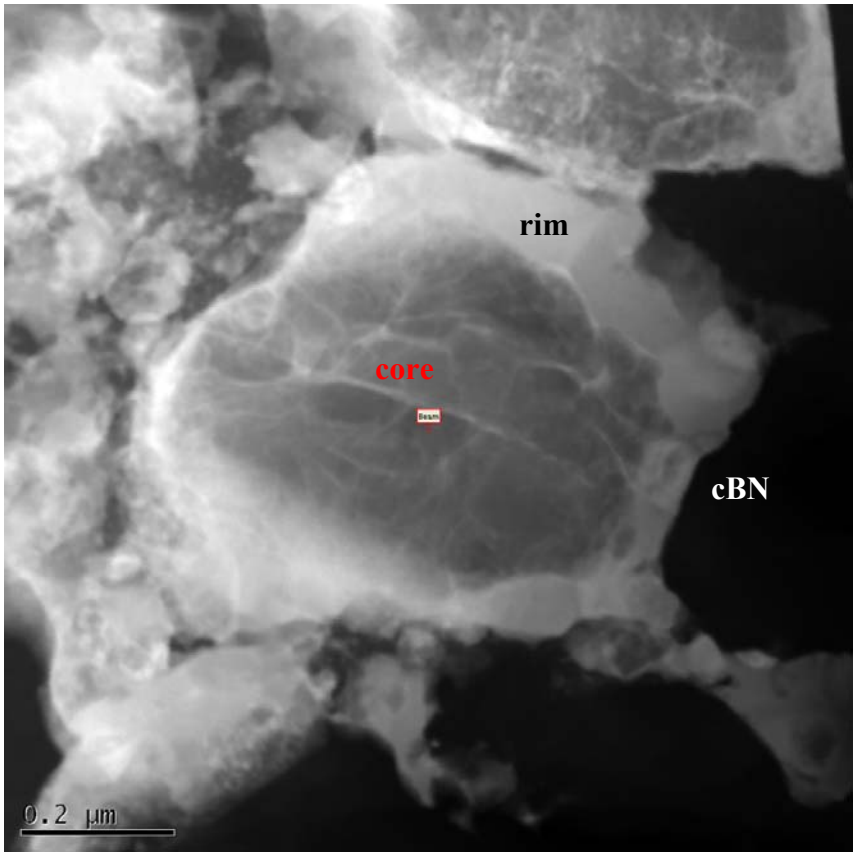

Figure 6.3. STEM - HAADF image of product sintered with $Ti(C_{0.5}N_{0.05})$ - W milled for 12h and mixed with Al showing the core-rim structure of a nanostructured binder particles.

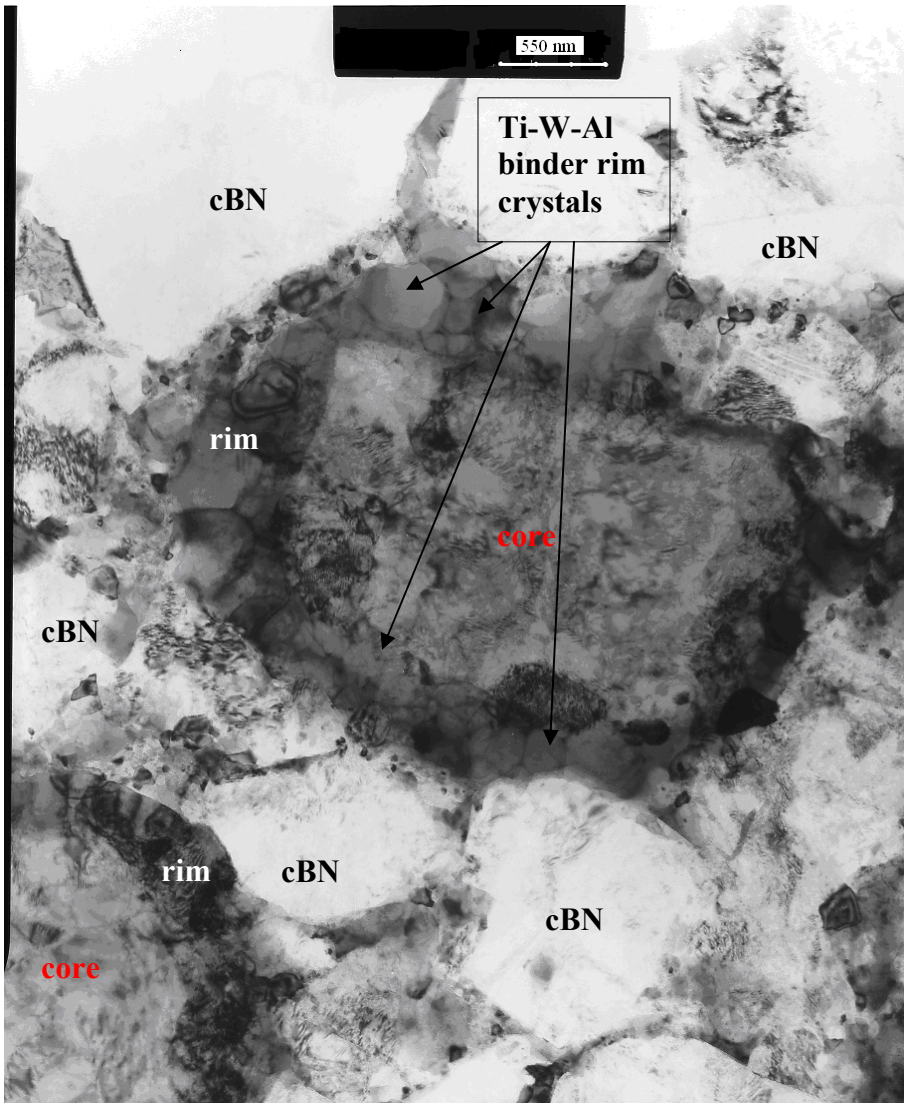

Figure 6.4. Bright field TEM image showing the formation of nanocrystals in the rim of the binder particles of Ti($C_{0.5}N_{0.05}$) - W milled for 12h and attrition mixed with Al.

The elemental mapping of the STEM-HAADF image and TEM-BF images of a mechanically alloyed Ti($C_{0.5}N_{0.05}$) binder particle surrounded by cBN (Figure 6.5) showed that W and Al atoms were dissolved, although their diffusion was limited to the rim portions of the binder particles milled for 12h. The lower density distribution of the N atoms in the rim regions was attributed to the denitriding observed at the longer milling times of the Ti(C,N) powder particles processed in an argon atmosphere as discussed

earlier in Chapter 4. The lower intensity of Ti in the rim was attributed to the dilution by dissolution and alloying of W and Al.

The traces of Fe contamination from the milling media were identified in the rims, whereas the cores of the binder particles were not affected. It also appeared that Fe was most concentrated where Al was not, which suggested that Al was substituted to the contaminant Fe in the Ti(W,Fe) rims formed during milling.

The thickness of the rims regions varied between 50 and 100nm. Thus, the thermally induced reactions between the binder constituents were limited to the rim regions inherited from the ball milling stage. The HPHT sintering process did not induce significant diffusion of W, Al or the contaminating Fe through the core of Ti(C,N) particles.

The absence of atom diffusion during sintering was attributed to the stability of the phases (σ, ω and Ω) formed during the heating of the MA Ti(C,N) - W powders. It also indicates that the mechanically alloyed powders were fairly stable at temperatures as high as the sintering temperature of ~1400˚C. The thickness of the rims in the binder particles was therefore ascribed to the ball milling parameters and the original particle size of the $Ti(C_{0.5}N_{0.05})$ and $Ti(C_{0.5}N_{0.5})_{0.6}$ powders.

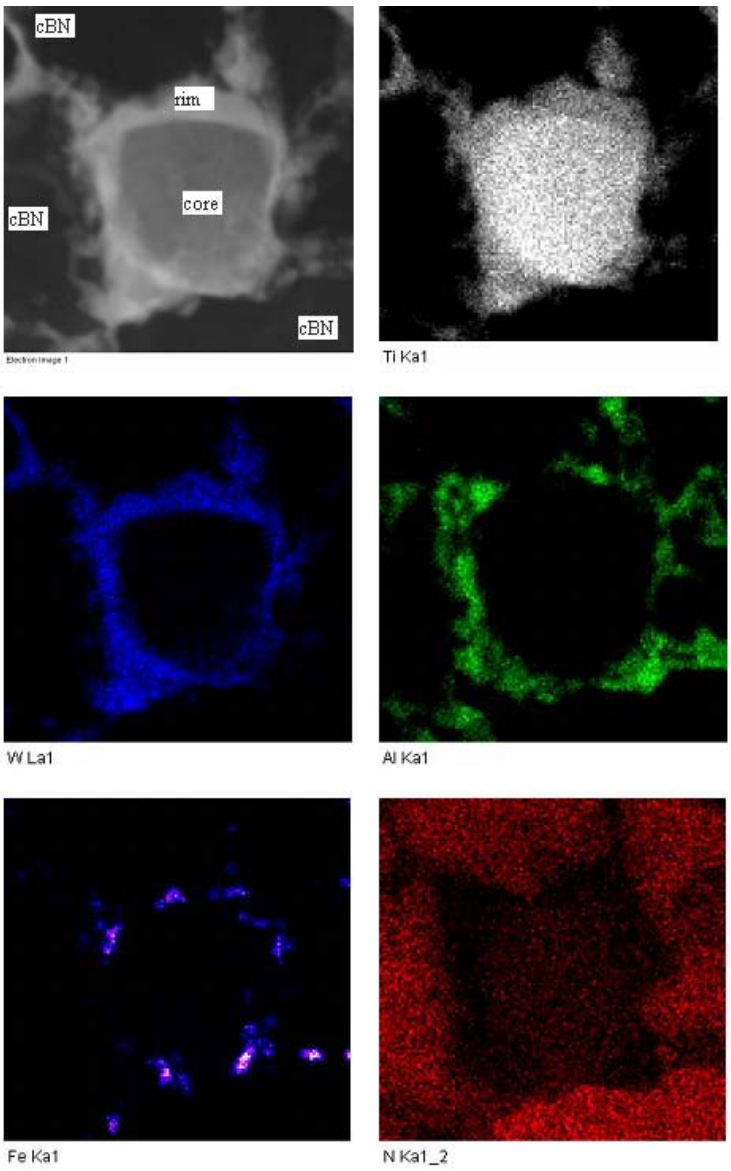

Figure 6.5. HAADF-STEM elemental maps showing the distribution of elements in the rim and core of particles PcBN sintered with $Ti(C_{0.5}N_{0.05})$-W powders milled for 12h and mixed with Al by attrition milling. Scale bar = 250 nm.

The element mapping of nitrogen (in Figure 6.5) indicated that the fine strings of binder phase located between the particles of cBN were also poorer in N than the core of the binder particles. It was therefore concluded that these particles originated from the rim materials, which were crushed and pushed in between the cBN particles during the HPHT

sintering cycle. High concentrations of aluminium and iron were found in the W-rich rim regions of the binder particles, whereas the cores remained rich in titanium. The subsistence of the core-rim structures after HPHT suggests that atom diffusion was minimal during sintering.

The crystals formed in the binder pools (Σ) of $Ti(C_{0.5}N_{0.05})$ - W milled for 12h were smaller than 200 nm (Figure 6.6.a), whereas those formed in the binders milled for 48h were sometimes coarser (Figure 6.6.b). The formation of the coarse structures was attributed to the grain growth during sintering. It was also noticed in Chapter 4 that cold welding leading to agglomeration was significant in powders milled for longer times than 24h, whereas fracturing of the particles prevailed during the shorter milling times. Thus, the particles of the binder milled for 48h became larger than those milled for 12h.

The microstructure structure of the binder pool (Ω) (Figure 6.6.c) formed during the sintering of PcBN with the $Ti(C_{0.5}N_{0.5})_{0.6}$ - a W alloyed powder was finer than 100 nm. The formation of the finer substructures in the binder pools was attributed to the finer crystallite sizes generated during the ball milling process as it was noticed in Chapter 4 that fracturing and particle size reduction by ball milling were more efficient for $Ti(C_{0.5}N_{0.5})_{0.6}$ than $Ti(C_{0.5}N_{0.05})$. Thus, the fineness of the substructures formed in the sintered binder particles was also determined by the milling parameters.

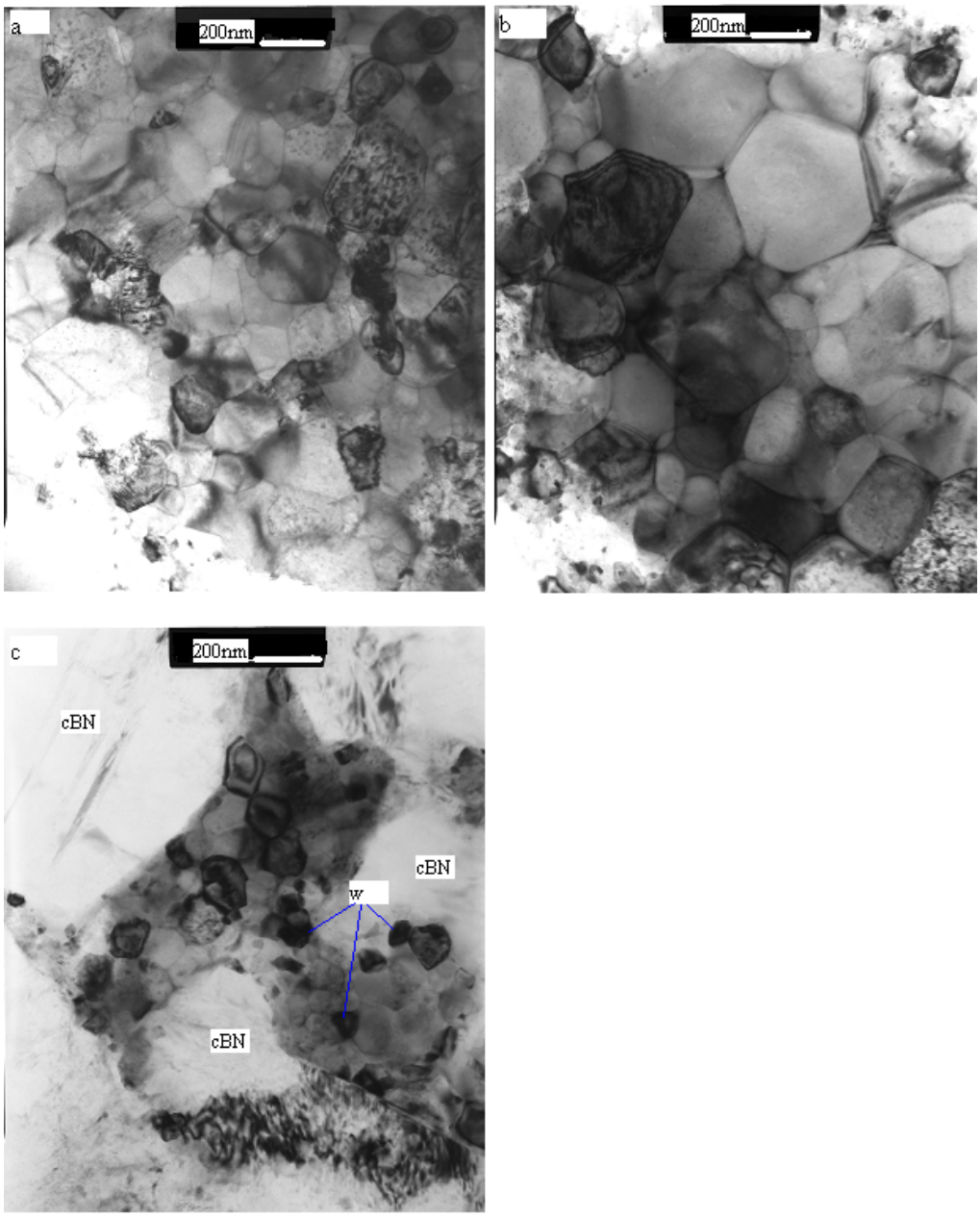

Figure 6.6. BF-TEM images showing the crystals inside the binder pools (Σ) of $Ti(C_{0.5}N_{0.05})$ - W milled for 12h and 48h respectively (a and b) and (c) those of the binder phase (Ω) in $Ti(C_{0.5}N_{0.5})_{0.6}$ - W milled for 48h mixed with Al.

6.3. Sintering mechanism

The sintering mechanism can be determined from the geometry of the binder/matrix particle interfaces. The microfaceted interfaces are formed by the mechanism of dissolution-precipitation and re-arrangement of atoms during liquid phase sintering, whereas smooth interfaces are indicative of a solid state sintering by diffusion of surface atoms [202-206]. The sharp step-like boundary features were seen in the TEM images only for samples which were carefully aligned with the <110> direction of the FCC materials lattice parallel to the electron beam [202].

The microfaceted interfaces which were observed in some regions, as shown in Figure 6.7, indicated that liquid phase sintering took place between the cBN and the binder (Σ) and also a limited solubility and interdiffusion of atoms through the cBN/binder interface. However, smooth interfaces were also observed between the surrounding particles of PcBN and the binder and between the grains of the binder themselves, which could be attributed to a change of orientation of the interface between the crystals relatively to the TEM viewing direction. The smooth interfaces could also result from the truncation of the sharp microfacets upon annealing. Jacobsen *et al.* [202] ascribed the truncation process to the relaxation of surface energies.

The formation of two types of interfaces could also be due, in this case, to the non-uniform distribution of Al and Fe in the rims of the binder particles as shown by elemental mapping (Figure 6.5), thus to the formation of Fe-rich and Fe-deficient binder pools.

The first would form a lower melting temperature phase characterized by higher mobility of atoms through the interface than the second where solid state sintering occurred.

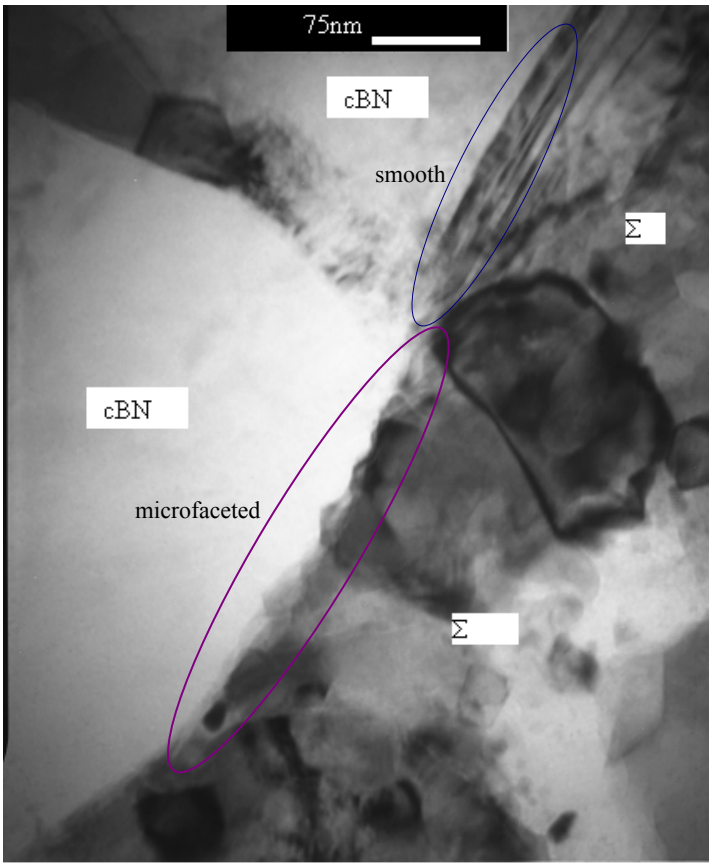

Figure 6.7. BF-TEM image of the interfaces between the cBN and the binder (Σ) particles showing a microfaceted boundary contiguous with a smooth boundary.

The HAADF-STEM analysis of the microstructures also showed that the sintered binder phases also contained crystals smaller than 50 nm, indicated by arrows, located between the cBN particles (Figure 6.8.a). It was inferred from the element mapping results (Figure 6.5) that the N distribution was comparable in these crystals and in the rims of the binder pool particles.

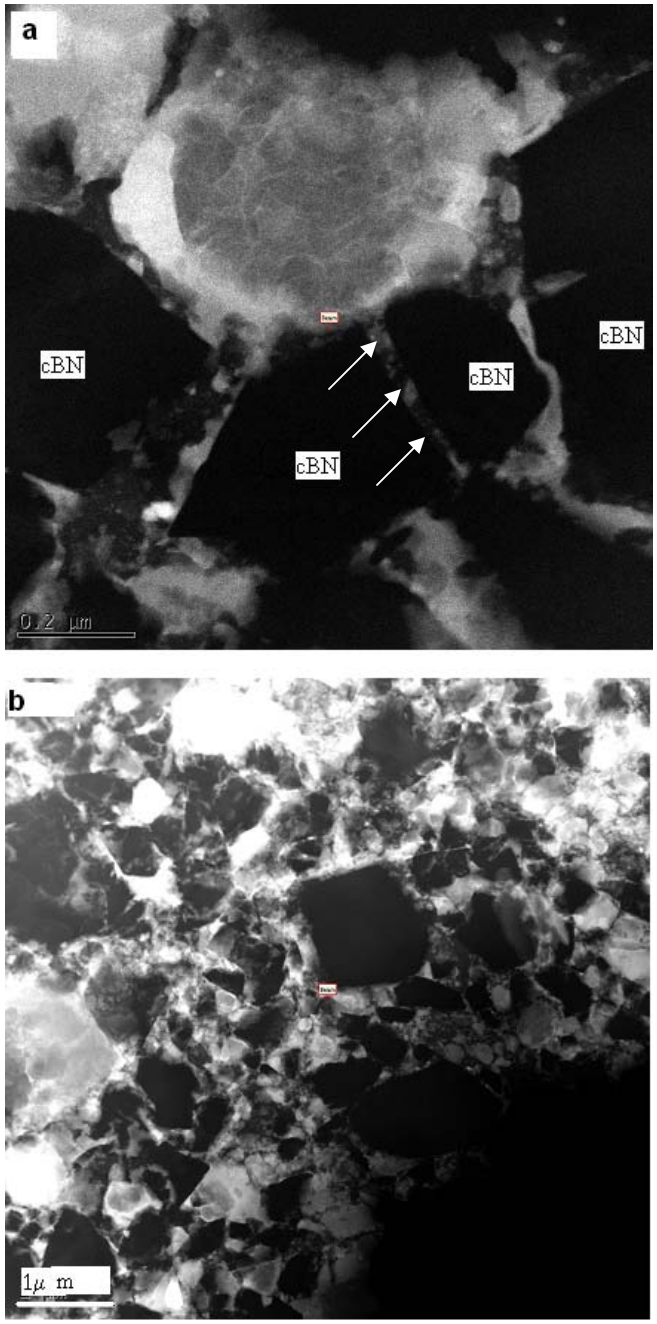

Figure 6.8. HAADF-STEM images of (a) binder particles between the cBN particles and (b) the general microstructure of sintered product showing higher proportion of submicron particles than the larger cBN.

Previous investigations [203-206] have already demonstrated that the morphology (atomic structure) of grain boundaries could change from faceted (atomically ordered) to rounded (atomically disordered) as the boundary step free energy decreased.

Consequently, different fractions of the faceted boundaries between polycrystalline samples were expected to form.

In the present work, two types of morphology of PcBN/binder boundaries: straight and rounded were distinguished in the STEM images (Figure 6.8). Straight boundaries were mostly microfaceted (atomically ordered) boundaries (Figure 6.7). The STEM micrographs (Figure 6.8b) also showed that the pressure applied enhanced the crushing of the initial cBN particles from 2 μm across to smaller than 500 nm. The crushing of the cBN particles would mostly occur during the pressure ramp-up stage at low temperature in the HPHT press and, to a lesser extent during the attrition milling due to the lower impact energy and pressure generated in the powder particles trapped between the balls in the last process.

It was shown in Chapter 4 that the properties and sizes of the starting powder particles affected the transmission of the mechanical energy from the milling balls to the powder particles, thus the deformation and transformations of the materials. The particle size, hardness, ductility and grain structure of the binder particles could therefore affect the fracturing rate and the energy stored in the cBN crystals. Part of the mechanical energy input during the pressing of the powders would have therefore been consumed to deform the particles of a soft binder like the Ti(C,N) : Al powder mixtures used in the common practice of PcBN sintering. Thus, the fracturing of the cBN particles is hindered and the microstructures of the sintered products are coarse (Figure 6.2.a).

The dissolution of W in Ti(C,N) enhanced the fracturing of the cBN particles and the formation of the nanostructured binder pools. The sintered microstructures of the PcBN and the binder pools became finer (Figure 6.2.b through to 6.2.d and Figure 6.6) with submicron grains. It is reasoned therefore that alloying with W increased the hardness and reduced the ductility of the binder particles. The particle size distribution determined by analysis of the SEM micrographs indicated that 90 vol.% of cBN particles were about 2μm across in the low cBN PcBN products sintered with Ti(C,N) : Al attrition milled binder (Figure 6.2.a) whereas on the other hand, 70 vol.% of particles in the products sintered with the Ti(C,N) - W based mechanically alloyed binders were smaller than 1μm (Figure 6.2. b, c and d) and contained a large proportion of particles that were smaller than 500nm, as shown in Figure 6.8.b.

Tungsten carbide substrates containing 10% Co were used as backing in PcBN sintering. Chemical and physical heterogeneities and the differences between the coefficients of thermal expansion of cBN and substrate would introduce residual stresses upon sintering that might induce cracking of the sintered materials during quenching in the press or during processing into semi-finished tools.

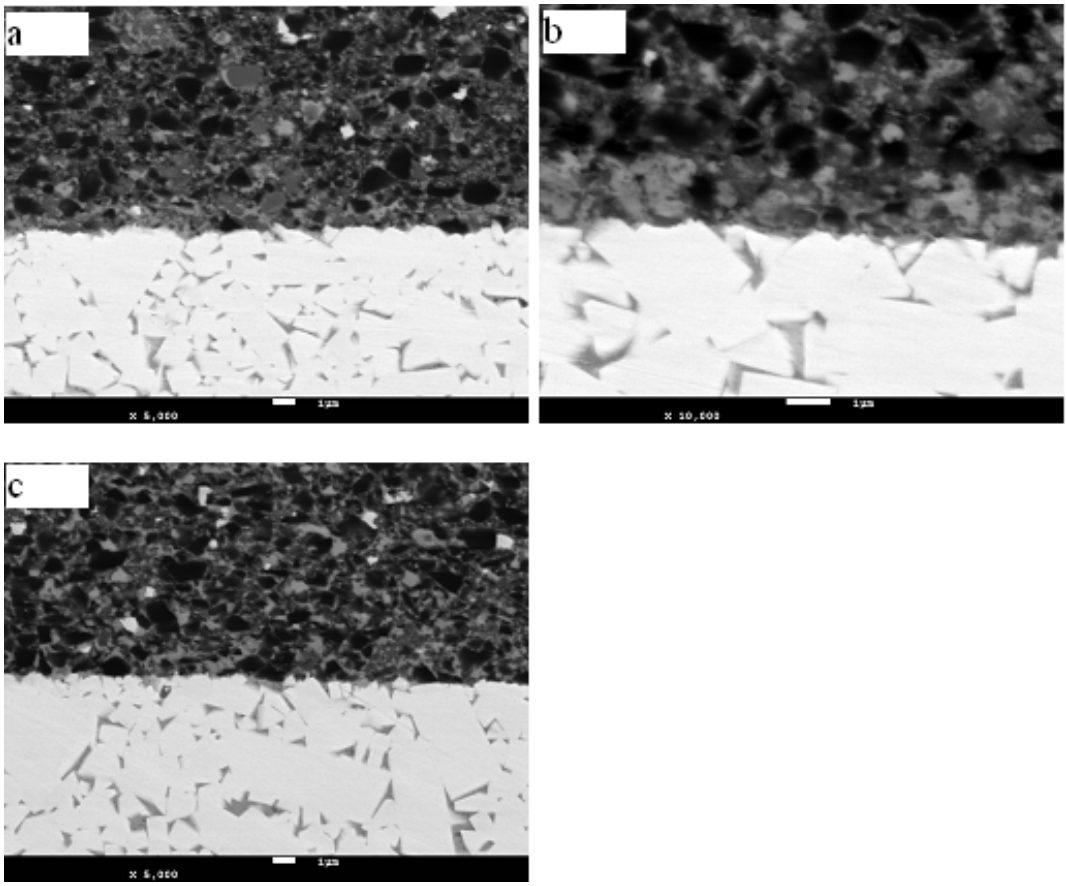

Figure 6.9. BSE-SEM micrographs of the interfaces between PcBN tables (top dark regions) and WC-10%Co substrates (bottom bright) sintered using MA binders (a) $Ti(C_{0.5}N_{0.05})$ - W milled for 12h, (b) milled for 48h and (c) $Ti(C_{0.5}N_{0.5})_{0.6}$ milled for 48h all mixed with 10% Al by attrition milling.

Other defects might be delamination of the PcBN table from the substrate and the formation of non-sintered regions (soft spots) inside the PcBN table. The cross sections showing the interfaces between the substrates and the PcBN were therefore studied under the SEM as illustrated in Figure 6.9.

Liquid cobalt infiltrated under the pressure and temperature conditions of sintering from the WC-10%Co substrate into the PcBN table. The low cBN PcBN was prepared with mixtures of 40wt% binder materials (mechanically alloyed) and 60wt% cBN. The metal

contents in any point of the sintered products would add up to ~40wt%. The balance is BN and a little carbon. A cobalt-denuded zone was formed on the carbide side of the substrate/PcBN interface, where Co content dropped to ~6.5±0.5wt%. Infiltration of liquid cobalt formed a concentration gradient in the PcBN side as shown in Figure 6.10.

The metal concentration profiles across the sections of the samples, hence the Co infiltration depth, determined by means of EDX are given in Figure 6.10a for the PcBN sintered using Ti(C,N) - W mechanically alloyed powders mixed with Al, and in Figure 6.10b for the case where binders were prepared by mechanically alloying Ti(C,N), W and Al in the high energy ball milling stage.

Cobalt infiltration is unwanted as it impairs the wear abrasion resistance and the cutting performance of the sintered tools, and thus should be minimised [31]. The use of mechanical alloying did not prevent Co infiltration from the substrate, a phenomenon driven by the flow of liquid Co under the high pressure inside the pores in the PcBN table. However, it is observed in Figure 6.10b that the concentration of Co remained lower in the infiltration layer formed when Al was alloyed with Ti(C,N) and W directly by ball milling than in the other case (Figure 6.10a).

On the other hand, there was no detectable infiltration of any of the binder constituents (Ti, W or Al) into the substrate. The sintering profile comprises first the application of the pressure before heating. Cobalt melting therefore occurs under a 5GPa pressure,

which leads to the formation of a high pressure - high velocity flow of Co inside the pores in the PcBN table.

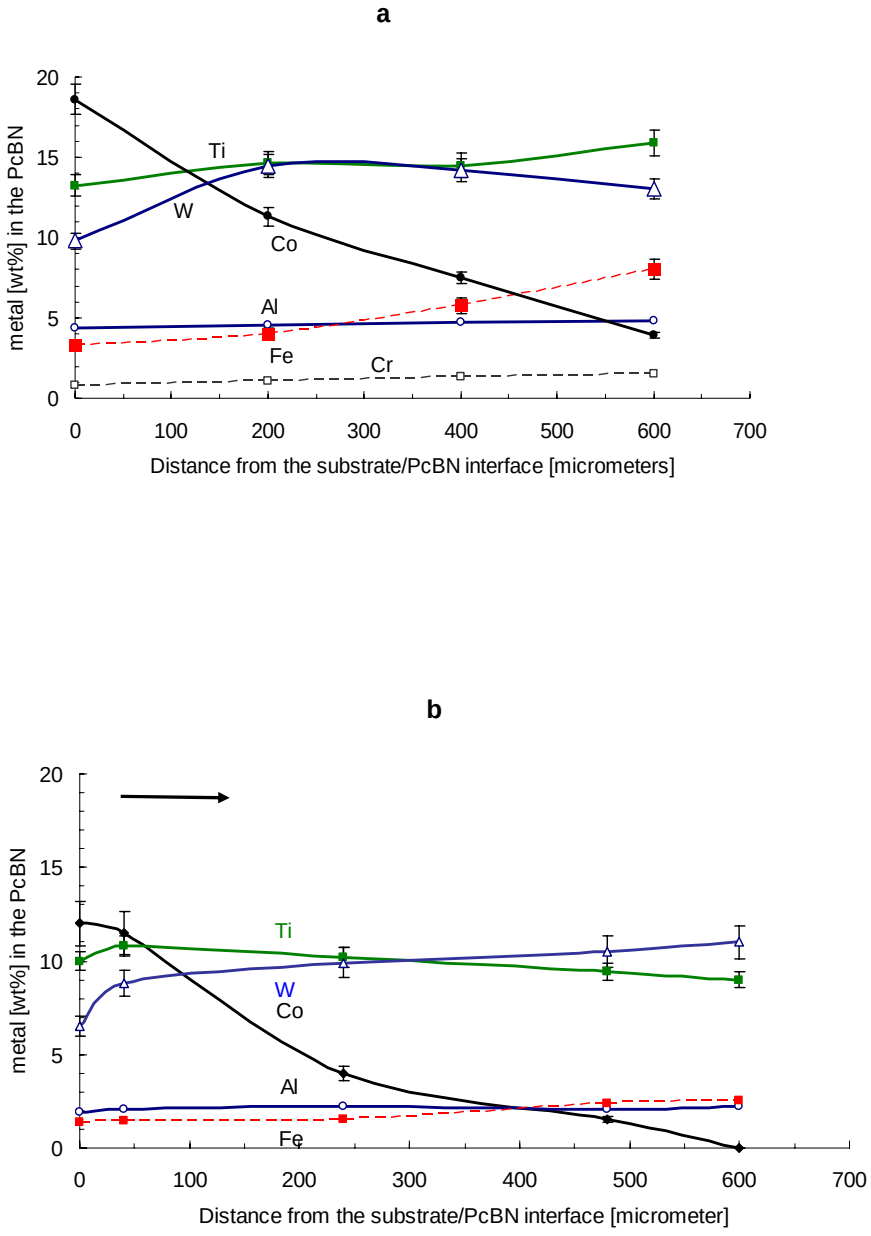

Figure 6.10. Metal content profiles along the infiltration layer; the arrow indicates the direction from the substrate/PcBN interface inside the PcBN table. The balance at each point mainly consists of BN.

It is suggested here that the flow of liquid cobalt dragged some of the Ti(C,N)-W-Al binder constituents from the interface inside the PcBN table, thus contributing to the dilutions in binder elements noticed along the interfaces. High melting temperature and stability of the phases (Σ), (Ω) and (ω) formed in the mechanically alloyed binders could be other reasons of the absence of infiltration of the alloyed elements toward the substrate.

6.4. Effect of pressure on the structural composition of the binder phase

The crystal structures and phase compositions of the binders under different pressures were investigated by the XRD technique. The mixtures of boron nitride with the binders were annealed at about 1350˚C in a vacuum of 10^{-8} bar and under 1bar in an argon atmosphere. The materials were also sintered in industrial conditions under a pressure of 50000 bars (5GPa).

The XRD patterns of the products formed in the mixtures containing $Ti(C_{0.5}N_{0.05})$ - W milled for 48h and mixed with Al are presented in Figure 6.11, where it is observed that the binder material annealed under vacuum contained a BCC product (τ) rich in W, whose structure is close to the $Al_{0.13}W_{0.57}Ti_{0.30}$ given in the ICSD Database [200].
The contaminating elements Fe and Cr were alloyed with W in a HCP phase (η), whose structure was close to Fe_7W_3 according to the same database. However, the major constituent of the binder material annealed under 1 bar pressure in an argon atmosphere was an FCC phase (σ), whose structure was close to $(Ti_{0.8}W_{0.2})C$ [200].

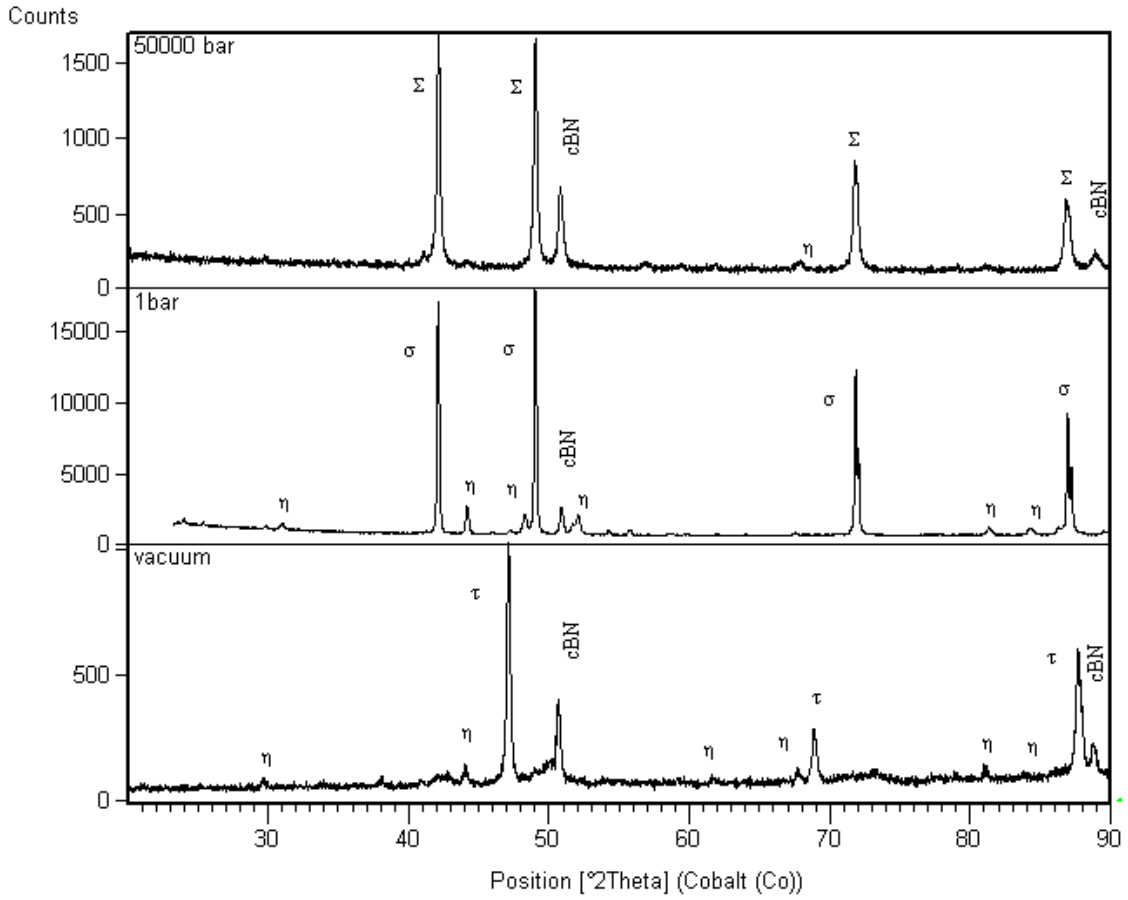

Figure 6.11. XRD patterns of the mixtures of cBN with $Ti(C_{0.5}N_{0.05})$ - W mechanically alloyed binders mixed with Al heated to ~1400˚C under different pressures, showing the formation of a BCC phase (τ) under vacuum, FCC phases (σ) and (Σ) at high pressure and the dissolution of the contaminant product (η).

The XRD results suggest that mobility of Al and Ti were higher under vacuum, which enhanced their dissolution in W and the formation of the products (τ) and (η). The diffusion coefficient of Ti decreased at normal and high pressures, and it rather behaved as solvent in W and matrix of the binder product (σ). The contaminant atoms combined in the Fe_7W_3 particles were dissolved in the crystals of (σ), which transformed into the FCC (Σ) under high pressure.

The intensities of the XRD peaks of the binder phase and the contaminating compound (η) formed in the PcBN sintered under high pressure were roughly 10 times smaller than those of the material annealed under 1 bar pressure. The short broad peaks indicate that the crystallites of the binder phase (Σ) formed during the high pressure sintering were fine and the lattice strains were high.

The XRD peaks of the mixtures of the cBN with $Ti(C_{0.5}N_{0.5})_{0.6}$ - W milled for 48h and mixed with Al are shown in Figure 6.12, where it is observed that a single phase BCC product (τ) was formed during the annealing under vacuum. The binder material decomposed into two constituents: an FCC phase product (Ω) rich in Ti and Al, which dissolved the contaminating Fe, and a BCC phase product (κ) rich in W. The product (κ) formed during annealing under normal pressure has been dissolved into the binder matrix under 5GPa.

The binder phase formed under 5GPa contained about 63% of an FCC product (Ω) and 37% of a HCP product (ω) rich in W, whose composition was close to $WC_{0.9}$ [200]. Thus, the low pressure annealing enhanced the transformation of $Ti(C_{0.5}N_{0.5})_{0.6}$ - W mechanical alloys by inversing the roles of W from solute in solvent of Ti, whereas decomposition into (Ω) and (ω) was observed under 5GPa. The low pressure annealed binder products in both the $Ti(C_{0.5}N_{0.05})$ - W and $Ti(C_{0.5}N_{0.5})_{0.6}$ - W based systems contained particles of solution of W that dissolved Ti and Al. The destruction of W crystals subjected under high pressure favoured the dissolution of its atoms in Ti(C,N) lattices, which led to the formation of different products in the binder materials.

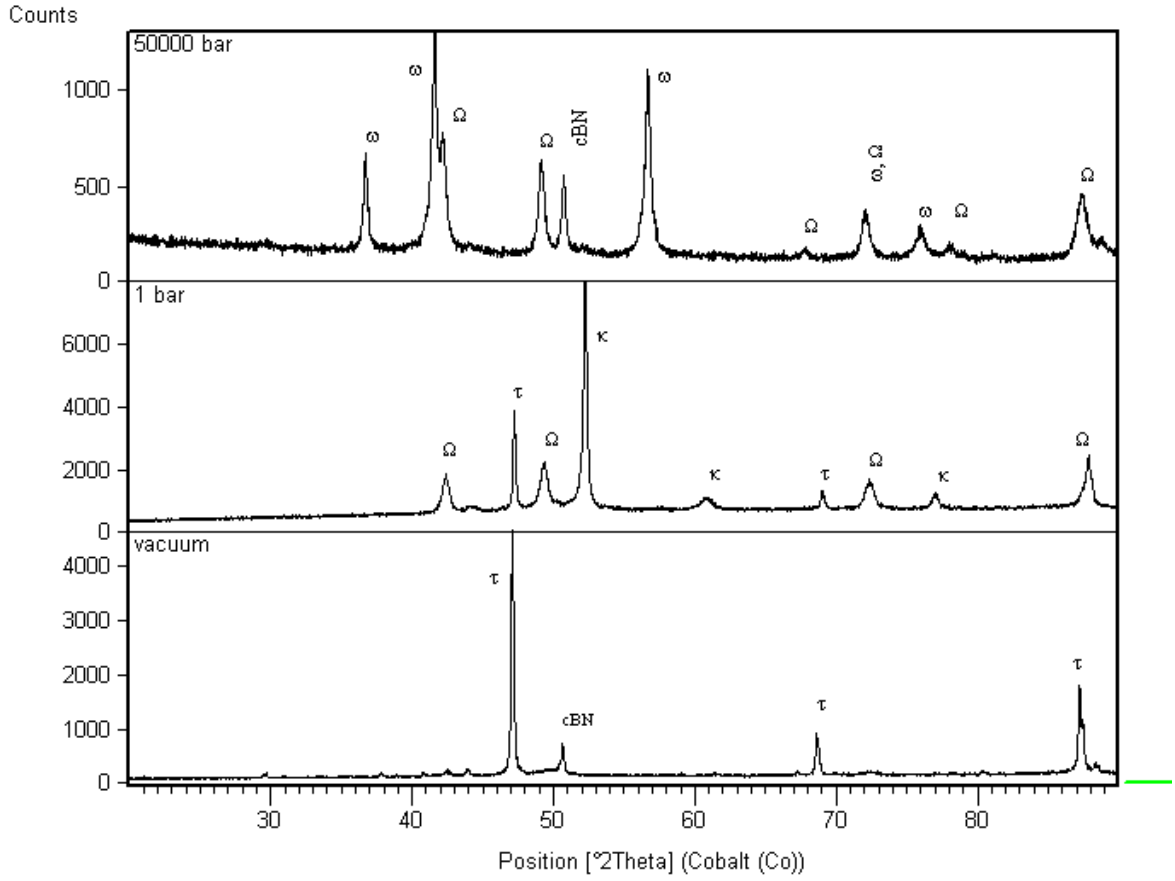

Figure 6.12. XRD patterns of the annealed mixtures of cBN with $Ti(C_{0.5}N_{0.5})_{0.6}$ - W mechanically alloyed binders mixed with Al, showing the formation under vacuum of the product (τ), the normal pressure phase (κ) and the products (Ω) and (ω) formed under 5GPa.

6.5. Effect of temperature on phase formation under vacuum

The high temperature XRD patterns of the $Ti(C_{0.5}N_{0.05})$ - W mechanically alloyed powder and attrition mixed with cBN and Al were determined under vacuum at 25˚C, 650˚C, 750˚C, 850˚C, 950˚C, 1050˚C and 1200˚C using a hot stage. The evolution of the patterns is illustrated in selected patterns shown in Figure 6.13.

The XRD peaks indicate the formation of the W-rich phase (τ) occurred at about 950˚C. The corresponding peak intensities increased as the temperature increased, due to crystallite growth and increased proportion. The product (η) that dissolved the contaminating Fe precipitated at about 1200˚C and remained stable after cooling down to room temperature.

However, Figure 6.14 shows that the formation temperature of the product (τ) in the $Ti(C_{0.5}N_{0.5})_{0.6}$ - W based binder was as low as 850˚C, and the contaminating Fe was dissolved in the same phase, unlike the precipitation of the product (η) as observed in the $Ti(C_{0.5}N_{0.05})$ - W type of binder mixture (Figure 6.12). The $(Al_{0.5}W_{0.5})C_{0.5}$ HCP compound [200] formed during the treatment of $Ti(C_{0.5}N_{0.5})_{0.6}$ - W - Al mixtures dissolved above 1050˚C, where the product (τ) was the only binder product detected by XRD.

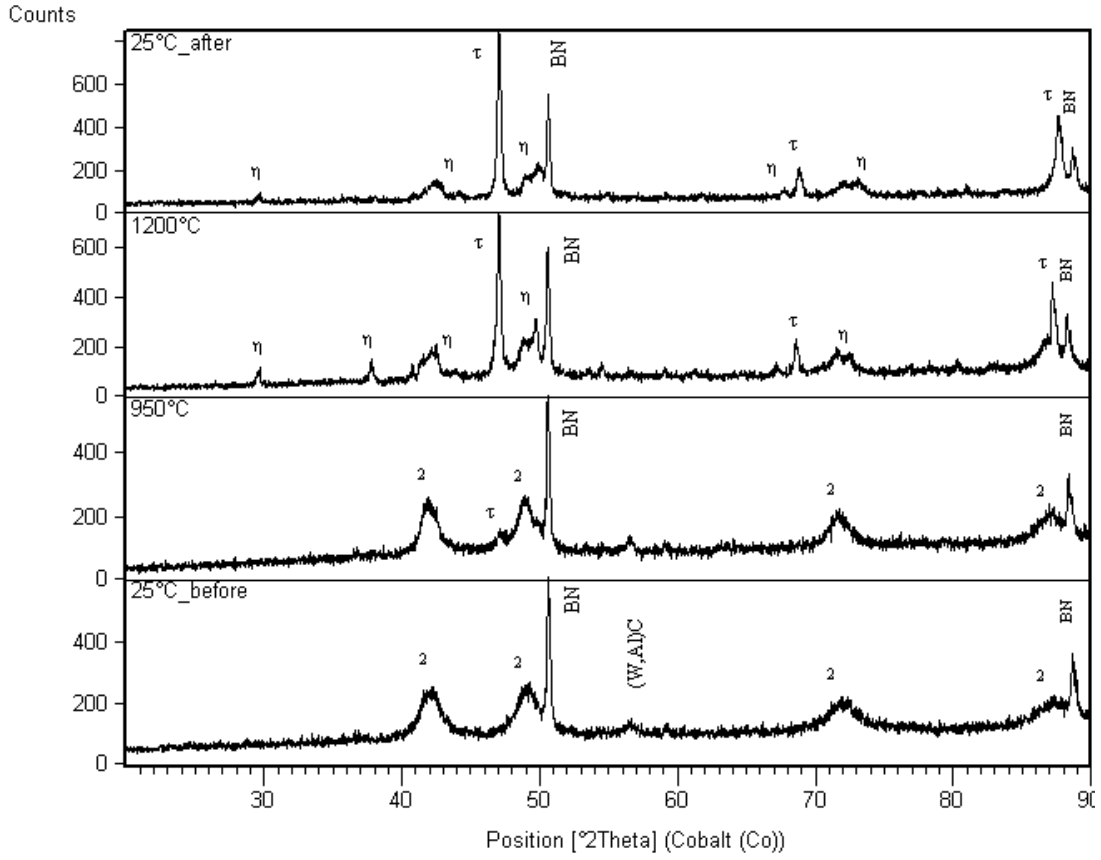

Figure 6.13. XRD patterns illustrating the effect of temperature, under vacuum, on the transformation of the mixture of cBN with mechanically alloyed $Ti(C_{0.5}N_{0.05})$ - W milled for 48h and attrition mixed with Al.

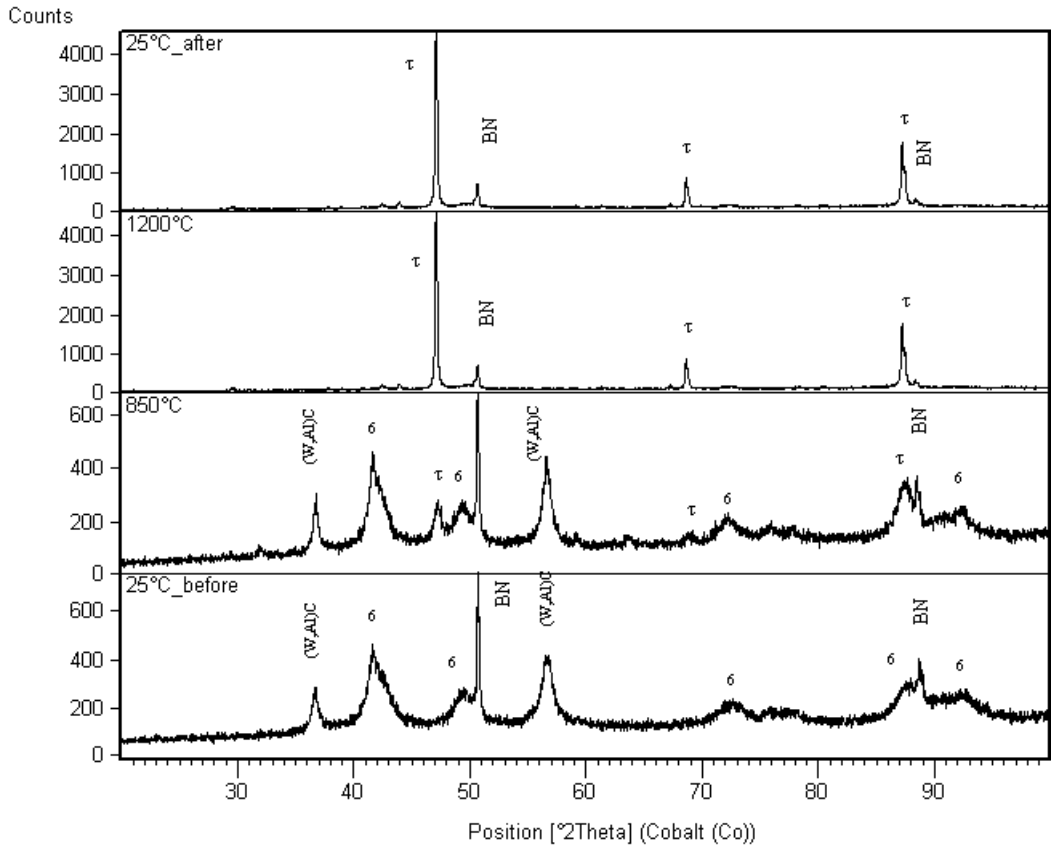

Figure 6.14. XRD patterns illustrating the effect of temperature, under vacuum, on the transformations of mechanically alloyed $Ti(C_{0.5}N_{0.5})_{0.6}$ - W milled for 48h and attrition mixed with Al, showing the dissolution of (W,Al)C in phase (6) formed during high energy ball milling and the formation of a single phase BCC product (τ).

The pressure applied to the system, temperature and type of Ti(C,N) all contributed to the crystal structures and compositions of the products formed in the binder and to the behaviour of the contaminating Fe. A general observation was that the HPHT sintering favoured the formation of Ti(W,Al) solutions and such compounds (Σ) and (Ω), whereas W(Ti,Al) products were predominantly formed under vacuum.

These tendencies show that Ti(C,N) crystals are more stable than W and Al, which are decomposed and their atoms dissolved under HPHT conditions, whereas W was the

stable constituent when the binder materials were heated under vacuum; thus it dissolved Ti and Al.

The stability of W crystals under vacuum was attributed to its elevated melting temperature, whereas the mobility of Ti and Al atoms increased and their solubility in W increased. It was noticed in Chapter 4 that W and Al crystals were quickly destroyed during ball milling and their atoms dissolved in or reacted with Ti.
The solvent character of Ti at high pressure was therefore rather ascribed to the fast destruction of W and Al crystals under HPHT conditions and the subsequent diffusion of the atoms, which enhanced their solubility in the Ti(C,N) crystals.

6.6. Sintering of low cBN PcBN using 55% Ti(C,N) – 35% W – 10% Al alloyed binders

Alternatively to the mixing of Ti(C,N) - 40wt% W mechanical alloys with Al by attrition milling, binders were prepared by alloying 55% Ti(C,N) - 35% W - 10% Al in high energy ball milling. Typical microstructures of low cBN PcBN sintered with the last type of mechanically alloyed binders are shown in Figure 6.15.

The binder phases were generally homogeneous after HPHT sintering. The contamination by WC particles observed in Figure 6.15b was inherited from the mixing-homogeneisation of cBN with the MA binder powders by attrition milling, which used WC balls.

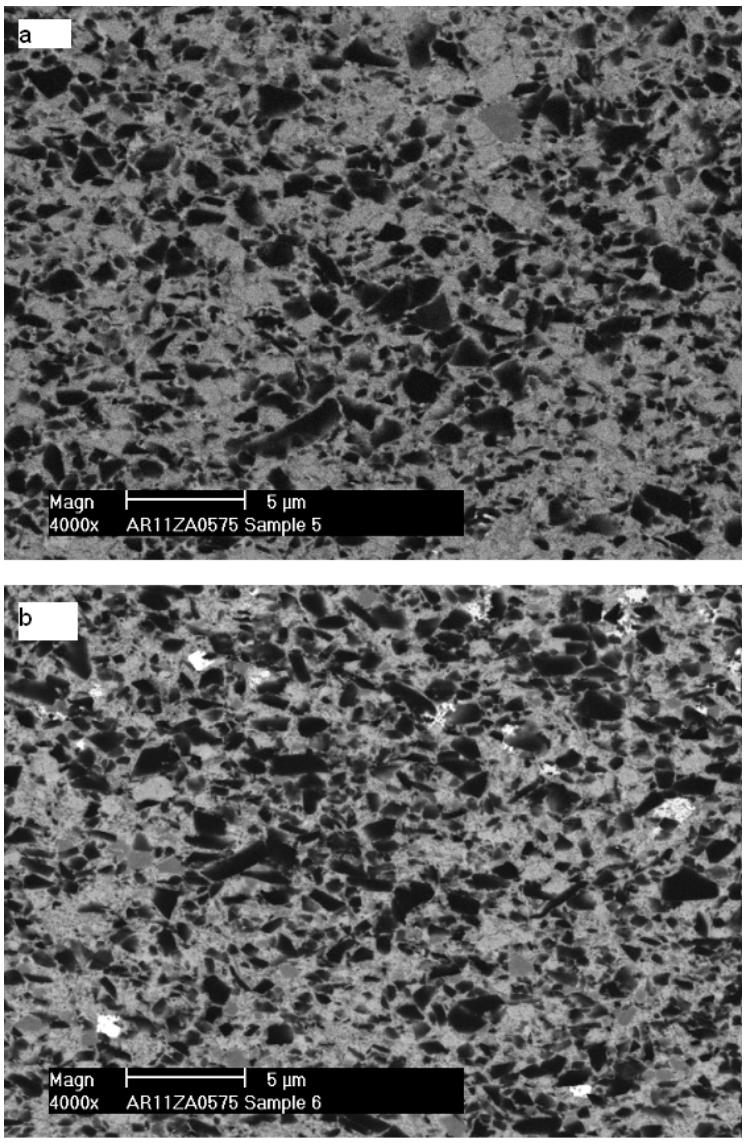

Figure 6.15. BSE-SEM images of low cBN PcBN sintered with 55% Ti($C_{0.5}N_{0.05}$) - 35% W - 10% Al binder milled for (a) 12h and (b) 32h, showing cBN particles (dark contrast), the binder (grey contrast) and traces of contamination by WC from milling balls (bright contrast in Figure b).

The oxygen contents of the PcBN sintered using 55% Ti(C,N) - 35% W - 10% Al mechanically alloyed binder was 2±0.3wt% which is lower than in custom PcBN (~7.0±1.0wt% O) [10] and in those made using the Ti(C,N) - W (~8wt% O) alloyed powders that were mixed with Al in an attrition mill.

It is therefore concluded that Al and the way it is introduced may determine the level of oxygen in the sintered PcBN. Mechanical alloying with Ti(C,N) and W stabilises Al in the products, such as (Ω) and (σ), formed during ball milling, and thus prevent Al from carrying oxygen inside the PcBN.

6.7. Improvement to PcBN sintering industrial practices

It is the first time that W-containing binders were successfully synthesized, in which W is dissolved in solid solution with Ti(C,N) and Al. Many works reported on the expected strength and mechanical performance of PcBN hard tools sintered with binders which contain refractory metals such as Hf, Ta and W [10, 207-212]. However, all of them attempted to incorporate Hf, Ta or W by attrition milling or fine dispersion in the Ti(C,N). This resulted in inhomogeneous binder phases as the refractory metals were not dissolved during HPHT sintering. The refractory particles played an adverse role as residual thermal stress raisers, which led to thermal cracking or non-sintering of PcBN.

The oxygen content in sintered commercial high cBN PcBN (containing only ~15wt% binder) is ~7wt% [10, 207, 208, 211, 212], which contributes to the brittle behaviour of the hard tools. The oxygen content achieved using the binder containing W were lower than 2wt%, despite the large amount of binder (~40wt%) in the low cBN PcBN prepared.

Mechanical alloying of the binders is proven to solve all these challenges, and thus it is one efficient way of dissolving refractory metals in the binders used for PcBN sintering

and limiting their oxygen sensitivity. The microstructures formed are homogeneous, and no cracks or delamination were observed. PcBN was still sintered near the lower limits of pressure (~5GPa) and temperature (~1500˚C) ranges established by the industrial practice, which are 5 - 8GPa and 1400˚C - 2200˚C [10, 207-212].

Pre-reaction of binder mixtures with Al by heating at 1050˚C - 1450˚C for five hours under controlled atmosphere is used in industrial practice [10, 207, 208, 211] to alloy the binder constituents. Mechanical alloying allowed the suppression of the pre-reaction stage from the synthesis of PcBN.

6.8. Elastic properties and hardness of the low cBN PcBN sintered materials

Seven variants of equal mass of PcBN and binder materials, defined in Table 6.3, were sintered at about 1500˚C, under a pressure of 5.5GPa. The elastic properties determined using a Krautkramer USIP 12 Pulse echo ultrasonic equipment with 50 MHz longitudinal probe and 20 MHz transverse probe and the micro-Vickers hardness measured under 2 kg load in a Wilson-Wopert 402MVD testing machine are given in Table 6.4. Densities of the sintered products were determined by means of Archimedes' method, and are also given in Table 6.4.

Shear moduli of PcBN materials sintered with MA binders were practically identical to that of a commercial low cBN PcBN product sintered in the same conditions of pressure and temperature with Ti(C,N) binder pre-reacted with 10wt.% Al at about 1050˚C.

However, Poisson's ratios, Young's and shear moduli of new products were higher than that of the reference product. Alloying with W increased the density of the binder phase and hence that of the sintered PcBN.

Table 6.3. Compositions and milling times of binder materials used in sintering of candidate PcBN products.

PcBN variant No.	**Binder compositions and preparation**				
	T(C,N) Type 55wt%	**W [wt%]**	**Al in ball milling [wt%]**	**Al in attrition milling [wt%]**	**Milling time**
v1	$Ti(C_{0.5}N_{0.05})$	35	10	-	12h
v2	$Ti(C_{0.5}N_{0.05})$	35	10	-	24h
v3	$Ti(C_{0.5}N_{0.05})$	35	10	-	48h
v4	$Ti(C_{0.5}N_{0.5})_{0.6}$	35	10	-	48h
v5	$Ti(C_{0.5}N_{0.05})$	35	-	10	12h
v6	$Ti(C_{0.5}N_{0.05})$	35	-	10	24h
v7	$Ti(C_{0.5}N_{0.5})_{0.6}$	35	-	10	32h

Micro-Vickers hardnesses of sintered products increased with milling time of the binder material. The increase in hardness was ascribed to the dissolution of W in Ti(C,N) during milling. Slightly higher hardnesses were achieved when Al was mechanically alloyed with Ti(C,N) and W powders in the binder than when it was attrition milled with cBN and Ti(C,N)-W MA products. Mechanical alloying in the presence of Al delayed the dissolution of W in Ti(C,N) as shown in Chapter 4, although the PcBN products formed after sintering had high hardness values. The increase in hardness could be attributed to the formation of Ti(Al,W) (C,N) compounds in the binder products.

Table 6.4. Densities, elastic properties and micro-Vickers hardness numbers of low cBN PcBN variants prepared using Ti(C,N)-xW-yAl mechanically alloyed binders.

PcBN variant	**Density**	**Young's modulus E** ±8 **[GPa]**	**Bulk modulus B**±5 **[GPa]**	**Shear modulus G**±4 **[GPa]**	**Poisson's ratio**	**Micro-Vickers hardness [Hv 2kg]** ±40
v1	5.11	596	340	244	0.205	3140
v2	5.15	603	344	250	0.210	3272
v3	5.08	610	348	250	0.210	3644
v4	4.99	600	341	248	0.200	3215
v5	5.12	592	337	245	0.199	3204
v6	5.08	602	340	248	0.200	3245
v7	5.15	605	346	248	0.210	3296
Commercial product	4.27	573	275	249	0.153	2900±100

The high Poisson's ratio, Young's and shear moduli of PcBN sintered with MA binders suggest that bonding between atoms in the binder and PcBN was different from those in the commercial product due to the alloying with of W. The effect of milling time and the type of Ti(C,N) on the elastic properties could therefore be attributed to type and numbers of chemical bonding formed during milling and subsequent sintering treatment of the products.

The present study investigated high energy ball milling as a route for solid state dissolution of tungsten in titanium carbonitride. The behaviour of the mechanical alloys

during HPHT sintering of seven low cBN PcBN variants was investigated to demonstrate the potential use and benefit of the alloys developed in industry. Behavioural and tribological studies of cutting tools made with materials described in this work are planed in further investigations, which require the expertise of researchers who specialise in manufacturing. Standards and methods they use are enumerated in Chapter 8, Section 8.2. Comparison between machining performances of the variants developed in this study and commercial product will bring new understanding into the effect of introducing W in the binder phase.

CHAPTER 7. CONCLUSION

The effects of milling parameters and composition of the starting powder mixtures on the transformation and alloying of Ti(C,N) - W and Ti(C,N) - W - Al powder mixtures processed by high energy ball milling were investigated in this work. The milling parameters included the milling time, which varied from 12 to 72h, and the temperature comprising milling at subzero temperature and above 25˚C. Two sub-stoichiometric Ti(C,N) stocks were selected, the $Ti(C_{0.5}N_{0.05})$ containing more interstitial elements than the $Ti(C_{0.5}N_{0.5})_{0.6}$. The transformation temperatures of the mechanically alloyed powders were determined by DTA and the annealing behaviour investigated by XRD, SEM and TEM. The potential use of the alloyed powders as binder in PcBN sintering was demonstrated by sintering of low cBN PcBN under 5GPa at 1400˚C. The main findings are summarised in the following sections.

7.1. Solid state transformation and alloying of the powder mixture constituents

The milling atmosphere affected the lattice strain of milled products, and the kinetics of solid state dissolution between the powder constituents. This effect was attributed to the nitriding of the material milled in nitrogen, or de-nitriding when milled in argon.

The mechanical alloying by substitution of Ti with W atoms leads to the shrinkage of the Ti(C,N) FCC lattice.

The access of nitrogen or oxygen atoms to the interstitial sites was hence restricted, which led to the simultaneous decrease of nitrogen and oxygen contents in the powders milled for longer times.

The lattice strain induced by high energy ball milling contributed to the driving force for the solid state diffusion between the powder constituents. The refinement of the crystallite size alone did not play a determinant role in the solid state dissolution process. However, the release of the stored crystallite lattice strain energy appeared to be the major determinant in mechanical alloying. Particle size reduction plays a necessary, but less significant role in solid state alloying.

The strain energy and the fine particle size contributed to the increased chemical reactivity with oxygen of the powders milled for 12h to 24h. The high oxygen contents in the powders milled for these intermediate times resulted from the oxidation during sample collection from the milling bowl and transportation to the oxygen analyzer equipment. Powders milled for 48h were more stable in the presence of oxygen. Their oxygen contents remained below 4% after 6 months storage in open air. The affinity of the powders with oxygen decreased after W dissolution in Ti(C,N), and the subsequent decrease in lattice strains.

7.2. Effect of 10wt% aluminium addition

The W peaks in XRD indicates that its BCC lattice was strained before its destruction and dissolution in Ti(C,N) after 48h milling. The EDX and EMPA analyses showed that part of Al contained in the mixtures has been dissolved in the orthorhombic W-rich phase.

Aluminium lowered the lattice strains, and subsequently the strain energy stored by the deformed crystals of Ti($C_{0.5}N_{0.05}$) and W milled above 25˚C. The slower kinetics of dissolution of W in Ti($C_{0.5}N_{0.05}$) in the presence of Al was attributed to the stability of the orthorhombic W(Al,Fe) formed in the early stage of milling and to the lower strain energy stored in Ti(Al) crystals.

The contact between the strained Al particles and the Ti(C,N) and W particles enhanced the diffusion of Al atoms in the particles and the formation of the W-Al and Ti-W-Al compounds. Aluminium preferably reacted with W particles, which released a higher lattice strain than Ti(C,N). The relaxation of the lattice strain after the maximum was reached contributed to the driving force for reaction and alloying between the powder constituents.

The evolution of the morphologies of Ti(C,N)-W mixtures show that fracturing of hard particles dominated in the early stage of milling in the absence of Al, whereas with Al, plastic deformation of particles and cold welding of Ti(C,N) and W particles by the softer Al prevailed at the same time.

7.3. Milling at subzero temperature

The microstructure of the Ti(C,N)-W-Al powder mixtures milled at temperatures between -140˚C and -5˚C showed that Al had an effect on the strain-induced transformations and alloying mechanisms.

It was observed that fracturing of particles dominated the early stage of milling in the absence of Al, whereas cold welding of the particles prevailed in the systems which contained Al. However, the strain rate of Ti(C,N) and W at subzero temperature increased in the presence of Al.

Although Al improved the rates of transformation at low temperature, the alloying of W with $Ti(C_{0.5}N_{0.05})$ was slower than observed during milling at higher temperatures. The crystalline of (W,Al) formed at low temperature were stable and the dissolution of W in the Ti(C,N) was therefore limited.

The use of a process control agent (PCA), 3wt% proportion of aluminium stearate added to powder mixtures, at low temperature was detrimental to the alloying process, due to the formation of viscous films around the particles. The lattice strain energy stored, thus the driving force for reaction, was low. The inhibition effect of the PCA was significant in mixtures milled without Al.

Binary titanium aluminides were not formed during milling below -5˚C for 24h as also reported by Yu *et al.* [187]. However, three-components T-W-Al, W-Al-C and Ti-W-C were formed in the same conditions. The large lattice strain in W crystals and the release of the stored energy as milling time increased was therefore the determinant factor of the driving force for alloying.

It was also noticed that the lattice strain of W grains increased faster in the presence of Al than in its absence. The increase of lattice strains in the presence of Al was ascribed to

the dissolution of Al atoms in the W lattices. Therefore, interaction between W and Al improved the kinetics of transformation during milling at subzero temperatures by two mechanisms:

- the increase of lattice strain during short milling time before relaxation at longer time
- and the fast diffusion of Al atoms during milling.

7.4. High temperature transformation in milled powders

The investigation on the effect of the milling on the annealing behaviour of milled Ti(C,N) - W powders showed that the reaction start and finish temperatures between constituents were lower in the system that had high residual lattice strains after milling. Crystal lattice strains were thermally released and strain free grains existed in milled powders annealed at about 1450˚C.

The milling time and annealing temperature determined the compositions of the product phases and contaminating intermetallic particles formed.

Thermal alloying was observed during annealing of $Ti(C_{0.5}N_{0.05})$ - 40wt% W mechanically alloyed products, whereas de-mixing of W-rich phases from the metastable solid solution occurred during annealing of the $Ti(C_{0.5}N_{0.5})_{0.6}$ - 40 wt% W milled powders.

The heat required for decomposition of the $Ti(C_{0.5}N_{0.5})_{0.6}$ - W metastable solid solution increased as the milling time increased. Conversely, positive heat of alloying contributed to the elevation of the maximum temperature changes recorded during heating of the $Ti(C_{0.5}N_{0.05})$ - W milled powders.

The contaminating Fe introduced by the stainless steel milling balls preferably reacted with W, rather than Ti, during annealing.

The annealed mechanically alloyed $Ti(C_{0.5}N_{0.05})$ - W - Al contained Al(Ti,W,Fe) particles dispersed in the Ti(W,Al,Fe) matrix.

However, the FCC W(Al,Fe,Ti) solution formed was not dissolved in the matrix of the product annealed at 1400˚C. The compositions of W(Al,Fe,Ti) grains formed in annealed $Ti(C_{0.5}N_{0.5})_{0.6}$ - W - Al powders contained more than 90wt% W, which was attributed to the low solubility between the Ti(W,Al) and the W(Al,Fe,Ti) solid solutions formed during milling.

The products formed after milling and annealing of Ti(C,N)-W and Ti(C,W)-W-Al powder mixtures differed in composition and structure from the predicted equilibrium phases [9]. The energy stored in crystals and defects introduced by milling enhanced the formation of metastable phases, which are not included in the equilibrium phase diagrams. These phases were thermally stable and did not decompose into predicted stable phases at the annealing temperature. Thermal stability of the mechanically alloyed powders is a requirement for the formation of single phase binder after HPHT sintering.

7.5. Sintering of low cBN PcBN with mechanical alloy binders

Longer milling time improved the homogeneity and the formation of nanostructured binder pools in the sintered products. A homogeneous product could be formed by milling $Ti(C_{0.5}N_{0.05})$-W mixtures for at least 24h and mixing with Al and cBN before annealing under normal pressure. Undissolved W reacted with Ti(C,N) to form a HCP phase of composition $WC_{0.9}$.

High pressure (5GPa) and temperature (1400˚C) applied during the PcBN sintering enhanced the thermal dissolution of the residual W and $WC_{0.9}$ in the binder matrix, hence the formation of a single phase binder.

Binder particles milled for 12h were characterized by core-rim structures after sintering, which were ascribed to incomplete diffusion of W atoms through the core of the particles of Ti(C,N). The core-rim structure inherited from the milling remained unchanged upon HPHT sintering, which showed the stability of the products of milling and the lack of significant diffusion during sintering.

The high pressure and temperature applied during sintering induced opposite structural effects in the binder phase than in the PcBN. The lattice strain in the PcBN phase increased, whereas a decrease was observed in the binder.

Crushing of the cBN particles to smaller sizes, thus the formation of finer sintered microstructures than in the custom PcBN sintered without W, was achieved by sintering with the hard W-containing alloyed binders.

The HPHT sintering did not prevent the thermal decomposition of the $Ti(C_{0.5}N_{0.5})_{0.6}$ - W based binder and the formation of $TiAl_{0.11}(C_{0.38}N_{0.35})$ and $WC_{0.9}$ as the main phases, even after milling for 48h. These two phases were formed during the annealing under normal pressure at 1050˚C. Their crystallite sizes increased under HPHT conditions.

The lattice strains of the binder and the PcBN were higher in the sintered materials prepared with the $Ti(C_{0.5}N_{0.5})_{0.6}$ - W binder than in those made using the $Ti(C_{0.5}N_{0.05})$ - W alloys. The differences were ascribed to the differences in C and N contents of the Ti(C,N) and the milling parameters, which determined the dissolution rates of W. The combination of the higher dissolution rate of W in Ti(C,N) with higher contents of C and N led to lower lattice strains in the products.

Straight and rounded morphologies characteristic of ordered and disordered boundaries were formed together. A limited proportion of sharp microfaceted boundaries was observed, which indicated a dissolution-precipitation-rearrangement process might have taken place during a liquid phase sintering.

The pressure and temperature applied during sintering or annealing had a strong effect on the compositions and the crystal structures of the phases formed in the mechanically alloyed binder.

Lower oxygen contents in sintered PcBN were achieved by mechanically alloying Ti(C,N), W and Al in the high energy ball milling stage. Low level of Co in the infiltration layer was also achieved when sintering PcBN with this type of binder. A link was established between the addition of Al at the attrition milling stage and high oxygen content in the sintered PcBN, thus should be avoided.

CHAPTER 8. FURTHER WORK

8.1. Sintering of high cBN PcBN using mechanically alloyed binders

It is hypothesized that sintering PcBN containing <15wt% binder would be even easier because it will introduce less W in the mixture, thus lower residual stresses. However, high cBN PcBN cutting tools would have higher wear resistance, hardness and longer life. It is expected that the density of the PcBN composite will increase by about 10% for a low cBN composite. Another study of interest could consist in the determination of the effect on the elastic properties of the composites of alloying W and Al to the binder phase. Additionally, Young's modulus, shear and bulk moduli and Poisson's ratios of PcBN can be accurately evaluated from the speeds of propagation of ultrasounds in the sintered materials, and these experiments could be undertaken.

Further analysis by high resolution TEM (HRTEM) would bring new insights to the understanding of the formation of PcBN/binder interfaces. A characterisation of the boundaries between phases would contribute to optimisation of interactions between the crystals of different constituents of the sintered products. Atom probe metrology and orientation imaging by EBSD technique may be useful to understand the orientation of the grains on the reaction. The orientations of PcBN/binder interfaces would affect the bonding strength and the coherence character of PcBN/binder boundaries. Optimised interfaces for high strength and high fracture energy can be achieved by (pressure, temperature) scan of sintering conditions and their effects on the PcBN/binder interfaces.

It appeared that cBN particles were crushed during the pressure up ramp in the HPHT system. The fracturing of these particles led to high compaction of the PcBN sintered product. It is expected that fracturing would occur along preferential crystal systems in cubic boron nitride that would affect the PcBN/binder interface and the micro-residual stress in the grains of the sintered products. Micro-Raman spectroscopy can be used to evaluate the micro-stress in an attempt to establish a relationship between properties and performance of the PcBN cutting tools.

8.2. Mechanical testing and assessment of machining performance

Machining performance of the sintered low cBN and high cBN PcBN needs to be assessed by standard abrasion, wear and chemical tests. It was hypothesized that dissolution of refractory metals in the binder will increase the mechanical performance of the hard tool. Most mechanical testing procedures for PcBN used in industry are defined by the manufacturers to comply with the specifications required by the end-users of the tools. Thus, wear testing, abrasion resistance and machining performance are evaluated according to company specific procedures and standards. The hardness and strengths of PcBN are so high that it is difficult to prepare testing specimens according to existing standard for mechanical testing for structural materials such as steels. Thus, each manufacturer has developed its standards. Such standards can be used for ranking different PcBN composites sintered with mechanically alloyed binders and comparison with commercial products.

Evaluation of machinability of working edges (chisels) of a finished tool and its cutting performance includes the investigation of thermal resistance, heat conductivity, cooling methods, chemical resistance against working environment, dissolution or reaction with workpiece material and the abrasion resistance. Cutting performances of tools are determined for well defined stages such as roughing or finishing of operations such as turning, interrupted turning, drilling, milling etc. These analyses require the use of material science and engineering methods such as SEM, TEM, fracture mechanics, failure analysis, vibrations, etc.

There is opportunity of other students and researchers to expand this work, i.e. by developing models based on relationships between the independent variables such milling parameters, atmosphere and sintering conditions and the microstructure or the performance of the tools.

REFERENCES

1. 64. Benjamin J.S., Mechanism of mechanical alloying. Metallurgical Transactions 1974 (8) 1929 – 1934

2. El-Eskandarany M.S., Sumiyama K., Aoki K. and Suzuki K., Morphological and structural evolutions of non-equilibrium titanium-nitride alloy powders produced by reactive ball milling. Journal of Materials Research 7 (1992) 888 – 893

3. Eckert J., Schultz L., Amorphization reaction during mechanical alloying: influence of milling conditions, Journal of Materials Science 26 (1991) 441-446

4. El-Eskandarany M.S., Synthesis of nanocrystalline titanium carbide alloy powders by mechanical solid state reaction. Metallurgical and Materials Transactions A: Physical Metallurgy and Materials Science 27 (8) (1996) 2374 – 2382

5. Eckert J., Schultz L., Urban K., Glass-forming ranges in transition metal-Zr alloys prepared by mechanical alloying. Journal of the Less-Common Metals 145 (1988) 283-291

6. Suryanarayana C., Mechanical alloying and milling. Progress in Materials Science 46 1-2 (2001) 1-184

7. Maweja K., Phasha M., van der Berg N., Microstructure and crystal structure of an equimolar Mg-Ti alloy processed by Simoloyer high energy ball mill. Powder Technology 199 (2010) 256 – 263

8. Phasha M., Maweja K., Babst C., Mechanical alloying by ball milling of Ti and Mg elemental powders: Operation conditions considerations. Journal of Alloys and Compounds 492 (1-2) (2010) 201 – 207

9. ASM Alloy Phase Diagrams Center, P. Villars, editor-in-chief; H. Okamoto and K. Cenzual, section editors; AsmEnterprise/APD, ASM International, Materials Park, OH, 2006.

10. Can N., New low CBN PCBN materials with improved crater wear resistance. DRL/ 2004. Confidential.

11. Walmsley J.C., Lang A.R. A transmission electron microscope study of a cubic boron nitride-based compact material with AlN and AlB_2 binder phases. Journal of Materials Science 22 (1987) 4093 – 4102

12. Klimczyk P., Benko E., Lawniczak-Jablonska K., Piskorska E., Heinonen M., Ormaniec A., Gorczynska-Zawislan W., Urbanovich V.S. Cubic boron nitride-Ti/TiN composites: hardness and phase equilibrium as function of temperature. Journal of Alloys and Compounds 382 (1-2) (2004) 195 – 205

13. Neo K.S, Rahman M., Li X.P., Khoo H.H., Sawa M., Maeda Y. Performance evaluation of pure cBN tools for machining of steel. Journal of Materials Processing Technology 140 (1-3) (2003) 326 – 331

14. Wentorf R.H., De Vries R.C., Bundy F.P. Sintered superhard materials. Science 208 (1980) 873 – 880

15. Zhao Y., Wang M. Effect of sintering temperature on the structure and properties of polycrystalline cubic boron nitride prepared by SPS. Journal of Materials Processing Technology 209 (2009) 355 – 359

16. Arsecularatne J.A., Zhang L.C., Montross C., Matthew P. On machining of hardened AISI D2 steel with PcBN tools. Journal of Materials Processing Technology 143 – 144 (2006) 244 – 252

17. Katuku K., Koursaris A., Sigalas I. Wear mechanisms of PcBN cutting tools when dry turning ASTM Grade 2 austempered ductile iron under finishing conditions. Wear 268 (2010) 294 – 301

18. Katuku K., Koursaris A., Sigalas I. Wear, cutting forces and chip characteristics when dry turning ASTM Grade 2 austempered ductile iron with PcBN cutting tools under finishing conditions. Journal of Materials Processing Technology (5) 209 (2009) 2412 – 2420

19. Cook M.W., Bossom P.K. Trends and recent developments in the material manufacture and cutting tool application of polycrystalline diamond and polycrystalline cubic boron nitride. International Journal of Refractory Metals and Hard Materials 18 (2000) 147 – 152

20. Jiang W., More A.S., Brown W.D., Malshe A.P. A cBN-TiN composite coating for carbide inserts: Coating characterization and its applications for finish hard turning. Surface and Coatings Technology 201 (2006) 2443 – 2449

21. Agha S., Liu C.R. On modeling the rolling contact fatigue performance based on residual stresses generated by superfinish hard turning. American Society of Mechanical Engineers, Manufacturing Engineering Division, MED 11 (2000) 1047 – 1053

22. Jacobson M. "Residual stress generated in bearing steel during hard turning", Thesis, Department of Product and Production Development, Chalmers University of Technology, S-412 96 Gotebord, Sweden, 2001

23. Matsumoto S., Zhang W.J. The introducing of fluorine into the deposition of BN: a successful method to obtain high quality, thick cBN films with low stress. Diamond and Related Materials 10 (2001) 1868 – 1874

24. Mirakami P.B., McCarthy K.F., Medlin D.L. Review of advances in cubic boron nitride film synthesis. Materials Science and Engineering R 21 (1997) 47-100

25. Jun W., Ying L., Ping Z., Jiancai P., Jinwen Y., Mingjing T. Effect of WC on the microstructure and mechanical properties in the $Ti(C_{0.7}N_{0.3})_{-x}WC$-$Mo_2C$-(Co,Ni) system. International Journal of Refractory Metals and Hard Materials 27 (2009) 9-13

26. Manoj Kumar B.V., Ram Kumar J., Bikramjit B. Crater wear mechanisms of TiCN-Ni-WC cermets during dry machining. International Journal of Refractory Metals and Hard Materials 25 (2007) 392 – 399

27. Wang J., Liu Y., Feng Y., Ye J., Tu M. Effect of NbC on the microstructure and sinterability of $Ti(C_{0.7}N_{0.3})$-based cermets. International Journal of Refractory Metals and Hard Materials 27 (2009) 549 – 551

28. Li Y., Liu N., Zhang X., Rong C. Effect of WC content on the microstructure and mechanical properties of (Ti, W)(C,N) – Co cermets. International Journal of Refractory Metals and Hard Materials 26 (2008) 33-40

29. Zhou S., Zhao W., Xiong W. Microstructure and properties of the cermets based on Ti(C,N). International Journal of Refractory Metals and Hard Materials 27 (2009) 26 – 32

30. Kim J.W., Ahn S.Y., Kang S., Effect of the complete solid-solution phase on the microstructure of Ti(C,N) – based cermets. International Journal of Refractory Metals and Hard Materials 27 (2009) 224 – 228

31. Ahn S., Kang S. Dissolution phenomena in the $Ti(C_{0.7}N_{0.3})$ – WC – Ni system. International Journal of Refractory Metals and Hard Materials 26 (2008) 340 – 345

32. Ahn S., Kang S. Effect of various carbides on the dissolution behavior of $Ti(C_{0.7}N_{0.3})$ in a $Ti(C_{0.7}N_{0.3})$ – 30Ni system. International Journal of Refractory Metals and Hard Materials 19 (2001) 539-545

33. Ahn S.Y., Kang S. Formation of core/rim structures in Ti(C,N) – WC – Ni cermets via a dissolution and precipitation process. Journal of The American Ceramic Society 83(6) (2000) 1489 – 1494

34. Ahn S.Y., Kim S.W., Kang S. Microstructure of Ti(C,N) – WC – NbC – Ni cermets. Journal of The American Ceramic Society 84(4) (2001) 843 – 849

35. Ahn S.Y., Kang S. Effect of WC particle size on microstructure and rim composition in the Ti(C0.7N0.3)-WC-Ni system. Scripta Materialia 55(11) (2006) 1015 – 1018

36. Zhang X., Liu N. Microstructure, mechanical properties and thermal shock resistance of nano-TiN modified TiC-based cermets with different binders. International Journal of Refractory Metals and Hard Materials 26 (2008) 575 – 582

37. Liu N., Yin W.H., Zhu L.W. Effect of TiC/TiN powder size on microstructure and properties of Ti(C,N)-based cermets. Materials Science and Engineering A 445-446 (2007) 707 – 716

38. Chao S., Liu N., Yuan Y.P., Han C.L., Xu Y.D., Shi M. Microstructure and mechanical properties of ultra-fine Ti(C,N)-based cermets fabricated from nano/submicron starting powders. Ceramic International 31 (2005) 851 – 862

39. Cardinal S., Malchere A., Garnier V., Fantozzi G. Microstructure and mechanical properties of TiC-TiN based cermets for tools application. International Journal of Refractory Metals and Hard Materials 27 (2009) 521 – 527

40. Lahiri I., Bhargava S. Compaction and sintering response of mechanically alloyed Cu-Cr powder. Powder Technology 189 (2009) 433 – 438

41. Fang Z.Z., Wang X., Ryu T., Hwang K.S., Sohn H.Y. Synthesis, sintering and mechanical properties of nanocrystalline cemented tungsten carbide – A review. International Journal of Refractory Metals and Hard Materials 27 (2009) 288 – 299

42. Fang Z.Z., Eason J.W. Study of nanostructured WC-Co composites. International Journal of Refractory Metals and Hard Materials 13(5) (1995) 297 – 303

43. Goren-Mugistein G.R., Berger S., Rosen A. Sintering study of nanocrystalline tungsten carbide powders. Nanostructured Materials 10(5) (1998) 795 – 804

44. Porat R., Berger S., Rosen A. Dilatometric study of the sintering mechanism of nanocrystalline cemented carbides. Nanostructured Materials 7(4) (1996) 429 – 436

45. Schubert W.D. In: 2000 International conference on tungsten hard metals and refractory alloys, Annapolis, MD, USA; 2000

46. Benko E., Stanislaw J.S., Królicka B., Wyczesany A., Barr T.L., cBN-TiN, cBN-TiC composites: chemical equilibria, microstructure and hardness mechanical investigations. Diamond and Related Materials 8 (1999) 1838 – 1846

47. Smith W.P., Missen R.W. "Chemical reaction equilibrium analysis; Theory and Algorithms". John Wiley & Sons, New York, 1982

48. Casanova C.A.M., Balzaretti N.M., Voronin G., da Jornada J.A.H. Experimental study of plastic deformation during sintering of cubic boron nitride compacts. Diamond and Related Materials 8 (1999) 1451 – 1454

49. Lv R., Liu J., Li Y., Li S., Kou Z., He D. High pressure sintering of cubic boron nitride compacts with Al and AlN. Diamond and Related Materials 17 (2008) 2062-2066

50. Kato H., Shintani K., Sumiya H. Cutting performance of a binder-less sintered cubic boron nitride tool in the high-speed milling of gray cast iron. Journal of Materials Processing Technology 127 (2002) 217 – 221

51. Hulbert D.M., Jaing D., Dudina D.V., Mukherjee A.K., The synthesis and consolidation of hard materials by spark plasma sintering. International Journal of Refractory Metals and Hard Materials 27 (2009) 367 – 375

52. Xavier F.A., Schramm B., Mit Keramik einen guten Schnitt machen. WB12 (2005) 18–24

53. Harris T.K., Brookes E.J., Taylor C.J., The effect of temperature on the hardness of polycrystalline cubic boron nitride cutting tool materials. International Journal of Refractory Metals and Hard Materials 22 (2004) 105 – 110

54. Harris T.K., Brookes E.J., Taylor C.J., The flow stress of PcBN cutting tool materials at high temperature. International Journal of Refractory Metals and Hard Materials 19 (2001) 265-273

55. De Souza Jr., A.M., Sales W.F., Santos S.C., MacHado A.R., Performance of single Si_3N_4 and mixed Si_3N_4 + PcBN wiper cutting tools applied to high speed face milling of cast iron. International Journal of Machine Tools and Manufacture 45 (2005) 335 – 344

56. Mankova I. Tribological behaviour of coated and uncoated oxide ceramics when machining, Proceedings 7th CIRP International Workshop on Modelling of Machining Operations, Ecole Nationale Supérieure d' Arts et Métiers (ENSAM), Cluny, France, May 4-5, 2004

57. Keunecke M., Yamamoto K., Bewilogua K. Mechanical and tribological properties of cBN films on silicon and tungsten carbide substrates. Thin Solid Films 398 - 399 (2001) 142-149

58. Li Q., Bello I., Marks L.D., Lifshitz Y., Lee S.T. Orientation effects in iBN/cBN interfaces: A transmission electron microscopic study. Applied Physics Letters 80 (2002) 4604 - 5415

59. Klett A., Freudenstein R., Kulisch W. Dependence of the stress of cBN films on the major deposition parameters: theoretical and experimental studies. Thin Solid Films 398-399 (2001) 130-136

60. Wong S.F., Ong C.W., Pang G.K.H., Li Q., Lau W.M. Removal of sp^2-boron nitride transition layer in the growth of cubic boron nitride films, Diamond and Related Materials 13 (2004) 1632 – 1637

61. Bello I., Chong Y.M., Leung K.M., Chan C.Y., Ma K.L., Zhang W.J., Lee S.T., Layyous A. Cubic boron nitride films for industrial applications. Diamond and Related Materials 14 (2005) 1784 – 1790

62. Zhang W.J., Bello I., Lifshitz Y., Chan K.M., Meng X.M., Wu Y., Chan C.Y., Lee S.T., Thick and adherent cubic boron nitride films grown on diamond interlayers by fluorine-assisted chemical vapor deposition. Applied Physics Letters 85(8) (2004) 1344 - 1346

63. Bewilogua K., Keunecke M., Weigel K., Wiemann E. Growth and characterization of thick cBN coatings on silicon and tool substrates. Thin Solid Films 469-470 (2004) 86-91

64. Deyneka N., Zhang X.W., Boyen H.G., Ziemann P., Banhart E. Growth of cubic boron nitride films on Si by ion beam assisted deposition at the high temperatures. Diamond and Related Materials 13 (2004) 473 – 481

65. Jiang W., More A.S., Brown W.D., Malshe A.P. A cBN-TiN composite coating inserts: Coating characterization and its applications for finish hard turning. Surface and Coatings Technology 6 (2006) 2443 – 2449

66. Vetter U., Reineke P., Ronning C., Hofsäss H., Schaaf P., Bharuth-Ram K., Taniguchi T. Europium doping of c-BN and ta-C thin films. Diamond and Related Materials 12 (2003) 1182 – 1185

67. Aslan E. Experimental investigation of cutting tool performance in high speed cutting of hardened X210Cr12 cold-work tool steel (62HRC). Materials and Design 26 (1) 2005 21-27

68. Sayagués M.J., Avilés M.A., Córdoba J.M., Alcalá M.D., Gotor F.J. Microstructural characterization of ceramic-intermetallic composites using TEM related techniques. Journal of the European Ceramic Society 30 (2010) 1765-1774

69. Jeon E.T., Joardar J., Kang S. Microstructure and tribo-mechanical properties of ultrafine Ti(CN) cermets. International Journal of Refractory Metals and Hard Materials 20 (2002) 207-211

70. Zheng Y., Xiong W.H., Liu W.J., Lei W., Yuan Q.A. Effect of nano addition on the microstructures and mechanical properties of Ti(C,N)-based cermets. Ceramics International 31 (2005) 165-170

71. Córdoba J.M., Alcalá M.D., Avilés M.A., Sayagués M.J., Gotor F.J. New production of TiC_xN_{1-x}-based cermets by one step mechanically induced self-sustaining reaction:

powder synthesis and pressureless sintering. Journal of the European Ceramic Society 28 (2008) 2085 – 2098

72. Córdoba J.M., Alcalá M.D., Sayagués M.J., Avilés M.A., Real C., Gotor F.J., Nitriding study of titanium silicide intermetallics obtained by mechanical alloying. Intermetallics 16 (2008) 948-954

73. Schwarz R.B., Petrich R.R., Saw S.K., The synthesis of amorphous NiTi alloy powders by mechanical alloying. Journal of Non-Crystalline Solids 76 (1985) 281-302

74. Hellstern E., Schultz L., Progress of the amorphization reaction during mechanical alloying in Fe-Zr. Journal of Applied Physics 63 (1988) 1408-1413.

75. Cohen N.S., Ahlswede, E., Wicks, J.D., Pankhurst Q.A., Investigation of the ternary phase diagram of mechanically alloyed FeCuAg. Journal of Condensed Matter 9 (1997) 3259 – 3276

76. Grigor'eva T.F., Tsybulya S.V., Cherepanova S.V., Kryukova G.N. G.N., Barinova A.P., Belykh V.D., Boldyrev, V.V., Mechanochemical synthesis of metastable solid solutions: Phase composition and microstructure evolution, Inorganic Materials 36 (2000) 143-149.

77. Krüger M., Franz S., Saage H., Heilmaier M., Schneibel J.H., Jéhanno P., Böning M., Kestler H., Mechanically alloyed Mo-Si-B alloys with a continuous α-Mo matrix and improved mechanical properties. Intermetallics 16 (2008) 933 – 941

78. Ipus J.J., Blázquez J.S., Franco V., Millán M., Conde A., Oleszak D., Kulik T., An equivalent time approach for scaling the mechanical alloying processes. Intermetallics 16 (2008) 470 – 478

79. Gordo E., Gómez B., Ruiz-Navas E.M., Torralba J.M., Influence of milling parameters on the manufacturing of Fe – TiCN composite powders., Journal of Materials Processing Technology 162-163 (2005) 59 – 64

80. Gómez B., Gordo E., Torralba J.M., Influence of milling time on the processing of Fe – TiCN composites. Materials Science and Engineering A 430 (2006) 59-63.

81. Zhang S., Khor K.A., Lü L., Preparation of Ti(C,N) – WC – TaC solid solution by mechanical alloying technique. Journal of Materials Processing Technology 48 (1995) 779-784

82. Zhang S., Tam S.C., Mechanical alloying of a TiC – TiN ceramic system. Journal of Materials Processing Technology 67 (1997) 112 – 116

83. Tcherdyntsev V.V., Kaloshkin S.S., Shelekhov E.V., Salimon A.I., Sartori S., Principi G., Quasicrystalline phase formation in the mechanically alloyed Al – Cu – Fe system. Intermetallics 13 (2005) 841 – 847

84. Hellstern E., Schultz L., Eckert J., Glass – forming ranges of mechanically alloyed powders. Journal of the Less-Common Metals 140 (1988) 93-98

85. Eckert J., Schultz L., Glass formation and extended solubilities in mechanically alloyed cobalt – transition metal alloys. Journal of the Less-Common Metals 166 (1990) 293-302

86. Eckert J., Schultz L., Urban K., Quasicrystal formation and phase transitions by ball milling. Materials Science and Engineering A 133 (1991) 393-397

87. Scudino S., Eckert J., Yang X.Y., Sordelet D.J., Schultz L., Conditions for quasicrystal formation from mechanically alloyed Zr – based glassy powders. Intermetallics 15 (2007) 571-582

88. Koch C.C., Amorphization of single composition powders by mechanical milling. Sripta Materialia 33 (1996) 21-27

89. Akaishi M., Satoh T., Ishii M., Taniguchi T., Yamaoka S., Synthesis of translucent sintered cubic boron nitride. Journal of Materials Science Letters 12 (1993) 1883 - 1885

90. Taniguchi T., Akaishi M., Yamaoka S., Sintering of cubic boron nitride without additives at 7.7 GPa and above 2000˚C. Journal of Materials Research 14 (1999) 162 - 169

91. Dub S.N., Petrusha I.A., Mechanical properties of polycrystalline cBN obtained from pyrolytic gBN by direct transformation technique. High Pressure Research 26 (2) (2006) 71 - 77

92. Rong X.Z., Tsurumi T., Fukunaga O., Yano T., High pressure sintering of cBN-TiN-Al composite for cutting tool application. Diamond and Related Materials 11 (2002) 280 – 286

93. Zhao Y.C, Sun J.F., Wang M.Z., Preparation of polycrystalline cubic boron nitride containing nanodiamond. Gaoya Wuli Xuebao/Chinese Journal of High Pressure Physics 21 (4) (2007) 409 - 413

94. Ren Z., Zhang R., Wang H., Chen D., Li M., Preparation and characterization of polycrystalline cubic boron nitride (PcBN) compacts by a pressureless sintering process, Advanced Materials Research 105-106 (2010) 38-41

95. Rong X.Z., Tsurumi T., Fukunaga O., Yano T., High-pressure sintering of CBN-TiN-Al composite for cutting tool application. Diamond and Related Materials 11 (2) (2002) 280 - 286

96. Rong X.Z., Yano T., TEM investigation of high-pressure reaction-sintered cBN-Al composites, Journal of Materials Science 39 (14) (2004) 4705 - 4710

97. Liu J., Jiang W., Li D., Hu J., Wang H., Kou Z., Study on the solid sintering of cBN – AlN composites. Diamond and Abrasives Engineering 5 (2006) 57 - 61

98. Zhao Y., Wang M., Preparation of polycrystalline cBN containing nanodiamond. Journal of Materials Processing and Technology 198 (2008) 134-138

99. Gaffet E., Bernard F., Niepce J.-C., Charlot F., Gras C., Caër G.L., Guichard J.-L., Tillement O., Some recent developments in mechanical activation and mechanosynthesis. Journal of Materials Chemistry 9 (1) (1999) 305-314

100. Gaffet E., Abdellaoui M., Malhouroux-Gaffet N., Formation of nanostructured materials induced by mechanical processings (overview). Materials Transactions, JIM 36 (2) 1995 198-209

101. Costa e Silva A., Ågren J., Clavaguera-Mora M.T., Djurovic D., Gomez-Acebo T., Lee B.J., Liu Z.K., Miodownik P., Seifert H.J., Applications of computational thermodynamics – the extension from phase equilibrium to phase transformations and other properties. Computer Coupling of phase diagrams and thermochemistry 31 (2007) 53-74

102. Kattner U., Erickson G., Spencer P., Schalin M., Schmid-Fetzer R., Sundman B., Jansson B., Lee B., Chart T., Costa e Silva A., Groups 4 & 5: Process modeling and applications, 1997 Ringberg Workshop, CALPHAD 24 (1) (2000) 55-94

103. Ågren J., Hayes F.H., Hoglund L., Kattner U.R., Legendre B., Schmid-Fetzer R., Applications of computational thermodynamics, Zeitschrift fuer Metallkunde/Materials Research and Advanced Techniques 93 (2) (2002) 128 – 142

104. Lee K.-M., Oh D.-K., Choi W.-S., Weissgärber T., Kieback B., Thermomechanical properties of AlN-Cu composite materials prepared by solid state processing. Journal of Alloys and Compounds 434-435 (2007) 375 – 377

105. Froes F.H., Suryanarayana C., Russel K.C., Ward M., Proceedings of Symposium held at Materials Week, The Minerals & Materials Society (TMS) and the Materials Information Society, ASM International, 1994, pp. 1-21

106. Nieh T.G., Wadsworth J., Hall-Petch relation in nanocrystalline solids. Scripta Metallurgica et Materialia 25 (1991) 955-958

107. Aguilar C., Martínez V., Navea L., Pavez O., Santander M., Thermodynamic analysis of the change of solid solubility in a binary system processed by mechanical alloying. Journal of Alloys and Compounds 471 (2009) 336 – 340

108. Kittel C., "Introduction to solid state physics", 7th Ed., John Wiley & Sons, Inc., New York, 1996

109. Porter D.A., Easterling K.E., "Phase Transformations in Metals and Alloys", 2nd Ed., Chapman & Hall, London, 1992

110. Chen Y.-L., Hu Y.-H., Hsieh C.-A., Yeh J.-W., Chen S.-K., Competition between elements during mechanical alloying in an octonary multi-principal-element alloy system. Journal of Alloys and Compounds 481 (2009) 768 – 775

111. Roura P., Farjas J., Structural relaxation kinetics for first- and second-order processes: Application to pure amorphous silicon. Acta Materialia 57 (2009) 2098 – 2107

112. Kissinger H.E., Reaction kinetics in differential thermal analysis. Analytical Chemistry 29 (1957) 1702 - 1706

113. Krill C.E., Haberkorn R., Birringer R., Specification of microstructure and characterization by scattering techniques. Handbook of Nanostructured Materials and Nanotechnology (2000) 155 – 211

114. Gubicza J., Szépvölgyi J., Mohai I., Zsoldos L., Ungár T., Particle size distribution and dislocation density determined by high resolution X-ray diffraction in nanocrystalline silicon nitride powders. Materials Science and Engineering A 280 (2000) 263 – 269

115. Gubicza J., Ribárik G., Goren-Muginstein G.R., Rosen A.R., Ungár T., The density and the character of dislocations in cubic and hexagonal polycrystals determined by X-ray diffraction. Materials Science and Engineering A309-310 (2001) 60 – 63

116. Ungár T., Gubicza J., Hanák P., Alexandrov I., Densities and character of dislocations and size distribution of subgrains in deformed metals by X-ray diffraction profile analysis. Materials Science and Engineering A 319-321 (2001) 274 – 278

117. Pantea C., Gubicza J., Ungár T., Voronin G.A., Nam N.H., Zerda T.W., High-pressure effect on dislocation density in nanosize diamond crystals. Diamond and Related Materials 13 (2004) 1753 – 1756

118. Gubicza J., Balogh L., Hellmig R.J., Estrin Y., Ungár T., Dislocation structure and crystallite size in severly deformed copper by X-ray peak profile analysis. Materials Science and Engineering A 400-401 (2005) 334 – 338

119. Ungár T., Dragomir I., Révész Á., Borbély A., The contrast factors of dislocations in cubic crystals: The dislocation model of strain anisotropy in practice. Journal of Applied Crystallography 32 (1999) 992 - 1002

120. Kuzel R., Cermansky M., Holy V., Kubena J., Simek D., Kub J., in: E.J. Mittemeijer, P. Scardi (Eds.), “Diffraction Analysis of the Microstructure of Materials”, Springer, Berlin (2004) p. 229

121. Ungár T., Ott S., Sanders P., Borbely A., Weertman J.R.. Dislocations, grain size and planar faults in nanostructured copper determined by high resolution X-ray diffraction and a new procedure of peak profile analysis, Acta Materialia 46 (1998) 3693 - 3699

122. Ungar T., Tichy G., The effect of dislocation contrast on X-ray line profiles in untextured polycrystals. Physica Status Solidi (A) Applied Research 171 (1999) 425 - 434

123. Ungar T., Borbely A., The effect of dislocation contrast on X-ray line broadening: A new approach to fine profile analysis. Applied Physics Letters 69 (1996) 3173 - 3175

124. Warren B.E., X-ray studies of deformed metals. Progress in Metal Physics 8 (C) (1959) 147 - 202

125. Guinier A., X-ray Diffraction, Freeman, San Francisco, CA, 1963

126. Grimsditch M., Zouboulis E.S., Polian A., Elastic constant of boron nitride. Journal of Applied Physics 76 (1994) 832 - 834

127. Klein C.A., Cardinale G.F., Young’s modulus and Poisson’s ratio of CVD diamond. Diamond and Related Materials 2 (1993) 918 - 923

128. Rawles R.E., Komarov S.K., Gat R., Morris W.G., Hudson J.B., D’Evelyn M.P., Mechanism of surface smoothing of diamond by a hydrogen plasma. Diamond and Related Materials 6 (1997) 791 – 795

129. D'Evelyn M.P., Taniguchi T., Elastic properties of translucent polycrystalline cubic boron nitride as characterized by the dynamic resonance method. Diamond and Related Materials 8 (1999) 1522 – 526

130. Tanigushi T., Akaishi M., Yamaoka S., Mechanical properties of polycrystalline translucent cubic boron nitride as characterized by the vickers indentation method. Journal of the American Ceramic Society 79 (2) (1996) 547 – 549

131. Harris T.K., Brookes E.J., Taylor C.J., The flow stress of PcBN cutting tool materials at high temperatures. International Journal of Refractory Metals and Hard Materials 19 (2001) 267 – 273

132. Krivoglaz M.A., "Theory of X-ray and Thermal Neutron Scattering by Real Crystals", Plenum Press, New York, 1996.

133. Masimov M., Motylenko M., Klimanek P., Analysis of deformation-induced substructure evolution of Al crystals by X-ray and electron diffraction. Materials Science and Engineering A 462 (1-2) (2007) 389 - 392

134. Klimanek P., Klemm V., Motylenko M., Romanov A., Substructure analysis in heavily deformed materials by diffraction methods. Advanced Engineering Materials 6 (11) (2004) 861 - 871

135. Langford J.I., Louër D., Scardi P., Effect of crystallite size distribution on X-ray diffraction line profiles and whole-powder-pattern fitting. Journal of Applied Crystallography 33 (3 II) (2000) 964 - 974

136. Scardi P., Leoni M., Cappuccio G., Sessa V., Terranova M.L., Residual stress in polycrystalline Diamond/Ti-6Al-4V systems. Diamond and Related Materials 6 (5-7) (1997) 807 - 811

137. Ungár T., Gubicza J., Ribárik G., Borbély A., Crystallite size distribution and dislocation structure determined by diffraction profile analysis: Principles and practical application to cubic and hexagonal crystals. Journal of Applied Crystallography 34 (3) (2001) 298 - 310

138. Ribárik G., Ungár T., Gubicza J., MWP-fit: A program for multiple whole-profile fitting of diffraction peak profiles by ab initio theoretical functions. Journal of Applied Crystallography 34 (5) (2001) 669 - 676

139. Gubicza J., Ungár T., Wang Y., Voronin G., Pantea C., Zerda T.W., Microstructure of diamond-SiC nanocomposites determined by X-ray line profile analysis. Diamond and Related Materials 15 (2006) 1452 – 1456

140. Battezzati L., Thermodynamic issues in nanocrystalline materials. Matreials Science Forum 235-238 (1997) 317 - 326

141. Philip J. Spencer. "The potential use of thermodynamic calculations for the prediction of metastable phase ranges resulting from mechanical alloying". In Thermodynamics at work. Second Edition, Klaus Hack, ed 2008. Pp, 245-262

142. Wang Y., Curtarolo S., Jiang C., Arroyave R., Wang T., Ceder G., Chen L.Q., Liu Z.K., Ab initio lattice stability in comparison with CALPHAD lattice stability. Calphad 28 (1) 2004 79 – 90.

143. Jaynes E.T., Information theory and statistical mechanics. Physics Review 106 (1957) 620 – 630

144. Masiuk S., Rakoczy R., Kinetic equation of grinding process in mixing of granular material using probability density function, transient operators and informational entropy. Chemical Engineering and Processing: Process Intensification 47 (2008) 200-208

145. Rakoczy R., The application of the informational theory to the analysis of the grinding process under action of transverse rotating magnetic field. Powder Technology 201 (2010) 161 – 170

146. Zhukov V., Mizonov V., Filitchev P., Bernotat S., The modeling of grinding process by means of the principle of maximum entropy. Powder Technology 95 (1998) 248 – 253

147. Otwinowski H., Energy and population balances in comminution process modeling based on the informational entropy. Powder Technology 167 (2006) 33 – 44

148. Kheifets A.S., Lin I.J., Energetic approach to the kinetics of batch ball milling. International Journal of Mineral Processing 54 (1998) 81-97

149. Austin L.G., Introduction to the mathematical description of grinding as a rate process. Powder Technology 5 (1972) 1 – 17

150. Kapur P.C., Fuerstenau D.W., Energy-size reduction 'laws' revisited. International Journal of Mineral Processing 20 (1987) 45 – 57

151. Kolosov A.S., Some problems of simulation and estimation of energetic efficiency of solids grinding processes, (in Russian). Izv. Sib. Otd. Akad. Nauk SSSR, 2, Ser. Khim. Nauk 1, p.26

152. Wentorf Jr. R.H., DeVries R.C., High-Pressure Synthesis (Chemistry). Encyclopedia of Physical Science and Technology (2004) 365 – 379

153. Rong X.Z., Tsurumi T., Fukunaga O., Yano T., High-pressure sintering of cBN-TiN-Al composite for cutting tool application. Diamond and Related Materials 11(2) (2002) 280 – 286

154. Biagiotti R., Macek R., The time is right for cermets. Cutting Tool Engineering (1996) 24 – 30

155. Sumitomo Electric Industries. Hard sintered body for tools. Patent No. EP 0386338 B1 (1994)

156. Qiu L.X., Yao B., Ding Z.H., Zheng Y.J., Jia X.P., Zheng W.T., Characterization of structure and properties of TiN – TiB_2 nano – composite prepared by ball milling and high pressure heat treatment. Journal of Alloys and Compounds 456 (2008) 436 – 440

157. Lee J.W., Munir Z.A., Ohyanagi M., Dense nanocrystalline TiB_2–TiC composites formed by field activation from high – energy ball milled reactants. Materials Science and Engineering A 325(1-2) (2002) 221 – 227

158. Rangaraj L., Divakar C., Jayaram V., Low temperature reactive hot pressing of TiB_2 – TiN composites. Journal of the American Ceramic Society 87 (2004) 1872 – 1878

159. Osipova I.I., Shvedkov E.L., Cutting ceramics 1985-1990, Soviet Powder Metallurgy and Metal Ceramics, vol. 31, No. 9, 1992, pp. 751-763

160. Griffiths A.A., The theory of rupture, Proc. 1st International Congress on Applied Mechanics Delft (1924) 55 – 63.

161. Griffiths A.A, The phenomena of rupture ad flow in solids, Proc. Trans. R. Soc. A221 (1921) 163 – 198

162. Lawn B.R., Wilshaw T.R., "Fracture of brittle solids". Cambridge Solid State Series, Cambridge University Press, Cambridge, 1975

163. Irwin G.R., Analysis of stresses and strains near the end of a crack traversing a plate. Journal of Applied Mechanics 24 (1957) 361 – 364.

164. Norton Company. Cemented and cemented/sintered superabrasive polycrystalline bodies and methods of manufacture thereof. Patent No. US 5151107 A1.

165. Suryanarayana C., Froes F.H., Nanocrystalline titanium-magnesium alloys through mechanical alloying. Journal of Materials Research 5 (1990) 1880 – 1886

166. Rousselot S., Bichat M.P., Guay D., Roué L., Structure and electrochemical behaviour of metastable Mg50Ti50 alloy prepared by ball milling. Journal of Power Sources 175 (2008) 621 – 624

167. Sundaresan R., Froes F.H., Mechanical alloying in the titanium-magnesium system. Key Engineering Materials 29-31 (1988) 199 – 206

168. Kalisvaart W.P., Wondergem H.J., Bakker F., Notten P.H.L., Mg-Ti based materials for electrochemical hydrogen storage. Journal of Materials Research 22 (6) (2007) 1640 - 1649

169. Huang H., Huang K., Liu S., Chen D., Microstructures and electrochemical properties of Mg0.9Ti0.1Ni1-xMx (M=Co, Mn; x=0, 0.1, 0.2) hydrogen storage alloys. Powder Technology 198 (1) (2010) 144 – 148

170. Asano K., Enoki H., Akiba E., Synthesis process of Mg-Ti BCC alloys by means of ball milling. Journal of Alloys and Compounds 486 (2009) 115 – 123

171. Asano K., Enoki H., Akiba E., Synthesis of hcp, fcc and bcc structure alloys in Mg-Ti binary system by means of ball mill. Journal of Alloys and Compounds 480 (2009) 558-563

172. Kalisvaart W.P., Notten P.H.L., Mechanical alloying and electrochemical hydrogen storage of Mg – based systems. Journal of Materials Research 23 (8) 2008 2179 – 2187.

173. Jin Y., Liu Y., Wang Y., Ye J., Influence factors and microstructure evolution during preparation of nanocrystalline (Ti, W, Mo, V)(C, N) – Ni composite powders. International Journal of Refractory Metals and Hard Materials 27 (2009) 957 – 961

174. Qingxiang W., Shuhua L., Zhikang F., Xin C., Fabrication of W-20wt%Ti alloy by pressureless sintering at low temperature. International Journal of Refractory Metals and Hard Materials 28 (2010) 576 – 579.

175. Raygan Sh., Kodori B., Yangijeh H.M., Effect of mechanical activation on the production of SiC from silica sand. International Journal of Refractory Metals and Hard Materials 29 (2011) 10 – 13.

176. Liang B., Han X., Zou Q., Zhao Y., Wang M., TiC/Ti_3SiC_2 composite prepared by mechanical alloying, International Journal of Refractory Metals and Hard Materials 27 (2009) 664 – 666.

177. Hewitt S.A., Kibble K.A., Effect of ball milling time on the synthesis and consolidation of nanostructured WC – Co composites. International Journal of Refractory Metals and Hard Materials 27 (2009) 937 – 948.

178. Whittenberger J.D., Artz E., Luton M.J., Preliminary investigation of a NiAl composite prepared by cryomilling. Journal of Materials Research 5 (2) (1990) 271 – 277

179. Huang B.L., Vallone J., Luton M.J., Formation of nanocrystalline B_2NiAl through cryomilling of Ni – 50at.%Al at 87K. Nanostructured Materials 5 (4) (1995) 414 – 424

180. Picas J.A., Forn A., Ajdelsztajn L., Schoenung J., Nanocrystalline NiCrAlY powder synthesis by mechanical cryomilling. Powder Technology 148 (1) (2004) 20 – 23

181. Zhou F., Liao X.Z., Zhu Y.T., Dallek S., Lavernia E.J., Microstructural evolution during recovery and recrystallization of a nanocrystalline Al-Mg alloy prepared by cryogenic ball milling. Acta Materialia 51 (2003) 2777 – 2791

182. Han B.Q., Lee Z., Witkin D., Nutt S.R., Lavernia E.J., Deformation behavior of nano – structured 5083 Al alloys. Metallurgical and Materials Transactions A 36 (2005) 957-965.

183. Sivasankaran S., Sivaprasad K., Narayanasamy R., Iyer V.K., An investigation on flowability and compressibility of AA 6061_{100-x} – x wt%TiO_2 micro and nanocomposite powder prepared by blending and mechanical alloying. Powder Technology 201 (1) (2010) 70 – 82

184. Razavi Tousi S.S., Yazdani Rad R., Salahi R., Mobasherpour I., Razavi M., Production of Al – 20wt% Al_2O_3 composite powder using high energy milling. Powder Technology 192 (3) (2009) 346 – 351

185. Wang Q., Chen G., Shi X., Jin R., Wang L., Chen D., Controllable synthesis of Cu_7Te_4 nanoparticles and sheet – like particles through the delayed reaction and their thermal stability. Powder Technology 207 (2011) 192 - 198

186. Mohamed F. A., Correlation between the behavior of nanocrystalline HCP metals and dislocation model for the minimum grain size obtainable by milling. Materials Science and Engineering A 527 (2010) 2157 – 2162

187. Yu H.B., Zhang D.L., Chen Y.Y., Cao P., Gabbitas B., Synthesis of an ultrafine grained TiAl based alloy by subzero temperature milling and HIP, its microstructure and mechanical properties. Journal of Alloys and Compounds 474 (2009) 105 – 112

188. Chung K.H., He J., Shin D.H., Schoenung J.M., Mechanisms of microstructure evolution during cryomilling in the presence of hard particles. Materials Science and Engineering A 356 (2003) 23 – 31

189. Li Y., Liu W., Ortalan V., Li W.F., Zhang Z., Vogt R., Browning N.D., Lavernia E.J., Schoenung J.M., HRTEM and EELS study of aluminium nitride in nanostructured Al 5083/B4C processed via cryomilling. Acta Materialia 58 (2010) 1732 – 1740

190. Almathami A., Brochu M., Crystal structure, transformation and thermal stability of nanostructured 316LSS alloyed with 2 and 6 wt.% aluminum. Materials Science and Engineering A 527 (21-22) (2010) 6020 – 6027

191. Almathami A., Brochu M., Microstructure and transformation of Al – containing nanostructured 316L stainless steel coatings processed using spark plasma sintering. Journal of Materials Processing Technology 210 (2010) 2119 – 2124

192. Huang B., Perez R.J., Lavernia E.J., Grain growth of nanocrystalline Fe – Al alloys produced by cryomilling in liquid argon and nitrogen. Materials Science and Engineering A 255 (1998) 124 – 132

193. Witkin D.B., Lavernia E.J., Synthesis and mechanical behavior of nanostructured materials via cryomilling. Progress in Materials Science 51 (2006) 1 – 60

194. Hedayati M., Salehi M., Bagheri R., Panjepour M., Maghzian A., Ball milling preparation and characterization of poly (ether ketone)/surface modified silica nanocomposite. Powder Technology 207 (2011) 296 - 303

195. Milligan J., Vintila R., Brochu M., Nanocrystalline eutectic Al – Si alloy produced by cryomilling. Materials Science and Engineering A 508 (2009) 43 – 49

196. Zhou F., Witkin D., Nutt S.R., Lavernia E.J., Formation of nanostructure in Al produced by low – energy ball milling at cryogenic temperature. Materials Science and Engineering A 375-377 (2004) 917 – 921

197. Zhang X., Wang H., Narayan J., Koch C.C., Evidence for the formation mechanism of nanoscale microstructure in cryomilled Zn powder. Acta Materialia 49 (2001) 1319 – 1326

198. Mindivan H., Reciprocal sliding wear behaviour of B_4C particulate reinforced aluminium alloy composites. Materials Letters 64 (2010) 405 – 407

199. Williamson G.K., Hall W.H., X-ray line broadening from filed aluminium and wolfram. Acta Metallurgica 1 (1953) 22 – 31

200. ICSD Database FIZ Karlsruhe 2009 – 02, version 2.3.

201. Slater J. C., Atomic radii in crystals. Journal of Chemical Physics 41 (1964) 3199 - 3204

202. Jacobsen S.N., Helmersson U., Erlandsson R., Skårman B., Wallenberg L.R.., Sharp microfaceting of (001)-oriented cerium dioxide thin films and the effect of annealing on surface morphology. Surface Science 429 (1999) 22 – 33.

203. Choi S.Y., Kang S.J.L,. Sintering kinetics by structural transition at grain boundaries in barium titanate. Acta Materialia 52 (2004) 2937 - 2943

204. Lee B.K., Chung S.Y., Kang S.J.L., Grain boundary faceting and abnormal grain growth in Acta Materialia 48 (2000)1575

205. Jung Y..I, Choi S.Y., Kang S.J.L., Effect of oxygen partial pressure on grain boundary structure and grain growth behavior in BaTiO3. Acta Materialia 54 (2006) 2849 – 2855

206. Lee M.G., Chung S.Y., Kang S.J.L., Boundary faceting-dependent densification in a $BaTiO_3$ model system. Acta Materialia 59 (2011) 692 – 698.

207. Can N., Bodkin R., Cubic boron nitride compacts, US Patent US2008226897 (A1), 2009.

208. Pretorius C.J., Can N., Harden P.M., Method of making a cBN compact. Patent WO2007122489.

209. Teramoto M., Kukino S., Fukaya T., Abe M., cBN sintered body and tool made of cBN sintered body. US Patent US2010313489.

210. Kukino S., Shiraishi J., Nakai T., Cutting tool made of Al_2O_3-coated cBN-based sintered material. US Patent US6337152 (B1), 2002.

211. Twersky A.R., Can N., Cubic boron nitride compacts, Patent WO200872180

212. Ederyd S., Packers S., Rai G., Rodriguez A., Corrosion and oxidation resistant PCD/PCBN grades for woodworking applications. European Patent EP0825915 (A1), 1999.

ANNEXES: Published papers

1. Int. Journal of Refractory Metals and Hard Materials 29 (2011) 312-319
2. Int. Journal of Refractory Metals and Hard Materials 29 (2011) 445-451
3. Powder Technology 211 (2011) 221-225